Universität Hamburg
DER FORSCHUNG | DER LEHRE | DER BILDUNG

Spin-resolved single-atom microscopy of ^{87}Sr

Dissertation
zur Erlangung des Doktorgrades
an der Fakultät für Mathematik, Informatik und Naturwissenschaften
Fachbereich Physik der Universität Hamburg

vorgelegt von
Thies Plassmann

Hamburg
Juli 2026

Gutachter/innen der Dissertation:

Dr. Guillaume Salomon
Prof. Dr. Peter Schauss

Zusammensetzung der Prüfungskommission:

Prof. Dr. Ludwig Mathey
Prof. Dr. Henning Moritz
Prof. Dr. Peter Schauss
Prof. Dr. Klaus Sengstock
Dr. Guillaume Salomon

Vorsitzende/r der Prüfungskommission:

Prof. Dr. Ludwig Mathey

Datum der Disputation:

07.07.2026

Vorsitzender des Fach-Promotionsausschusses PHYSIK:

Prof. Dr. Johannes Haller

Leiter des Fachbereichs PHYSIK:

Prof. Dr. Markus Drescher

Dekan der Fakultät MIN:

Prof. Dr.-Ing. Norbert Ritter

Abstract

Quantum simulations with ultracold atoms are a powerful and versatile tool for investigating models of complex quantum materials that are intractable with classical computational methods. Simulating the Fermi-Hubbard model with atomic quantum simulators is of particular relevance since it is expected to provide fundamental insights into correlated quantum systems and facilitate the development of advanced quantum technologies.

Despite substantial progress in controlling and probing such systems, experimental challenges persist. In particular, quantum simulations of the SU(N) Fermi-Hubbard model require challenging imaging techniques with state and single-atom resolution of atoms with multiple spin states.

In this thesis, we present a novel experimental approach employing optical Stern-Gerlach potentials to spatially separate and detect multiple nuclear spin states in fermionic strontium atoms. Our setup utilizes a combination of vacuum, magnetic field, and laser systems to produce ultracold bosonic and fermionic strontium samples at sub-μK temperatures. Subsequently, single atoms are prepared with higher than 99 % fidelity in a tweezer trap. After releasing the atom from the tweezer, a precisely positioned tensor potential is applied to the atom. The tensor potential depends on the absolute value of the ground state spin state $|m_F|$ and creates a spin-dependent, Stern-Gerlach-like force that spatially separates the atoms based on their initial spin state. After a free-expansion time, we rapidly image the atom in free space with fluorescence imaging beams and obtain a detection fidelity of 98 %. This technique enables the simultaneous detection of up to four nuclear spin states with fidelities between 93.6 % and 99.7 %.

Furthermore, we demonstrate the capability to monitor coherent nuclear spin dynamics following a magnetic-field quench, highlighting the potential of these systems for quantum information processing. The developed imaging technique opens new avenues for quantum simulations with multi-electron atoms and the realization of the SU(N) Fermi-Hubbard model, thus offering promising perspectives for exploring strongly correlated quantum phenomena and advancing quantum technologies.

Zusammenfassung

Quantensimulationen mit ultrakalten Atomen sind ein leistungsfähiges und vielseitiges Werkzeug, um Modelle von komplexen Quantenmaterialien zu untersuchen, die mit klassischen Rechenmethoden nicht zugänglich sind. Die Simulation des Fermi-Hubbard-Modells mit atomaren Quantensimulatoren ist besonders relevant, da sie grundlegende Einblicke in korrelierte Quanten-Vielteilchensysteme ermöglicht und die Entwicklung von Quantentechnologien verspricht.

Trotz bedeutender Fortschritte bei der Kontrolle und Untersuchung solcher Systeme bestehen weiterhin experimentelle Herausforderungen. Insbesondere erfordert die Simulation von Erweiterung des binären Fermi-Hubbard-Modells neue Abbildungstechniken, die einzelne Atome und deren Spin-Zustand auflösen können.

In dieser Arbeit stellen wir einen neuartigen experimentellen Ansatz vor, der optische Stern-Gerlach-Potentiale nutzt, um mehrere Kernspinzustände in fermionischen Strontiumatomen räumlich zu trennen und zu detektieren. Unser Aufbau verwendet eine Kombination aus Vakuum-, Magnetfeld- und Lasersystemen, um ultrakalte bosonische und fermionische Strontiumatome bei suk-μK Temperaturen zu erzeugen. Anschließend werden einzelne Atome mit einer Erkennungsgenauigkeit von über 99 % in einer Tweezer-Falle präpariert.

Nach dem Freilassen des Atoms aus der Tweezer-Falle wird ein präzise positioniertes Tensorpotential auf das Atom angewendet. Das Tensorpotential hängt vom Betrag des Grundzustands-Spinzustands $|m_F|$ ab und erzeugt eine spinabhängige, Stern-Gerlach-ähnliche Kraft, die die Atome anhand ihres Spinzustands räumlich trennt. Nach einer Freiflugzeit werden die Atome mit einer schnellen Abbildungstechnik im freien Raum mit einer Erkennungsgenauigkeit von 98 % abgebildet. Diese Technik ermöglicht die gleichzeitige Detektion von bis zu vier Kernspinzuständen mit einer Genauigkeit zwischen 93.6 % and 99.7 %.

Darüber hinaus zeigen wir die Fähigkeit, kohärente Dynamiken der Kernspins nach einem Magnetfeld Quench zu verfolgen, was das Potenzial dieser Systeme für die Quanteninformationsverarbeitung zeigt. Die entwickelte Abbildungstechnik eröffnet neue Möglichkeiten für Quanten-Simulationen mit Mehr-Elektronen-Atomen und für die Realisierung des SU(N) Fermi-Hubbard-Modells. Damit eröffnen sich vielversprechende Perspektiven, um stark korrelierte Quanteneffekte zu erforschen und Quantentechnologien weiterzuentwickeln.

Contents

Abstract v

Zusammenfassung vii

1 Introduction 1
1.1 Quantum Simulation with ultracold atoms . . . 1
1.2 Towards Quantum Simulation of the SU(N) Fermi Hubbard model with ^{87}Sr atoms . . . 2
1.3 A microscope with spin and density resolution for single ^{87}Sr atoms . . . 5
1.4 Outline of thesis . . . 6

2 Experimental apparatus 9
2.1 Strontium: the atom of choice . . . 9
2.1.1 Level structure . . . 10
2.2 Vacuum system . . . 11
2.2.1 Oven section . . . 12
2.2.2 Differential pumping sections . . . 13
2.2.3 Vacuum system assembly . . . 15
2.3 Magnetic fields . . . 18
2.3.1 MOT magnetic field coils . . . 18
Design . . . 18
Water cooling and interlocks . . . 21
Field validation . . . 23
Current switching electronics . . . 23
2.3.2 Compensation field coils . . . 25
2.4 Laser systems . . . 25
2.4.1 Blue laser system . . . 25
2.4.2 Red laser system . . . 27
Frequency stabilization . . . 28
OSG laser frequency stabilization . . . 29
2.4.3 Repump lasers . . . 30
2.4.4 Dipole trap lasers . . . 30
2.5 Optical systems for the experiment . . . 31
2.5.1 Atomic beam setup . . . 31
2.5.2 MOT system . . . 32
Blue MOT beams . . . 32
Red MOT beams . . . 33
Repumper beams . . . 33
Low-NA imaging . . . 33
2.5.3 Reservoir dipole trap . . . 34
2.5.4 Microscope setup . . . 35
Tweezer beam setup . . . 35
High-NA imaging . . . 36

Single-atom imaging beams . . . 38
Free-space imaging beams . . . 38
2.5.5 OSG beam setup . . . 38

3 Production of cold strontium gases **41**
3.1 Atomic beam . . . 41
3.2 Blue MOT . . . 42
3.2.1 Mini Zeeman slower beam . . . 43
3.2.2 Reservoir state loading . . . 45
3.3 Red MOT . . . 46
3.3.1 General red MOT sequence . . . 46
3.3.2 ^{87}Sr red MOT . . . 47
3.4 Reservoir dipole trap loading . . . 49

4 Single atom production **53**
4.1 Tweezer setup characterization . . . 54
4.1.1 Tweezer trap . . . 54
4.1.2 Sisyphus cooling beam . . . 57
4.2 Single-atom imaging and cooling . . . 58
4.2.1 Single-atom detection fidelity . . . 60
4.2.2 Cooling optimization . . . 61
4.2.3 Imaging resolution . . . 62

5 Spin-resolved imaging of single atoms **65**
5.1 Free-space imaging of individual atoms . . . 66
5.1.1 EMCCD noise characterization . . . 68
5.1.2 Imaging beam characterization . . . 70
5.1.3 Image analysis . . . 71
5.1.4 Imaging fidelity and spatial resolution . . . 72
5.1.5 Atom number resolution . . . 75
5.2 The optical Stern-Gerlach beam . . . 76
5.2.1 OSG beam design consideration . . . 76
5.2.2 OSG beam characterization . . . 79
5.3 Spin resolution . . . 83
Detection fidelity . . . 84
Spin-polarized manifold via optical pumping . . . 88
Application: Coherent nuclear spin dynamics . . . 90
5.4 Possible improvements . . . 91
Towards SU(N>4) resolution . . . 94

6 Conclusion and Outlook **99**

A Zeeman shifts **105**

B Light shifts **107**

C Magnetic field calculations **111**
C.1 Magnetic field . . . 111
C.2 Dipole force on coils . . . 112
C.3 Water cooling power . . . 113

Acknowledgements **125**

Chapter 1

Introduction

1.1 Quantum Simulation with ultracold atoms

Neutral atoms have established themselves as a powerful platform for quantum simulations of quantum many-body systems [1]. One of the main reasons for their success is the high level of controllability they offer. By choosing a suitable atomic species, the particles can have either fermionic or bosonic statistics. Interactions can be tuned over a wide range, from contact interactions to long-range interactions. In addition, atoms can be arranged in almost arbitrary geometries, enabling both itinerant dynamics in optical lattices [2] and well-resolved configurations in tweezer arrays [3]. Experimental control further extends to the atom number, the temperature, and the internal state composition.

These many control handles allow one to engineer a quantum system to match the defining features of a model that is used to understand the underlying mechanisms of physical phenomena. With that, neutral atoms realize the idea of an analog quantum simulator, as originally proposed by Richard Feynman in his famous work about computers in quantum physics [4]. The basic idea is to simulate an intractable quantum system with another, more controllable quantum system that is easier to read out. An analog quantum simulator can circumvent the inherent scaling problem of quantum many-body systems, where the Hilbert space grows exponentially with the number of particles involved.

The features of ultra-cold neutral atoms in quantum simulation experiments have led to many advances in understanding correlated condensed-matter problems. Examples range from spin models with well-controlled interactions realized in Rydberg atoms within tweezer arrays [5], strongly correlated fermions [6, 7, 8], and topological phenomena [9, 10, 11, 12].

One particularly important model is the Fermi–Hubbard model. The Fermi-Hubbard model is believed to capture the essence the relevant phenomenon of high-temperature superconductivity in cuprates, and has evolved into a prominent testbed for developing and innovating atomic quantum simulation techniques [13]. The SU(2) Fermi–Hubbard model is defined on a two-dimensional square lattice and might describe the physics of electrons with spin one-half in cuprate superconductors (figure 1.1). The interaction is an on-site repulsive contact interaction, while the dynamics consist of nearest-neighbor hopping between lattice sites. In state-of-the-art atomic quantum simulators, electrons are mapped to alkali atoms residing in an optical lattice. The spin of the electrons is translated into internal hyperfine states of the alkali atom [6].

Quantum gas microscopes, with single-site and even single-spin resolution, can now directly probe the phases and dynamics of the atoms in the Fermi–Hubbard model and thus provide insights into the many-body mechanisms with single particle resolution [14]. Such observables are not directly accessible in real condensed-matter systems. Techniques such as angle-resolved photoemission [15] or scanning tunneling microscopy [16] can resolve the excitation spectra of real materials, but they cannot resolve the dynamics on the

level of individual electrons. Atomic quantum simulators have reached a level of controllability and complexity that makes them highly relevant to materials science. They have realized and demonstrated several predicted phases of the Fermi-Hubbard phase diagram [17], ranging from the metal-to-Mott-insulator transition [18, 19] to antiferromagnetic ordering [20]. They are now being optimized to reach unexplored regimes that are also difficult to predict with advanced numerical methods [21].

Besides the successful exploration of the Fermi–Hubbard phase diagram so far, extensions of the Fermi–Hubbard model are still largely unexplored at the single-atom level. These extensions include different lattice geometries that can introduce geometric frustration and lead to highly correlated phases, for example, in triangular lattices [22]. They also include long-range interactions instead of on-site contact interaction, which can be implemented using magnetic atoms [23, 24, 25]. Another important direction is the simulation of fermions with more than two spin states, using suitable internal atomic states [26, 27, 28]. This generalization from an SU(2) to an SU(N) Fermi–Hubbard model has motivated the construction of our experiment and the development of suitable imaging techniques in the present work.

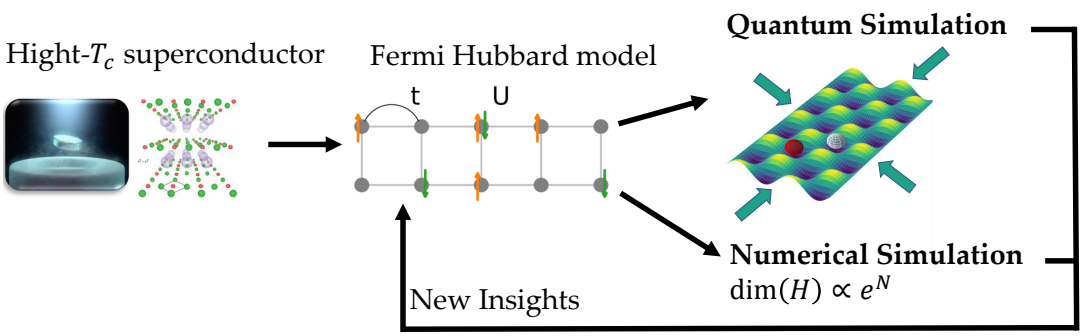

FIGURE 1.1: Presentation of the quantum simulation idea. The left picture shows a copper oxide superconductor material (taken from [13]). The copper and oxygen atoms are arranged in layers, which gives rise to a 2D model description of its electronic dynamics. This model is the Fermi Hubbard model (middle picture). In this model, spin-1/2 particles hop between lattice-sites and experience on-site interaction. This model can be realized and studied with an atomic quantum simulator of atoms residing in optical lattice potentials. An alternative is numerical simulations, which are limited by an exponentially growing Hilbert space.

1.2 Towards Quantum Simulation of the SU(N) Fermi Hubbard model with ^{87}Sr atoms

Extensions of the Fermi–Hubbard model from SU(2) to SU(N) symmetry are particularly relevant for simulating electronic systems that carry an additional orbital degree of freedom and therefore cannot be described by a single-band Fermi-Hubbard model. Such orbital degrees of freedom appear in a variety of solid-state materials, for example in transition-metal oxides [29] and in the spin-valley symmetry of graphene, whose band structure resembles an SU(4) system [30].

Another feature of SU(N) systems is the large variation of interaction channels that two atoms with N spin states can have. As a result, quantum fluctuations in the spin sector remain important at negligible thermal fluctuations and have an influence on the magnetic ordering. Another result is the enhanced collision and thermalization rates during evaporative cooling of SU(N) atoms, which offer new possibilities for cooling techniques and

for creating quantum systems with very low entropy. This effect has been observed in a comparison of a degenerate SU(6) Fermi gas with a SU(2) Fermi gas [31] or the rapid production of a degenerate SU(10) gas [32].

To date, a variety of SU(N) systems have been realized [27, 28]. For SU(N) physics, atoms from the second main group of the periodic table, as well as alkaline-earth-like atoms, are suitable candidates, such as ytterbium (Yb). Most commonly, the isotope ^{173}Yb and ^{87}Sr are used. For our experiment, we have chosen ^{87}Sr. The atoms obtain their spin-symmetric interactions from having a closed S-shell as their ground state, which means there is no electronic orbital angular momentum ($J = L + S = 0$). The atom's total angular momentum F is determined solely by the nuclear angular momentum I, which for the isotope ^{87}Sr can be high at $I = 9/2$. The large F results in 10 different projection states $m_F = -9/2, ..., 9/2$. A peculiarity of the nuclear magnetic moment is its decoupling from the electronic orbital degrees of freedom. As a result, the nuclear moment does not significantly modify the scattering properties of strontium atoms, so all 10 m_F-states interact with the same strength, enabling the formation of SU(10)-symmetric interactions [26].

The level structure of strontium has further features that make this atom relevant for quantum simulations and quantum technologies. Strontium possesses the same vanishing total angular momentum in its clock state $^3P_0$, which is well suited for using the narrow, doubly forbidden transition in atomic clocks [33, 34], or for implementing qubits with long coherence times [35, 36]. Furthermore, the $^3P_0$ state has the same spin symmetric interaction as the ground state $^1S_0$ and can be used to construct a two-orbital system, which finds applications in the Kondo lattice model [37]. The level diagram also shows a broad transition to $^1P_1$. This transition is even broader than the corresponding transition in typical alkali atoms, which is well suited for fluorescence imaging or laser cooling [38].

Although SU(N) systems in optical lattices can be prepared with low entropy, an outstanding experimental challenge for quantum simulations of the SU(N) Fermi-Hubbard model is the readout of the system with single-site density and spin resolution. So far, many experiments have mainly concentrated on global observables of bulk systems. Different imaging techniques have been developed to probe these systems, and are reviewed below.

The creation of SU(N) atoms in optical lattices in two (2D) or three dimensions (3D) is experimentally similar to the SU(2) case [39]. State-selective absorption imaging has been used to determine the equations of state for both SU(2) and SU(6) systems [40]. Another approach is the detection of excitations in the spin sector with precise lattice modulations [41]. This approach allowed for the detection of the formation of a SU(6) Mott insulator. By using local band-mapping into double wells, singlet-triplet oscillations have spectroscopically revealed the formation of antiferromagnetic phases in both SU(2) and SU(6) Mott insulators [42].

An entirely different approach does not rely on directly examining spin-dependent transitions but separates the atoms using spin-dependent potentials. Such optical Stern-Gerlach approach allowed for the detection of 6 m_F-states for ^{173}Yb [43] and 10 m_F-states for ^{87}Sr in bulk gases [44].

Upgrading these imaging techniques to quantum gas microscopes with single-atom and single-spin resolution introduces a new level of experimental challenge. In particular, methods developed for the SU(2) case cannot be transferred directly to SU(N) systems. For the standard Fermi-Hubbard model, in-situ fluorescence imaging has been developed [45, 46, 47, 48, 49, 50]. However, due to light-assisted collisions, the imaging process unavoidably projects the occupation number to either 0 or 1 [51]. Distinguishing between spin states, therefore requires additional steps. This can be achieved either by selectively removing one of the spin states [52] or by spatially separating the two spin components

using a magnetic-field gradient together with overlapped superlattices [53]. The superlattice approach allows the creation of spatially separated two-dimensional lattice planes that contain only one of the two spin components. Imaging in these resolvable lattice planes then enables the full reconstruction of the spin state and the atom number at each lattice site.

An alternative promising approach is spin-selective fluorescence imaging of atoms in the optical lattice. Instead of removing atoms based on their spin state, each spin state is imaged directly. Thanks to the level structure of SU(N) atoms, precise spectroscopy can be performed on the $^3P_1$ line or even more accurately on the $^3P_0$ line, thereby not affecting the imaging transition of neighboring spin states. Using the narrow $^3P_1$ transition, recent advances have led to spin-resolved imaging with single-atom resolution. The technique images the spin-state of every single atom by implementing a step-wise spin-selective optical pumping and imaging protocol [54].

In this work, we use yet another approach. We will use local spin-dependent optical potentials to spatially separate the strontium atoms based on their nuclear spin state and examine to what extent this approach can be applied to nuclear-spin-resolved single-atom imaging. Using this technique in a quantum gas microscope for SU(N) fermions would allow to explore with high resolution the intriguing phase diagram of the SU(N) Fermi-Hubbard model [27]. In particular, it will be exciting to use it to detect the emergence of anti-ferromagnetic (AFM) ordering with SU(3)-interactions as a first extension of the SU(2) case as illustrated in figure 1.2 [55, 56]. As N increases further, frustrated states can occur, potentially leading to strongly correlated phases such as valence bond solids [57] or chiral spin liquids [58].

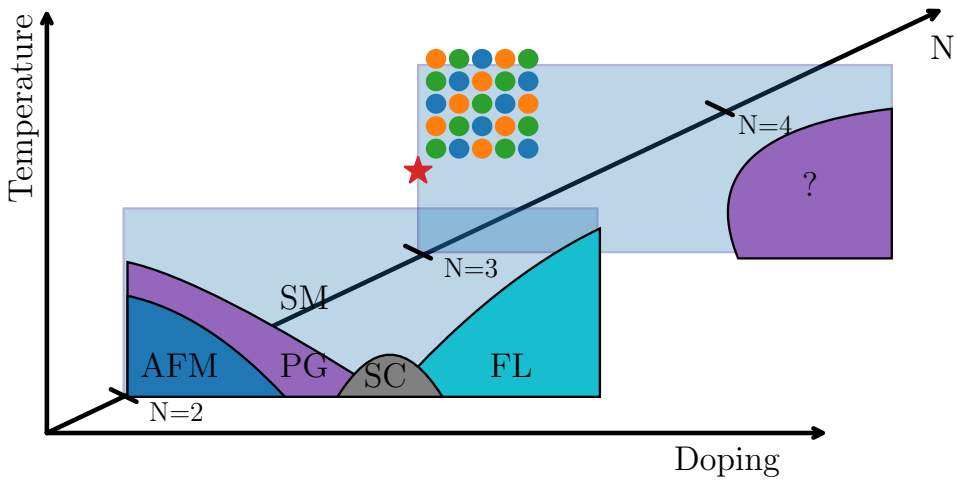

FIGURE 1.2: Phase diagrams of the SU(N) Fermi-Hubbard model. For the extensively studied SU(2) case, one expects the anti-ferromagnetic (AFM), pseudo gap (PG), strange metal (SM) and super conducting phase (SC). For high doping the Fermi-liquid phase (FL) appears. Increasing the number of spin states N is an exciting frontier to explore as much less is known about these phase diagrams. Mostly for integer filling, phases have been reliably calculated. Such example is the $N = 3$ antiferromagnetic phase as marked in red. Doping of systems with larger N, provides mostly unexplored phases that are interesting to study experimentally.

1.3 A microscope with spin and density resolution for single ^{87}Sr atoms

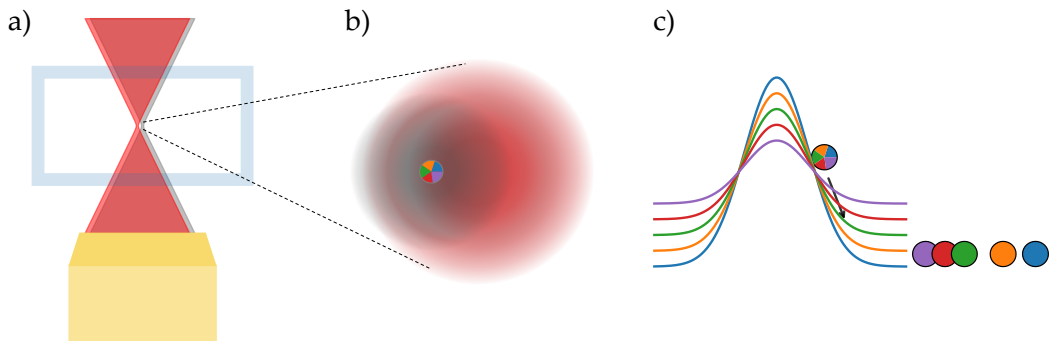

FIGURE 1.3: Visualization of the working principle of our spin-resolved microscopy for atoms with more than two spin states. a) An atom is held by an optical tweezer inside the vacuum chamber. b) Next to the tweezer beam (gray) is an optical Stern-Gerlach beam (red), which creates a spin dependent light shift and potential for the atoms. c) Since the atoms are placed on the gradient of the Gaussian beam, the atoms role down the different potential curves and reveal their spin state in the respective displacement after some TOF time.

Starting from a cold cloud of ^{87}Sr atoms in random spin states, the atoms must be separated using a spin-dependent potential and subsequently imaged. For alkali atoms, a magnetic gradient field is applied to alter the potential and create a spin-dependent separation. This is known as the Stern-Gerlach approach [59, 53, 60, 61]. In the case of alkali atoms, the magnetic field couples to the atom's orbital angular momentum. In contrast, separating the strontium atoms based on their nuclear angular momentum state would require an unrealistically high magnetic field. Therefore, an optical Stern-Gerlach method must be employed.

In this method, a focused laser beam that is closely tuned to the $^3P_1$ transition couples differently to the ground state spin manifold. This beam creates slightly different potentials for the different spin states. By creating highly focused beams with a high-NA microscope objective, the method can be scaled down to the single-atom level: one optical Stern-Gerlach (OSG) potential is applied per single-atom trap. The atom must be located in the gradient of the focused Gaussian beam. The resulting potential gradient exerts a force on the atom, which, after turning off the trap and the potential, results in a spin-dependent free-flight motion. ^{87}Sr atoms in different m_F-states travel different distances, which can be resolved with microscopy techniques. This experimental approach is visualized in figure 1.3.

Another experimental challenge is imaging the atom in free expansion with sufficiently high detection fidelity. Conventional fluorescence imaging takes place inside the trap sites and scatters a large amount of photons at a localized spot. Detrimental heating from the imaging process can be compensated by optical cooling techniques such as Sisyphus and Raman sideband cooling, enabling high detection fidelities [62, 63, 64, 65]. In contrast, conventional fluorescence imaging of an untrapped atom would cause the atom to be driven quickly out of the imaging sight. To circumvent this, we exploit a fast imaging technique that uses short alternating imaging pulses of counter-propagating imaging beams to detect atoms in free space [66, 67, 68].

In the long term, the atoms are intended to reside in optical lattices. However, in this work, the focus is on individual atoms in tweezer traps as a feasibility study of our

method. Compared to spectroscopic excitation and spin-resolved imaging within the trap, the combination of an optical Stern-Gerlach potential and free-space imaging offers two main advantages. First, multiple atoms can be resolved simultaneously, making excitation patterns in the density sector visible [67, 68]. Traditional imaging inside a trap causes parity projection to either 1 or 0 atoms. Consequently, it provides complete spin and density information for all atoms at once, without requiring the detection of individual spin transitions step by step [54, 69]. Secondly, the fast free-space imaging technique circumvents off-resonant scattering from the trap light, which can strongly affect slow sequential spin-resolution techniques. Although the trap light is far detuned and has a low scattering rate, a long imaging time can still yield a substantial number of scattering events [70]. After a scattering event, the atom does not necessarily return to its initial spin state, which ultimately reduces the fidelity of the spin-resolved imaging. Overall, we expect our method to enable the reconstruction of complex spin and density correlations, which will aid in characterizing strongly correlated phases in the SU(N) Fermi-Hubbard model.

1.4 Outline of thesis

This thesis presents the study of spin- and density-resolved microscopy of individual ^{87}Sr atoms. The work is structured into 4 main parts.

The first part in chapter 2 introduces the experimental apparatus. It begins with an overview of strontium's atomic properties relevant to laser cooling and trapping. Subsequently, the design and implementation of the vacuum system, magnetic field, and laser systems are described, which are essential for the laser cooling processes. Laser cooling of strontium atoms uses a two-stage magneto-optical trap (MOT) method, described in chapter 3. The cooling process starts with a 2D blue MOT in the atomic source. The first stage utilizes the broad dipole transition to capture and initially cool the atoms to mK temperatures. Following this, the atoms are transferred into a narrow-line red MOT, exploiting the intercombination line, which allows for further cooling to μK temperatures. The first part concludes with the loading of atoms from the red MOT into a reservoir dipole trap.

Chapter 4 focuses on the preparation and imaging of single atoms in a tweezer trap. It begins with setting up the tweezer system and loading atoms from the cold red MOT into the tweezer trap. After loading, the trap is characterized, and single-atom detection is performed using blue fluorescence imaging and red Sisyphus cooling.

The next chapter 5 presents the results of our state-resolved single-atom imaging technique. This involves rapid free-space imaging which is developed and characterized here for strontium atoms. Afterward, combining free-space imaging with optical Stern-Gerlach separation enables the detection of single atoms and their respective spin states. The fidelity of this method is characterized based on the single-atom and spin preparation.

The thesis concludes in chapter 6 with a summary of the methods and discusses the potential to apply this approach for imaging multiple atoms in a 2D optical lattice.

Chapter 2

Experimental apparatus

The first chapter provides an overview of our experimental setup. We begin with a brief review of the atomic properties of strontium in Section 2.1. Next, we describe the essential building blocks of our apparatus. Section 2.2 discusses the vacuum and oven system. Next, section 2.3 covers the construction of the magnetic field systems. Section 2.4 describes the relevant laser setups. We then present the various optical setups for cooling, trapping, and state preparation of strontium atoms in section 2.5.

2.1 Strontium: the atom of choice

Isotope	Natural abundance	Statistics	Nuclear Spin	Scattering length in a_0
^{84}Sr	0.56 %	bosonic	$I = 0$	124 a_0
^{86}Sr	9.86 %	bosonic	$I = 0$	830 a_0
^{87}Sr	7.00 %	fermionic	$I = 9/2$	97 a_0
^{88}Sr	82.58 %	bosonic	$I = 0$	-1 a_0

TABLE 2.1: Naturally occurring isotopes of strontium and relevant properties for this work. The properties are taken from [71] and [72].

The most crucial part of the experimental apparatus is the element with which we work: strontium. In this section, we describe the relevant properties that we considered during the planning and operation of the experiments.

In the lab, we use natural strontium in our oven. Natural strontium consists of 4 stable isotopes, with one fermionic and three bosonic isotopes. The most abundant isotope is ^{88}Sr with 82.58 %. Second is ^{86}Sr with 9.86 % and ^{87}Sr with 7.00 %. The least abundant is ^{84}Sr with only 0.56 % [71]. Strontium has a small overall isotope shift, which can be covered with AOM frequency-shifters. For the work in this thesis, the only two relevant isotopes are ^{87}Sr and ^{88}Sr. Nevertheless, we have also produced sub-μK gases of ^{86}Sr and ^{84}Sr on our machine. The isotope-specific properties are summarized in table 2.1.

The ^{87}Sr isotope has favorable properties for building a fermionic quantum simulator. First and foremost, ^{87}Sr is a fermion. Its scattering length of 124 a_0 is in the right regime for efficient evaporative cooling. This will allow us to prepare a cold sample in an optical lattice. Similarly, the scattering length is large enough to cause correlated dynamics in typical optical lattice experiments. For this work, we are mostly enthusiastic about the large nuclear spin of ^{87}Sr. The nuclear spin is, with $I = 9/2$, one of the largest among the laser-coolable elements. As a consequence, it possesses a rich hyperfine structure in its excited states as presented in the next section in figure 2.1.

^{88}Sr, on the other hand, is a boson with a scattering length of $-1\,a_0$. It has no nuclear spin and therefore has a simpler level structure. Because of its properties, it is less relevant for our quantum simulation goals. Due to its simpler level structure, ^{88}Sr has always

been the go-to element for us when implementing and characterizing new experimental techniques. Throughout the thesis, we will switch back and forth between ^{87}Sr and ^{88}Sr.

2.1.1 Level structure

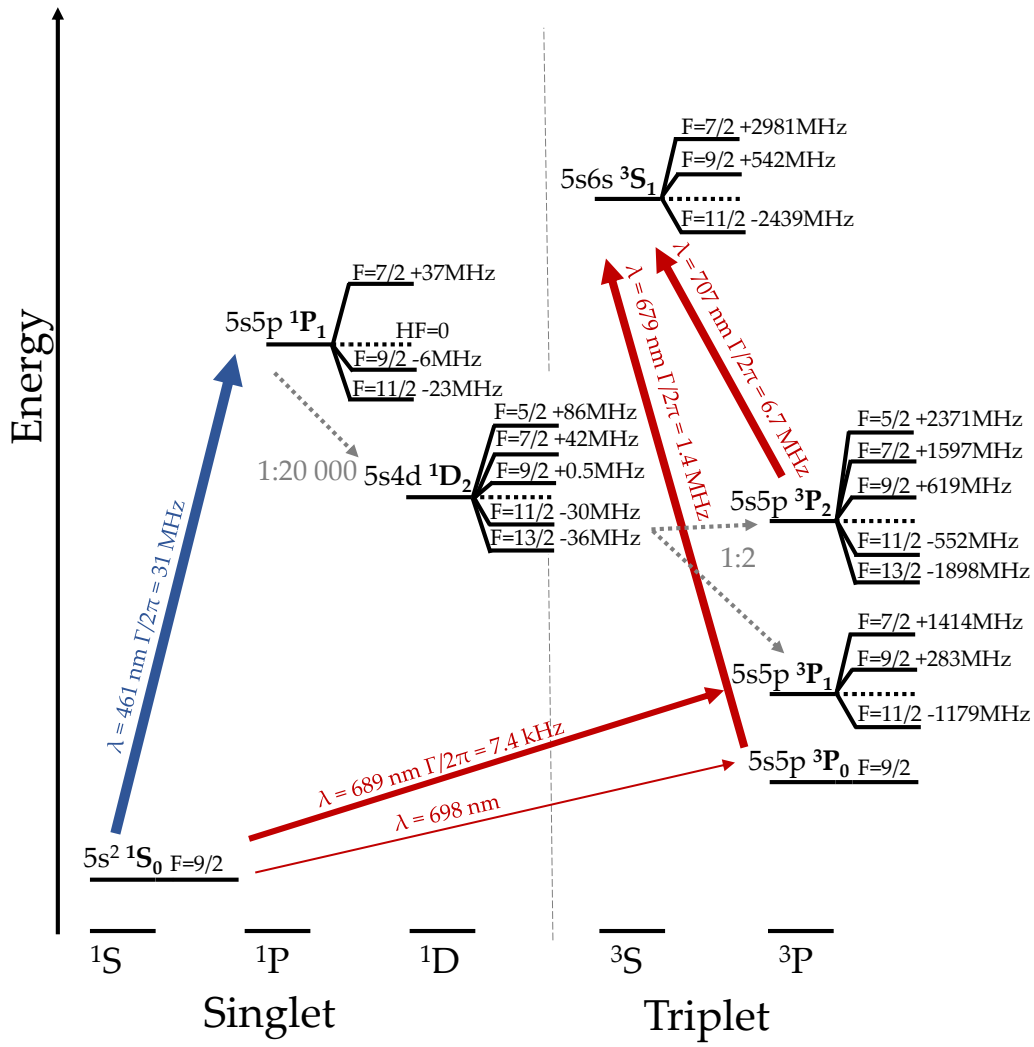

FIGURE 2.1: The levelstructure of the two-electron atom strontium splits in singlet and triplet states. The diagram only contains states (black), transitions (arrow) and decay channels (gray arrow) relevant to this work. The related hyperfine states for ^{87}Sr are referenced to the ^{88}Sr states. The data is based on the atomic data base [71].

The strontium atom has a closed-shell electron configuration with two electrons in the 5*s* orbital in its ground state. The energy-level structure is presented in 2.1 and features a series of singlet and triplet states, with the most prominent optical transition between the $^1S_0$ and the $^1P_1$ state. It is a dipole transition with a large linewidth of 30.5 MHz and a saturation intensity of 40.76 mW/cm^2 [73]. The small lifetime of this state allows for scattering a large number of photons, which is exploited for fluorescence imaging processes and in our blue 2D, 3D MOT and Zeeman slower setups to efficiently capture and quickly cool hot atoms to milli-Kelvin temperatures. The limit is thereby the Doppler temperature of 732 μK.

Since the $^1D_2$ state is lower in energy than the $^1P_1$ state, the $^1P_1$ state decays with 1:20 000 probability to this state [65]. The $^1D_2$ state is a curse and blessing at the same time for our experiment. As presented in chapter 5, our fast free-space imaging technique suffers from state loss when the atom decays to $^1D_2$ and essentially blocks further photon scattering owing to its lifetime of $\approx 350\,\mu$s [74, 75]. On the other hand, it is a blessing during the blue 3D MOT when the $^1D_2$ state decays further to either the $^3P_2$ or $^3P_1$ state. In case it decays to the $^3P_1$ state, it quickly returns to the blue cooling process with a $^3P_1$ state lifetime of 21.5 μs [73]. However, in the $^3P_2$ state, it lives for seconds but is also trapped in the large gradient field of the blue 3D MOT due to its large magnetic moment. The magnetic moments and resulting linear Zeeman shifts of the relevant states are presented in Appendix A.

The red MOT utilizes the closed, narrow transition of 7.4 kHz from $^1S_0$ to $^3P_1$ to cool the atoms further down to a recoil temperature limit of 230 nK. The saturation intensity is only $2.95 \times 10^{-3}\,\mathrm{mW/cm^2}$ [73]. To leave the trapped $^3P_2$ state, we have to repump back to the ground state. In our experiment, we first use a 707 nm laser to excite to $^3S_1$. This state decays either to $^3P_1$ or to $^3P_0$. From the long-lived $^3P_0$ state, we have to use another repumper back to $^3S_1$ at 679 nm [76]. Different repumping schemes are available. A prominent scheme uses a single green transition at 497 nm to a $^3D_1$ state [72]. However, the red repumping scheme also allows us to either pump to the $^3P_0$ clock state or the $^3P_2$ state. In particular, the magnetically insensitive $^3P_0$ state is highly relevant for precision spectroscopy.

The level structure description from above applies to ^{88}Sr. For ^{87}Sr, a more complicated hyperfine structure needs to be added. In contrast to the single ground state of ^{88}Sr with $F = 0$, the ground state of ^{87}Sr with $F = 9/2$ is a result of the large nuclear spin of $I = 9/2$ and has consequently 10 degenerate Zeeman levels. These m_F-states have a marginal Zeeman shift and thus have to be energetically separated with an optical Stern-Gerlach technique that induces state-dependent light shifts in the ground-state spin manifold. Appendix B gives a detailed treatment of light shifts in the multi-level structure of strontium.

Concerning the isotope shift of ^{87}Sr, a small 50 MHz shift is present for the $^1P_1$ state. Furthermore, the hyperfine splitting in the $^1P_1$ state is well embodied in the linewidth. A different scenario is present for the $^3P_1$ state, a similarly small isotope shift is enlarged by a large hyperfine splitting. The hyperfine and isotope splittings are incorporated in the level structure of figure 2.1.

2.2 Vacuum system

At the beginning of a cold-atom experiment, a vacuum system is used to create an environment where atoms can be isolated and controlled with laser beams. The design and assembly need to produce and maintain an ultra-high vacuum, while allowing the injection of atoms as well as windows through which lasers can reach the atoms for cooling and controlling. This apparatus section is devoted to the design of the vacuum chamber and its assembly process. An overview of our vacuum chamber is given in figure 2.2. It consists of three sections. The first section is the commercial oven section from AOSense. The oven section is attached via a differential pumping tube to a vacuum cube chamber. This second chamber is connected to the main chamber via another differential pumping tube, to which the glass cell is attached. The entire vacuum chamber has a compact design, which reduces the number of potentially leaky connections and allows placing the entire vacuum chamber on a translation stage (Lintech 1761248 CP02). Placing the vacuum chamber on a translation stage has two advantages. In case of a pressure problem,

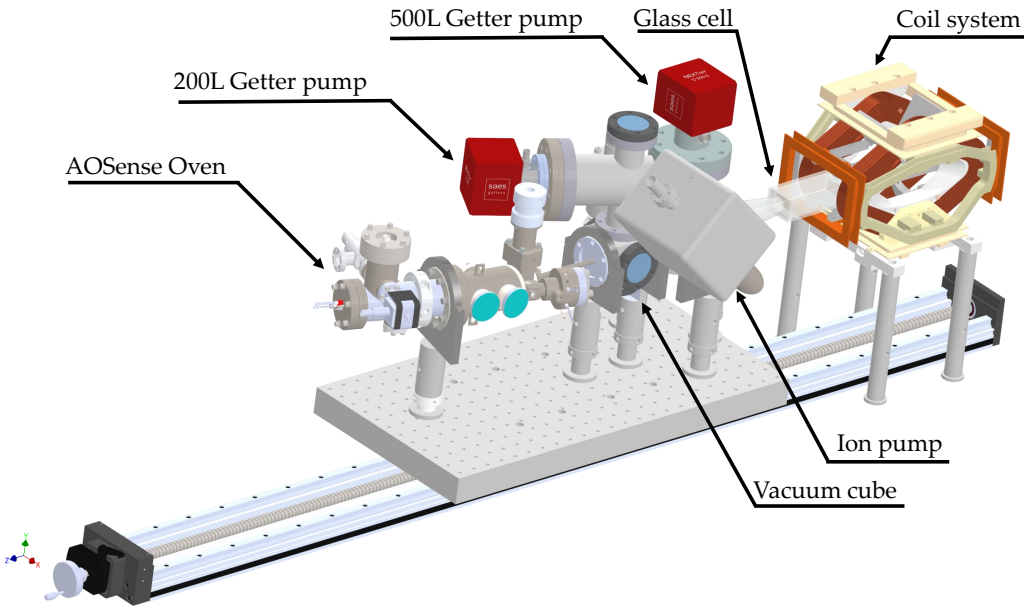

FIGURE 2.2: CAD illustration of the vacuum system. The entire vacuum system stands with posts on a translation stage bread board. The translation stage moves the glass cell between the magnetic coils that are fixed on the optical table.

the vacuum chamber can be retracted and investigated without taking apart any optical structures around it. Secondly, beams can be pre-aligned and characterized at the position of the atoms without the glass cell obstructing the beams.

2.2.1 Oven section

The vacuum system begins with a commercial beam source from AOSense. The beam source is specified to output 10^{11} atoms/s at the outlet of the attached differential pumping tube. At a typical operating temperature of 480 °C, the oven section maintains a specified pressure of $< 2 \times 10^{-8}$ torr. The flux performance is described in the cold atomic beam section of the next chapter 3, whereas this section concentrates on the vacuum performance.

The oven section is presented in figure 2.3. The beam source starts with an oven. The output nozzle can be seen from the side via two CF16 windows. We use these two windows for performing modulation-transfer spectroscopy. The oven output beam subsequently goes through a short Zeeman slower section that consists of a magnetically shielded arrangement of permanent magnets. The blue Zeeman beam enters from the heated Zeeman slower window. The oven heaters and Zeeman window heaters are controlled by a SRS temperature controller (SRS PTC10). We typically operate the oven at an economical 430 °C to save material and reduce wear down of oven heaters and thermistors.

Following the Zeeman slower section are two 2D MOT sections. Permanent magnets create the necessary magnetic field and internal mirrors direct an elongated beam through the atomic beam. The two 2D MOT sections are angled with respect to the oven output and are aligned with the system's output differential pumping tube. Figure 2.3 b) shows the beam angle and atomic beam path. In this arrangement, operating the 2D MOT essentially gates the atomic beam towards the science glass cell and is only on when the 3D MOT is loaded. This avoids a constant atom flux to the glass cell.

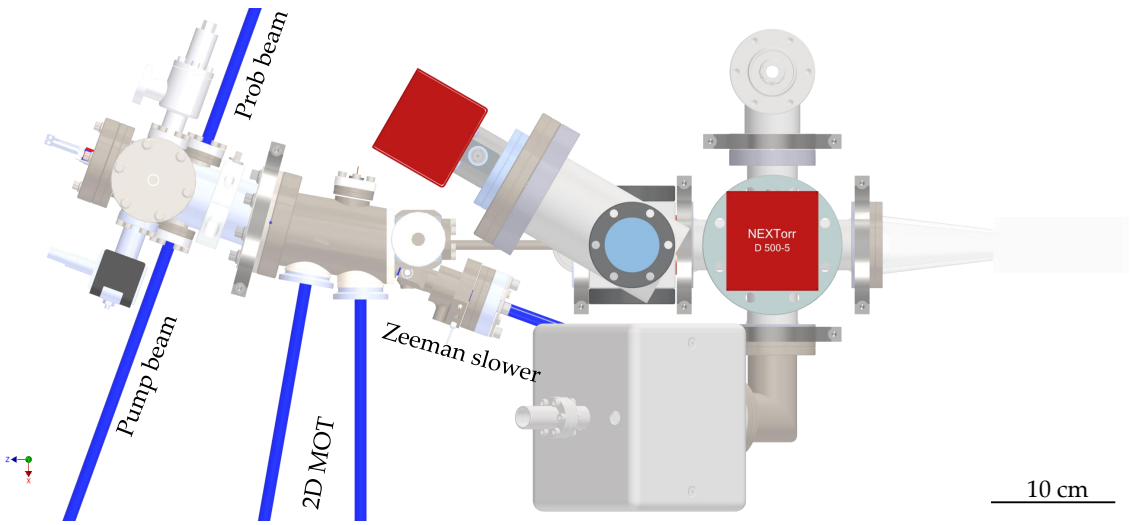

FIGURE 2.3: CAD illustration of the AOSense oven section and how it attaches to the subsequent vacuum chamber. Beam path of spectroscopy, 2D MOT and Zeeman beams as well as the path of the resulting atomic beam towards the main chamber and glass cell.

The beam source is mounted in custom clamps and on variable height posts (Thorlabs BLP01) to adjust the mounting height in the assembly procedure. Initially, we planned to have a vacuum bellow to align the direction of the atomic beam to the next differential pumping tube in the vacuum cube. However, the flange connection and the posts were flexible enough to align it straight to the subsequent vacuum cube chamber.

The atomic source section has a gate valve in case an empty oven needs to be exchanged. A future upgrade will be an extra gate valve after the differential pumping tube to be able to completely detach the oven section from the vacuum cube.

For maintaining a low pressure when the oven outputs its strong atomic flux, the atomic source is equipped with a 50 L/s and 5L/s getter pump and 3 L/s Ion pump (Gamma 3SMT). After receiving the atomic source, the ion pump indicated a large pressure and a sign of potential leakage. It made us hesitant to attach it to our vacuum system, which was designed for handling lower pressure loads from the oven section. After scanning the drawn current against the applied ion pump voltage as shown in the Fowler-Nordheim plot in figure 2.4, we could identify one part of the problem as leakage current. A second part was indeed an increased baseline pressure, as we increased the pressure load by switching on the oven. This is visible in the voltage-independent pressure regime at lower voltages. The higher baseline pressure could be reduced to the specified 2.7×10^{-8} torr by operating the oven for several hours and effectively baking it out.

2.2.2 Differential pumping sections

Following the oven section is the self-built vacuum system hosting the science glass cell in the end. The vacuum system has to maintain the atomic output flux from the oven and create a low pressure of $< 1 \times 10^{-11}$ mbar in the glass cell. In the following, we will explain the design choices for the vacuum system.

Figure 2.2 illustrates the complete vacuum system. It consists mostly of cost-efficient stock parts and can be divided into three parts. First, we have a standard vacuum cube (Vacom CUBE40-316LNS). Above the vacuum cube is a T-chamber (custom-tee CF63-CF40 from Lesker) hosting the first 200 L getter-ion pump (SAES Nextorr Z 200) on one side and

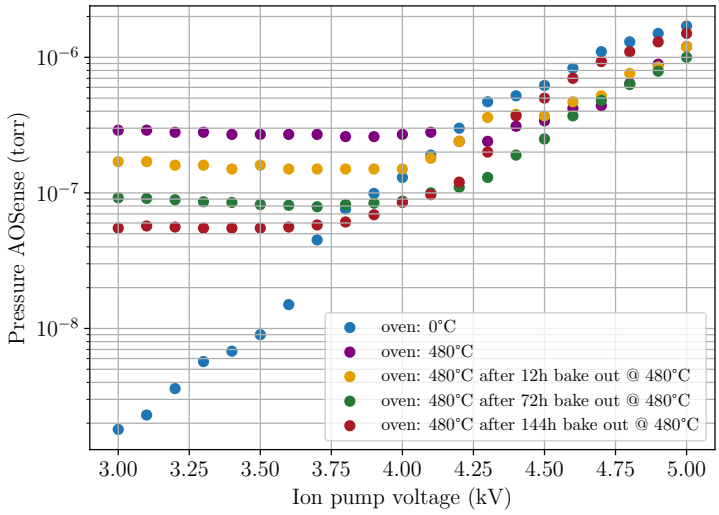

FIGURE 2.4: Fowler-Nordheim plot of the AOSense ion pump. The graph shows the pressure deduced from the Ion pump current load depending on the applied pump voltage and for different oven backing stages. For higher voltage the pressure increases linearly indicating leakage current. For low voltage, the pressure is independent of the voltage indicating the real pressure load for the ion pump. The pressure reduced to an acceptable value as the oven was heated up for the first few hours.

a window on the top side. The getter pump and its internal magnets are oriented away from the glass cell to minimize offset magnetic field gradients at the atomic position. The glass windows (Vacom VPCF40UVQ-L-316L) are attached to the sides of the vacuum cube. The windows allow for the application of 2D Doppler-cooling beams from the side before the differential pumping tube connecting the cube with the main chamber. The differential pumping tube is a custom part made by our workshop. It is made of oxygen-free copper (CWA009) and, at the same time, serves as the copper gasket connecting the vacuum cube to the custom 5-way cross main chamber (Lesker). This differential tube makes the atomic beam path in the vacuum chamber as short as possible, but still serves as a differential pumping tube to reduce the pressure successively from the oven towards the glass cell. The copper tube is 80 mm long and 10 mm inside diameter. The bore dimension is 1.5 times the size of the atomic beam coming out of the 6 mm differential pumping tube with a quoted 17 mrad half-angle divergence. The dimensions avoid clipping of the atomic flux towards the glass cell. A detailed view of the custom differential pumping tube is given by figure 2.5.

The vacuum system continues with the 5-way cross main chamber made of 316LNS stainless steel. Every part in the design is made of this type of stainless steel due to its low magnetic susceptibility. The 5-way cross hosts a second 500 L getter pump (SAES Nextorr D500-5) in its CF63 tube. In hindsight, this tube and the tube for the first getter pump could have been designed bigger since these tubes strongly heated up during the activation of the getter material. We had to reduce the heating of the getter pumps and shorten the activation process to avoid temperature-gradient-induced leaks at the flanges. On the side of the 5-way cross is the UHV valve (VAT 54132-GE02-0001). The other side holds an elbow (Vacom EL40R-316) and a 20L ion pump (Agilent VacIon Plus 20 Starcell). The elbow is in place to direct the large magnets of the ion pump away from the atom position. The purpose of the ion pump is to pump excess chemical compounds that can not be pumped by the getter material or are released during the getter material activation.

On the front side of the 5-way cross is the glass cell from Japan Cell. The cuvette's

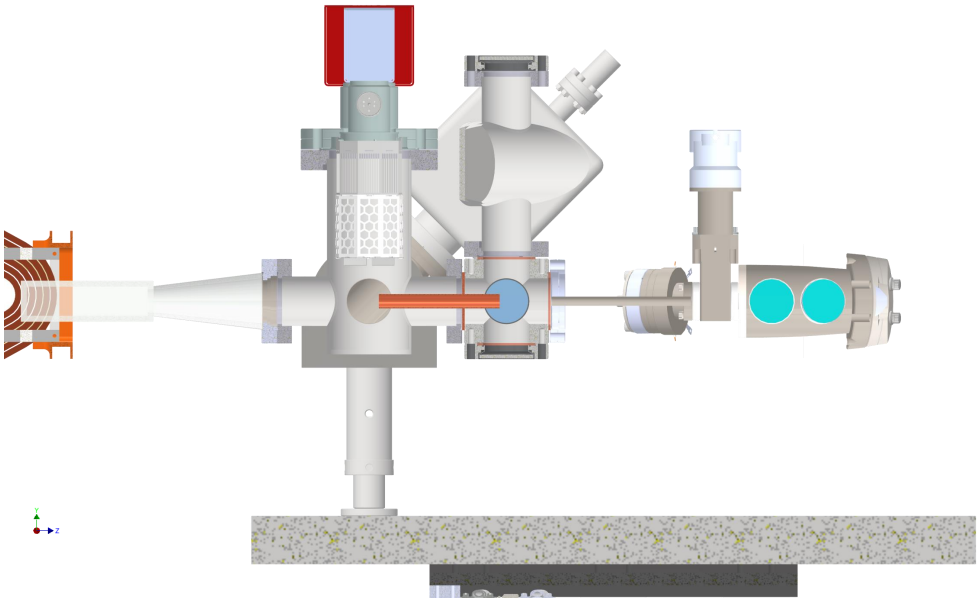

FIGURE 2.5: CAD cross-section of the vacuum system. The cross-section shows the integration of the custom copper gasket as a differential pumping tube between vacuum cube and 5-way cross main chamber.

inside dimensions are $35 \times 24 \times 100$ mm. The glass wall thickness of 5 mm was chosen to be large enough to counteract a bending of the glass wall due to the pressure difference between the inside and outside of the glass cell. The custom glass-metal connection to a CF40 flange has been made by Precision Glassblowing. The glass cell is uncoated since we potentially send in a wide variety of different beams ranging from blue to MID IR.

2.2.3 Vacuum system assembly

The assembly process has several phases, starting with the cleaning of the custom-manufactured parts. The stock parts had cleaning quality standards and were untouched. The cleaning of the parts in an ultrasonic bath involves four steps. First, we cleaned the parts with soap to remove any oil contamination. Then the parts are cleaned in isopropanol for 30 min. This isopropanol is then replaced by fresh isopropanol for another 30 min cleaning run and finished by a final fresh isopropanol cleaning run for 15 min.

After a successful cleaning, the vacuum chamber is assembled in a first high-temperature bake-out setup to get rid of hydrogen in the stainless steel material. We assemble every steel part apart from the valve, glass cell, windows and the oven section, which are baked at a lower temperature. We baked the steel assembly for 5 days at 450 °C while pumping with a turbo pump at a pressure of 1×10^{-9} mbar. We monitored the temperature with a self-built temperature monitor based on a Raspberry Pi that reads out several thermocouple sensors (Adafruit MAX31855). The K-type thermocouples (RS 621-2170) are glued to the chamber with Kapton tape. We control the heating bands (Vacom HB-TD-450-250-5000) via setting a duty cycle on switching power plugs (Antrax SwitchBox). For the high temperature bake out, it is recommended to use silver-plated copper gaskets since the copper can be baked to the knife-edge connection and is hard to remove afterwards. Although the gaskets were rated for 500 °C, the silver layer detached during removal. Small parts

of the silver remained attached to the knife edge connection area and caused problems for bake out 2.

For bake out number 2, we attached the glass cell, windows and angle valve to also bake out as much hydrogen out of their stainless steel connectors. For these parts, we had to ramp the temperature more smoothly, and we did a 300 °C bake out for 7 days. For attaching glass windows, it is recommended to use annealed gaskets to avoid fractures in the glass-metal connection during tightening. Due to the burned silver gaskets, the annealed gasket would not make the window leak-tight. Nevertheless, we learned that standard gaskets also work for windows when they are carefully tightened. The harder gaskets are less penetrated by the knife edge and therefore less lifted upwards by residuals on the knife edge surface. Before reopening the vacuum assembly between the bake outs, we carefully vented the chambers with argon to avoid entering water with humid air.

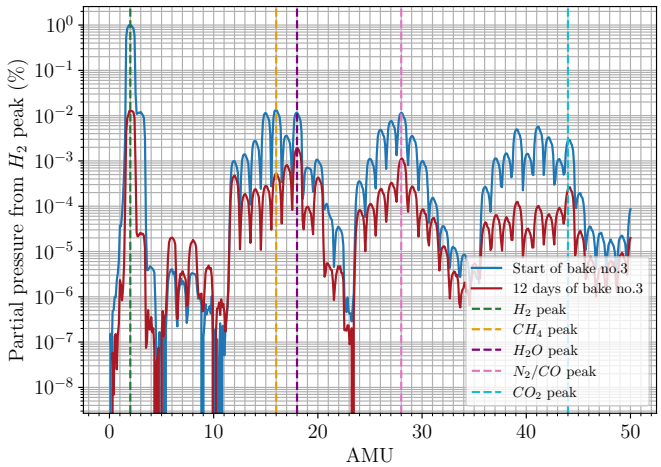

FIGURE 2.6: RGA spectrum recorded at different times of the final bake out. For the interpretation of the spectrum one typically looks at certain components (hydrogen, methan, nitrogen, carbon dioxide, etc) as highlighted. Overall the spectrum needs to lower over time and should not be larger than 10 % of the dominant hydrogen peak. Furthermore, no peak at high mass compound should appear for a successful bake-out and a high vacuum quality.

The vacuum chamber assembling is finished with a final bake out at 200 °C for several days to get rid of any residual water and to speed up the pumping. Before the bake out, we aligned the main chamber with the glass cell parallel to the optical table. During the final bake out we evaluated the quality of the vacuum in two different ways. The first was an occasional use of a residual gas analyzer (Lesker ELE1MA000). The RGA does a continuous mass spectroscopy by ionizing the influx. It outputs a spectrum as in figure 2.6 which needs to be analyzed to make a conclusion about the vacuum quality. First and foremost, we had to bake out the RGA by itself to get reliable data and not release any components into our main chamber. The spectrum analysis concentrated on certain components. The signal is referenced to the hydrogen peak (2 AMU) which is the dominant virtual leak source stemming from the stainless steel material. Together with CO_2 (44 AMU) is strongly reduced with the bake-out. Nitrogen and CO peaks at 28 AMU would indicate an air leak. An initial contribution from the H_20 peak (18 AMU) and the residual byproduct of hydrogen and carbon methane CH_4 (16 AMU) is always present but is reduced with the bake out over time. Any compounds with a mass higher than 50 AMU indicated contamination with oily substances, which was not the case for us. All in all, the components that are 10 times smaller than the hydrogen peak indicate an acceptable UHV [77].

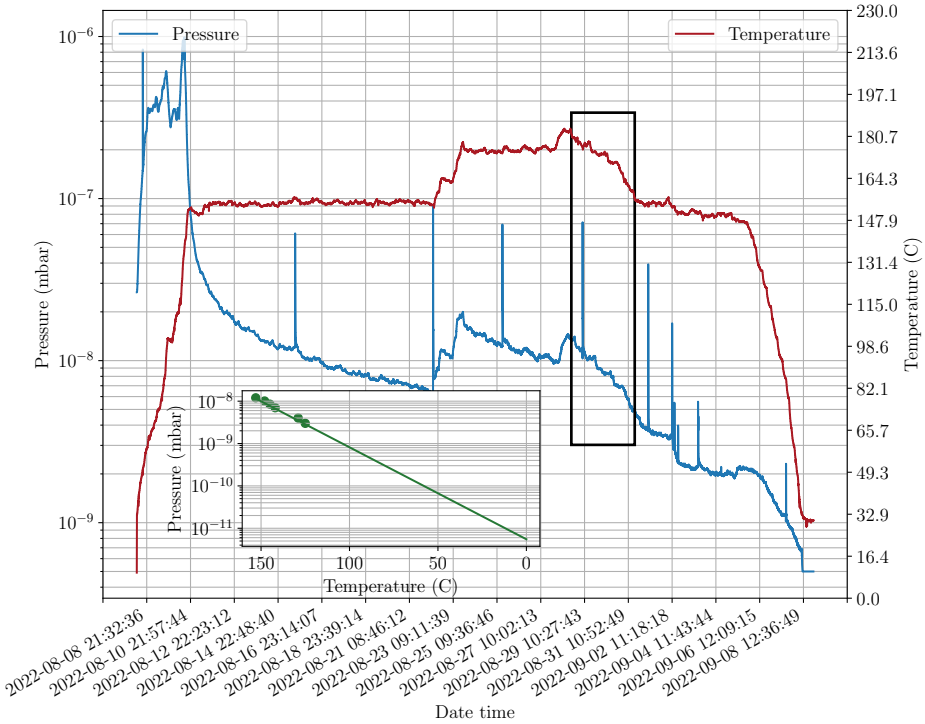

FIGURE 2.7: Temperature and pressure evolution during the final bake out. The temperature has been measured at the vacuum cube. Spikes in the pressure graph stem from RGA measurements temporarily increasing the pressure in the pressure gauge region. At the very end, the pressure decreased below the measurement threshold of the pressure gauge. The inset shows the pressure with decreasing temperature from the data box in the full graph (green dots). The green graph shows the extrapolation of the pressure to room temperature indicating a sufficient UHV pressure in the 1×10^{-11} mbar regime.

Another evaluation approach is the extrapolation of the pressure when ramping down the temperature a bit. An evolution of pressure and temperature over time is plotted in figure 2.7. As the temperature goes down, the pressure also goes down and can be extrapolated to room temperature, giving an extrapolated pressure in the 1×10^{-11} mbar regime. After 30 days of bake out at 200 °C we decided to ramp down the temperature and activate the ion and getter pumps. During the activation of the getter pumps, we kept pumping because the heating and release of the getter material releases a lot of extra material. The material itself and the built-in ion pumps should take care of the material release, but we played it safe and continued to pump with the turbo pump. Afterward, we tried to activate the ion pumps but saw no current signal from them. It can happen that the pressure is too low for the ion pumps to start the impact ionization process and effective pumping. Trying to increase the voltage or knocking on it did not give a signal. Only when switching on the oven and increasing the pressure load, the ion pumps showed a pumping signal. Most likely during the bake out we activated the getter pumps already. The final pressure reading on the VacIon pump is 9×10^{-12} mbar. The 500 L getter pump in the 5-way cross reads 2×10^{-11} mbar and the 200 L getter pump in the vacuum cube reads 1×10^{-10} mbar. We did a final leak testing with the ion pumps themselves by applying helium to every flange connection. The RGA would have been a very sensitive probe for that, but we did not want to connect it to the final vacuum setting.

2.3 Magnetic fields

Apart from the vacuum chamber, magnetic field coils are another essential component of cold atom experiments. Different types of coils are used for specific tasks ranging from gradient fields, guiding fields, and earth magnetic field compensation. They need to be well-planned and implemented to act accordingly on the atoms and fulfill safety requirements. Lead times and prices from coil winding companies forced us to build the magnetic field system ourselves. The following section outlines the design choices and manufacturing process of our magnetic field system. The magnetic fields include strong fields for the MOT and precise compensation fields.

2.3.1 MOT magnetic field coils

A typical magnetic field system consists of two types of coil pairs. A field coil that is switchable between an anti-Helmholtz (AH) and Helmholtz (HH) configuration for gradient and homogeneous fields. The second type of coils consists of three compensation coil pairs creating independent offset fields in each direction. The design and dimensions of these coils had to fulfill the following requirements:

- In AH configuration the coils should create a strong gradient field of 50 G/cm which is typically used for the blue MOT
- In the HH configuration - to be used in a later stage of the experiment - the homogenous field should reach at least 600 G to enable significant optical dipole coupling on the clock transition in ^{88}Sr
- The homogeneity of the strong field and the associated Zeeman shifts have to be less than the linewidth of the clock transition
- The maximally available current is 200 A at 30 V
- The compensation fields should be at least 3G for Earth magnetic-field compensation and guiding-field applications
- The coil designs should not block any beam access to the atoms
- The resistive heating should be reasonable to avoid thermal drifting of the optics around the glass cell

Design

With the requirements at hand, the design converged to diamond-shaped coils, which are oriented with the long axis parallel to the long axis of the glass cell. The design is inspired by the strontium machine of the Endres group [78]. The objective and glass cell between the coils and several different beams dictated the shape and size. The key dimensions are summarized in Table 2.2.

A CAD drawing of the coil structure in figure 2.8 shows how it is designed around the obstacles and includes several laser beams entering the glass cell towards the center position. The diamond-shaped coil from the side allows many different beams to enter from the x-z plane. Another important beam setup is a crossed optical dipole trap. With one beam coming from the side, the second beam has to come from the top. The top dipole beam together with the top and bottom MOT beam passes through the glass cell under an angle of 50 °.

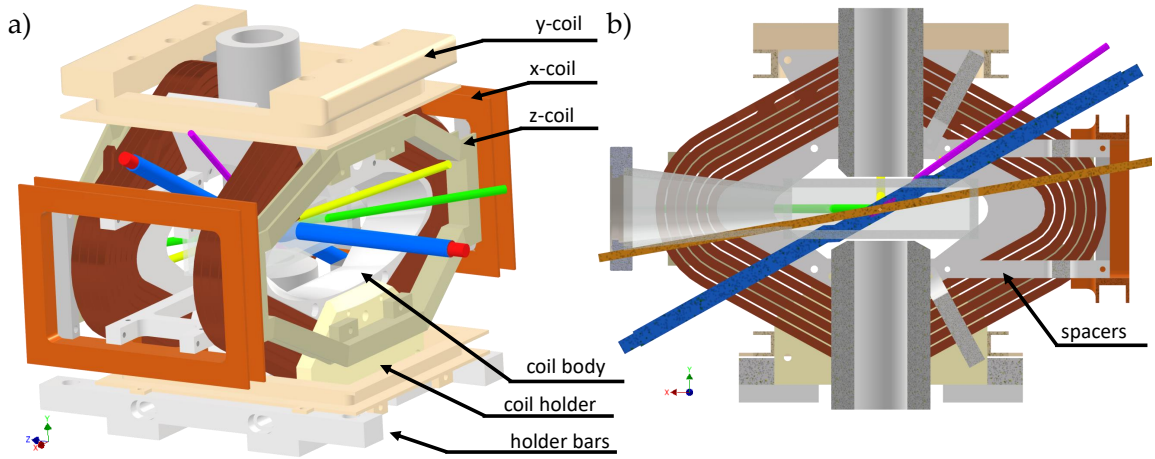

FIGURE 2.8: CAD Design of MOT field and compensation field coils: The mail coil consists of the hollow copper wires (bronce) glued together with the coil body. The coil body is mounted on a coil holder both made out of EPGC material. The coil structure is mounted on holder bars which allow for variable post height beneath and allow a variable distance of the coils via slotted holes. In between the coils are spacers for stabilization against mechanical vibrations. The dimensions of the coils are mostly determined by the objects that need to fit in between (microscope objective and glass cell) and various laser beams. The large MOT beams are shown in blue and several smaller horizontal beam under extreme angles determined by the cell dimensions and Brewster angles.

All in all, the entire coil structure is modular. It consists of the coil body around which the copper wire is wound. Having a coil body makes the winding easier and provides mounting points for additional holding structures. Such holding structures are spacers in between the coils that give the coil stability. The compensation coils are mounted at very specific points. The compensation coil holders are 3D printed and fit tightly around the main coil structure to be as close to the atoms as possible in order to potentially provide a bit stronger offset fields than just for compensation purposes.

Another important part of the design process is the material choice. Especially when dealing with materials in magnetic fields, magnetizing the holding structure over time and creating a varying offset is a problem for the precise interrogation of the atoms. Another issue is the eddy current during magnetic field switching. The induced eddy current can create strong temporary magnetic fields. These eddy current fields are enhanced at surfaces perpendicular to the coil's axis. Therefore, the coil body and coil body holder are manufactured out of epoxy glass cloth material (Hippe EPGC) with no magnetic permeability. For the screws, only A4 stainless steel screws with low magnetic permeability qualify. For the coil mount holder, we used aluminum bars that have a small enough surface along the main coils to induce no significant eddy currents.

During the operation, the two coils repel or attract each other. We validated the design strength against these forces with FEM simulations in Inventor. Appendix C.2 derives an expression for the maximal forces acting on the coils. Assuming $N = 23$ winding, a maximal current of $I = 200\,\mathrm{A}$ and a coil distance of $D = 50\,\mathrm{mm}$, we obtain a steady force of $F = 213\,\mathrm{N}$. However, in a fast switching process, induced currents increase the peak force to $F = 3.6\,\mathrm{kN}$ assuming a switching time of $t_{switch} = 500\,\mu\mathrm{s}$.

Figure 2.9 shows the simulated displacement and stress. The figure 2.9 a) shows the displacement when the force acts on the coils. The outsides are moving together over a distance of maximally $70\,\mu\mathrm{m}$. This displacement is largely dependent on the E-Module of the EPGC spacer material and the glue. Both E-moduls can be approximated with 7 GPa.

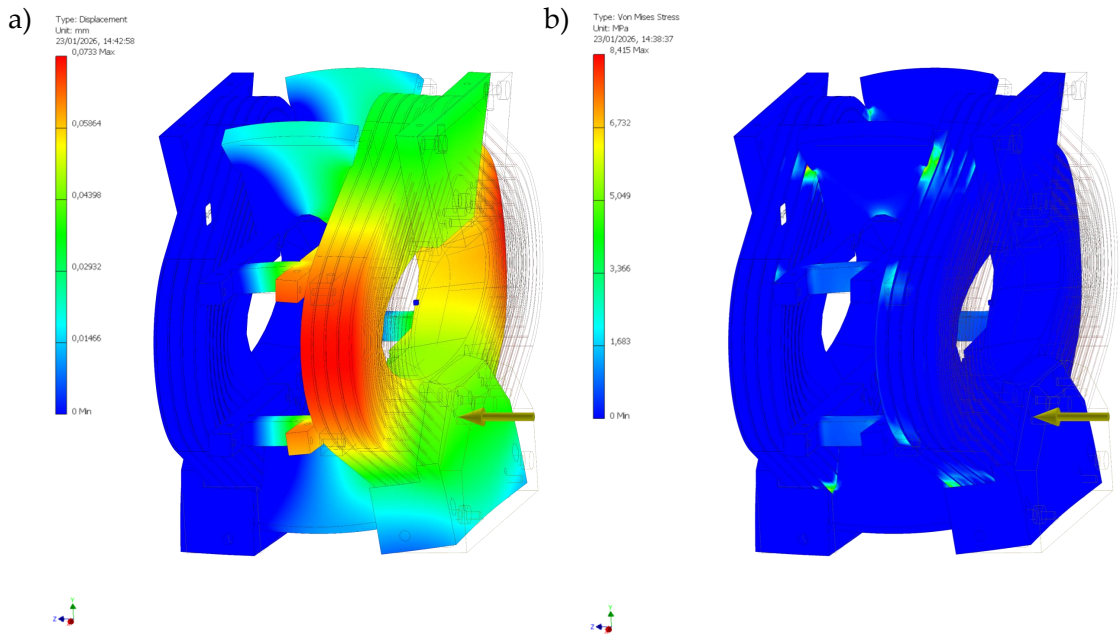

FIGURE 2.9: FEM simulation of the main coil structure under induction induced magnetic force of the coils during a fast switching process of 200 A in 5 ms. In a) the negligible displacement of the coils structure is shown. Subfigure b) shows the stress in the coils which is significantly lower than typically 80 − 150 MPa deformation stress of fiber enforced materials.

A slight movement will always be present due to the strong force acting on the assembly.

To evaluate whether the design is strong enough, one should analyze the stress in the structure as shown in figure 2.9 b). The stress should not exceed the maximal tensile, compressive, and flexural strength of the Material. The result of the FEM simulation is that the obtained 8.5 MPa are significantly lower than the 80 − 150 MPa strength of the EPGC material. Therefore, the holder structure should withstand the forces from the fast switching of the coils.

Due to the coil's complex shape, no company was willing to manufacture it. Therefore, we had to incorporate the manufacturing process into the design. Figure 2.10 a) shows the winding tool. The plan was to wind the copper tube around a separate coil body. During winding, the coil body is screwed onto two metal plates that restrict the sides. Additional holes in strategic positions hold clamps to secure the wire. The rectangular side holes allow entry from above and below for bending the copper tube in place. Although the copper tube was annealed, it was not soft enough. We had to gently hammer the tube into shape after each quarter turn, especially over the diamond-shaped coil body edges as shown in figure 2.10 b). To monitor the coil's temperature, we embedded 10k thermistors during winding.

We designed the coil body wide enough that the 5 mm × 5 mm copper tubes could be covered with an insulating tube (RS 668-1245). As the winding progressed, the copper tube naturally shifted into the next layer. Insulation and bending around the corners were taken into account in the dimension of the coil body thickness to provide a snug fit. At each turn, epoxy was applied generously to ensure strong bonding. The epoxy (RG Faserverbundwerkstoff GmbH Epoxy L and EPH161 Hardener) was subsequently baked for 15 h at 90 °C to cure and harden. Since we wrapped the winding tool in Teflon tape, the epoxy did not bond strongly to the tool, and the final coil could be nicely removed as shown in figure 2.10 c).

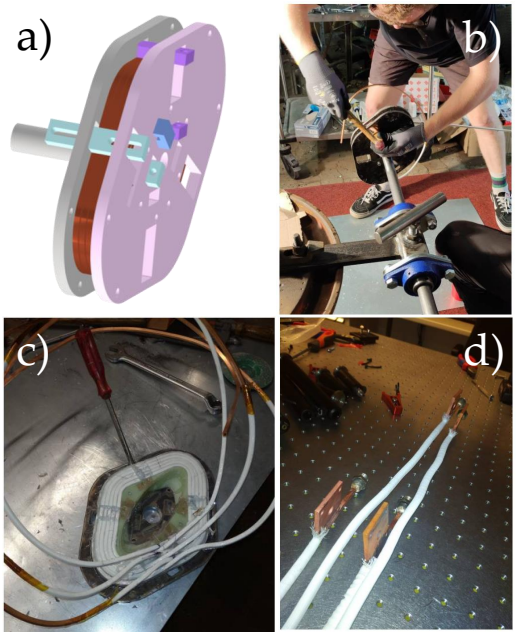

FIGURE 2.10: Coil winding procedure. a) We designed 2 steal plates which hold the coil body and bound the copper wire sections to each other for good glue contact. The plates hold the copper tube and can be rotated around an axis. b) At the position of the wire jumps the plates have openings to force the copper tube in place. c) Once the copper wire is wound in 3 independent sections the glue must be hardened under heat and subsequently forced out of the cast. d) The connection plate and water connector that are soldered to the copper tube.

Instead of a continuous 60 m roll of copper tube, we received 6 m pieces. This broke up the winding into 3 sections with two layers (8 turns) per section. We measured the required lengths for each layer, and sacrificed the last turn of the 6th layer to maximize the distance of the water connector to the optics on the table. The electrical connector comprises a 4 cm×4 cm plate with an M8 hole for the cable and a stainless-steal knifed water connector, which were hard soldered with copper solder for efficient electrical connection and cooling across the connection area 2.10 d).

Water cooling and interlocks

An important design consideration is the type of copper wire which is used in the coils. In the coils, we use a 5 mm×5 mm copper tube which provides cooling by a water flow through its 3 mm×3 mm center tube. There is a trade-off between a cross-section for minimal resistance and a cross-section for the maximal water flow. Appendix C.3 estimates the expected heating from a full coil. However, the final coil design changed to 3 times 6 m long sections, which consequently reduces the estimated heating to 5 °C. In the end, we measure the flow rate and temperature increase in the full cooling setup, because water distribution, tubing and additional cooling loads influence the final cooling power. The full water self-built water cooling system is presented in 2.11. It supplies each coil section in parallel. Additionally, the switching circuit components require cooling and are mounted on a water-cooled aluminium board. The system consists of a water pump (HELIX V409-1/25/E/S/1-230-50) that is controlled by the CO-ER System to pump deionised water from the reservoir. At the moment, we use a temperature controller (PD6100) to monitor the temperature of the reservoir. In the future, we could use the controller to stabilise the water temperature of the reservoir by actuating the electronic valve (Siemens

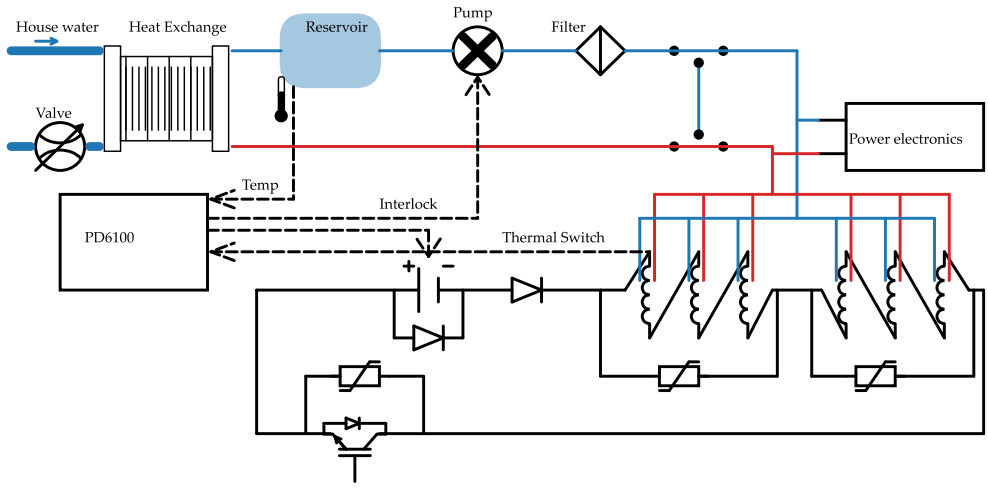

FIGURE 2.11: Circuit diagram and water cooling system of the main coils including interlock signal distribution.

TABLE 2.2: Features of the main coils.

Property	Value
Resistance	20 mΩ
Number of turns per coil	$2 \times 8 + 1 \times 7 = 23$
Wire gauge	5 mm×5 mm OD and 3 mm×3 mm ID
Water flow each section	1.5 L/min
Total temperature increase	1.5 °C
Nearest separation	50 mm
Helmholtz field (longitudinal)	2.5 G/A
Anti-Helmholtz gradient (vertical) Y	0.3 (G/cm)/A
Anti-Helmholtz gradient (longitudinal) Z	0.33 (G/cm)/A
Anti-Helmholtz gradient (horizontal) X	−0.16 (G/cm)/A

SQS65) to control the house water flow into the heat exchanger. At the moment, the stability is not important, and the cooling power of our water system is large such that we just keep the electronic valve at 90 % flow and keep the reservoir temperature at 17 °C. Our standard tubing is 10 mm black PVC tube (RS 144-7879) for algae growth suppression and knife cutting connectors (Timmer C-10 series) for safe connection. For the heat exchanger, we use pipes with larger cross sections of 30 mm diameter.

To safely operate the big coils at high current and avoid any meltdown of the coils and power electronics, the power supply gets an interlock signal from the water pump controller and water temperature controller. An additional interlock signal comes from thermal switches that we glued onto the coils. Additional interlock branches, such as a flow sensor after the water pump or a water sensor around the coils, on the table or a water level sensor for the reservoir, can be added. All these sensor signals are processed by the temperature controller and trigger the interlock at programmable threshold values. In conclusion, the dimension of the copper tube and water cooling system allows us to operate the coils at the highest current and fast cycle time with virtually any heating. The properties of the main coils are presented in table 2.2.

Field validation

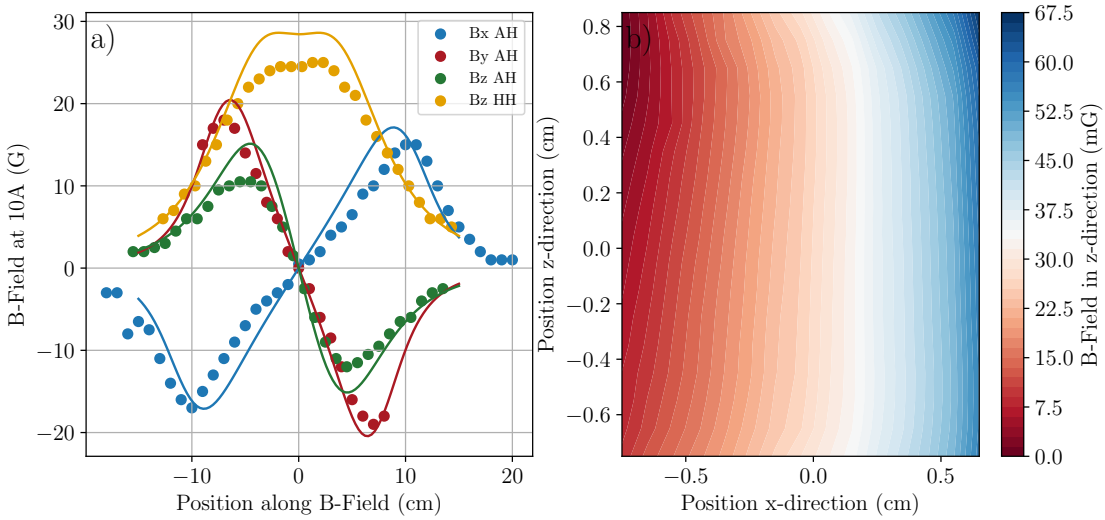

FIGURE 2.12: a) A comparison of the measured field (dots) to the calculated field (line) in AH and HH configuration at $I = 10\,\mathrm{A}$ of current. The fields were measured with a Hall Sensor. b) The field homogeneity around the center point in the x-z plane was measured with a more precise Flux Sensor.

In the following section, we validate the magnetic field of our coil design by comparing it to field calculations. Appendix C.1 presents the underlying formulas for our specific diamond-shaped coils. The resulting field in AH and HH configurations is presented in figure 2.12 a) and b). We used a Hall Sensor (TI SS494) to measure the field in the two configurations. In figure 2.12 a), it is visible that the field falls off more quickly from the center but creates the required gradient field at the center. A gradient field of 50 G/cm is achievable with 150 A. In the HH configuration, a slightly lower field has been measured than expected. With the present coils at maximal 200 A we will not reach 600 G but rather 550 G.

For validating the field homogeneity, we measured the field around the coil center with a more precise flux sensor (Stefan Mayer Instruments FLC 100). The data in figure 2.12 c) shows a field gradient of 60 mG. The field increases towards the outlet of the copper tubes of each coil section. One could have potentially minimized this gradient by arranging the coils counterparallel around the glass cell. In z-direction, the homogeneity is an order of magnitude better. This field inhomogeneity along x has an effect on several atomic transitions via the Zeeman shift and can be calculated with equation A.1 as presented in A. All in all, only the $^3P_2$ clock transition is strongly affected by the field gradient. However, the inhomogeneity does not affect a robust operation of the narrow red MOT on the $^3P_1$ transitions as the spatial Zeeman shift is an order of magnitude lower than the linewidth.

Current switching electronics

We opted for the simplest electronic circuit design at the beginning of our setup. It was important to establish a sufficiently large magnetic field gradient and a stable field for both blue MOT (bMOT) and red MOT (rMOT). Figure 2.11 shows the electrical circuit.

The power supply (Delta SM30-200) provides a maximum of 200 A of current at maximal 30 V. The power supply and the IGBT (Mitsubishi Electric: CM450DX-24T) are controlled by isolated gate drivers and thus create an isolated floating circuit for the coils. To

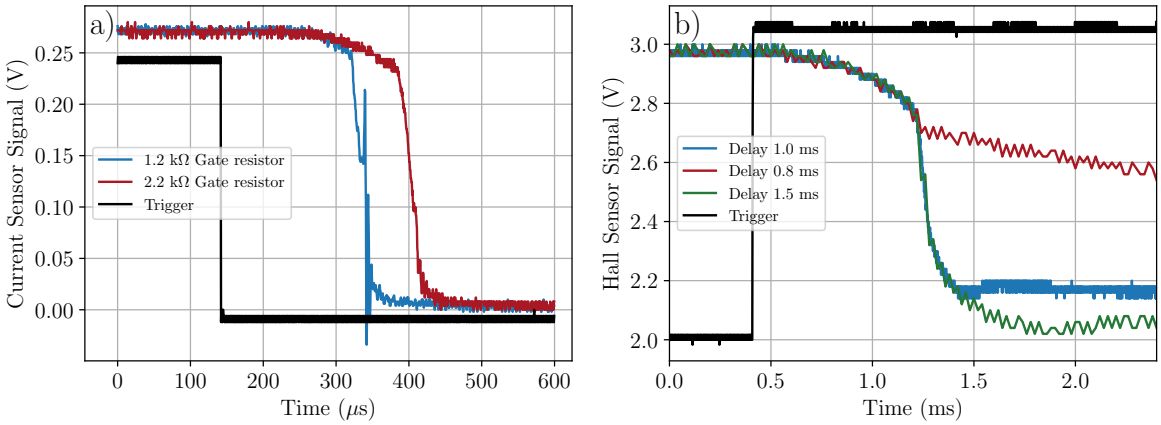

FIGURE 2.13: Characterization of the switching process of the main coils with an IGBT. a) The current sensor indicates detrimental spikes during the fast switching which vanishes when increasing the gate resistor of the IGBT driver. b) Switching process from a large gradient field to a small gradient field for the two-stage MOT sequence. The time between power supply disabling and reenabling is scanned and the current response is recorded. We choose a sequence that allows reasonable fast but soft switching in 1 ms without stressing the IGBT and coil structure too much.

protect the circuit components against reverse currents, we included two power diodes (Semikron SKKE6001/2 and Powerex Powrblok GP 800A600V). Additionally, varistors (EPCOS 872260B0321K001) are in parallel to each coil and IGBT to protect against voltage spikes during fast switching sequences. To reduce voltage drops over the 10-meter cable run to the coils, we used relatively large cable cross sections (CSE H07V-K 70mm^2).

The power supply has a current stability of 2.5 mA$_{RMS}$. With the equations in A, the current stability can be translated into a Zeeman shift from the gradient field inside the typical MOT region of 0.5 mm. For both isotopes, the Zeeman shift gives about 500 Hz, which is acceptable for the rMOT transition and should support stable rMOT operation. An alternative approach could have been active current stabilization using a current transducer and feedback on the analog voltage control of the power supply. We have a current transducer (Signaltech CT400), though it has only been used for debugging purposes, as described in figure 2.13. Another additional feature yet to be implemented is a H-bridge to switch between the AH and HH configurations. Currently, only the AH configuration is used. When considering the creation of the H-bridge, we looked into high-power relays (Layher 640 series), allowing for isolated switching, provided that the switching time does not limit the experimental sequence.

Although IGBTs are generally designed to handle large currents, in our particular setup, the IGBT caused problems during fast switching. Initially, we planned to switch as quickly as possible from the bMOT gradient field to the rMOT gradient field. However, the large coils induced significant inductive spikes, as observed with the current transducer and shown in figure 2.13 a). For a high current of around 150 A, we permanently damaged an IGBT. We addressed this issue by using large gate resistors in the IGBT driver (Isahaya VLA536-01R), which slowed down the switching process from a few microseconds to a few hundred microseconds.

Although this made the switching safer, it was still too fast, and measurable vibrations occurred when switching off the coils at high currents. To overcome this, we developed a switching sequence that reasonably quickly transitions the current from approximately 150 A for the bMOT to about 7 A for the rMOT. This sequence is presented in figure 2.13 b). This approach only works in constant voltage mode. It begins by changing the voltage

TABLE 2.3: Features of the compensation coils.

Property	x-axis	y-axis	z-axis
Resistance	0.5 Ω	0.7 Ω	0.9 Ω
Name	horizontal	vertical	main/longitudinal
Number of turns per coil	63	64	50
Wire gauge	1.5 mm	1.5 mm	1.12 mm
Nearest separation	246 mm	146 mm	169 mm
Helmholtz offset field	0.6 G/A	2.2 G/A	3.75 G/A

setpoint to match the rMOT current, then switches off the power supply first, followed by switching off the IGBT. During this phase, the remaining and induced currents are safely dissipated by the varistors since the power supply is turned off and not driving against the IGBT. After an experimentally determined switching time, we turn the IGBT back on and re-enable the power supply. Using this sequence, we achieve switching times of approximately 1 ms, which are fast enough to reliably transition from the bMOT to the rMOT without causing damaging vibrations.

2.3.2 Compensation field coils

In the last section, we describe the compensation coils, which consist of a pair of coils in each spatial direction. These coils serve two main functions: to shift the position of the red MOT and to establish a decent guiding field in every direction. Since the rMOT is highly sensitive to frequency changes, we do not require large currents. Instead, we optimized the circuit and design for high current precision rather than for generating large fields or fast switching. The design and winding of the compensation coils closely followed that of the main coils. We used Kapton-insulated wire (RS 779-0741) to wind the copper wire directly around the 3D-printed structures. For each coil, a thermistor was incorporated to monitor the temperature, especially if the current needs to be pushed towards maximal values. The key features of the coils are summarized in table 2.3. We utilize laser current drivers (Thorlabs LD3000) as power supplies, which provide a current stability of 12 μA_{RMS} at 1.0 A. To switch the direction of the magnetic field, we use mechanical relays (Debo SRD-05VDC-SL-C) arranged in an H-bridge configuration around the two coils. The switching times of the compensation coils are limited to sub-500 μs.

2.4 Laser systems

Lasers are the tools which we use to manipulate and control the strontium atoms. The level structure of strontium is largely accessible with diode lasers. This established laser technology allowed us to build some of the lasers ourselves. In this section, the structures and purposes of each laser system are presented.

2.4.1 Blue laser system

The first laser system is the 461 nm diode laser setup driving the 30.5 MHz $^1S_0 \rightarrow ^1P_1$ transition. The laser system provides light for frequency-modulated spectroscopy, 2D MOT, and Zeemann slower light for the AOSense atomic beam source, 3D MOT light, imaging light, and an extra cooling beam called the mini Zeeman slower. The blue laser system has been set up by my colleague Meny Menashes and described in detail in his thesis [79].

The blue laser source (Moglabs ILA461) employs an external-cavity diode laser (ECDL) configured in Littrow geometry and an injection locking of a secondary diode. Both the ECDL and the injection module utilize the same diode (Nichia NBD4916), generating the total power required for the system. The full laser system is shown in figure 2.14. The ECDL port has an output power of 200 mW and is shaped with a 2:1 anamorphic prism pair (Thorlabs PS875-A) before it is split into a spectroscopy and imaging beam path.

The spectroscopy beam path dictates the laser output frequency with respect to the ^{88}Sr resonance and thus needs to be tunable. For that, we use a broadband AOM (GH 3350-199) in a double-pass configuration. It can be tuned from $250 - 420$ MHz and covers the full range of isotope shifts. Together with another 350 MHz AOM, the ECDL laser frequency is 220 MHz red detuned from the atomic resonance. In that way, frequency-tunable beam paths are derived from the main laser frequency with standard 110 MHz AOMs in a double-pass configuration. Pump and probe beams are sent with PM fibers (OZ QPMJ-3A3A-488-3.5/125-3-10) to the spectroscopy setup. The locking setup sends the error signal to the laser driver (Moglabs DLC502) with built-in feedback branches for the grating piezo and laser current. Sending blue light through PM fibers over 10 m length, requires good polarization maintenance. Accordingly, cleaning PBS cubes are placed before and after fibers and the polarization quality is checked and maintained with a polarimeter (SK SK010PA-VIS).

Concerning the AOM control, we either use the option of a self-built analog AOM driver or a DDS (WieserlabsWL-FlexDDS-NG) for higher timing precision. The full experiment is controlled and synchronized by an ADwin Pro II processor, which is configured with the software infrastructure qcontrol, developed in Munich [80]. The RF signals are typically amplified with 2 W RF amplifiers (minicircuits ZHL-2 and ZX60-100VH+ for 80 MHz AOM). The DDS is employed for the imaging beam path, where precisely timed light pulses are created for the free-space imaging technique. The imaging beam is created with a double-pass AOM (GH 3110-120) and can also be used with standard absorption imaging. Since the blue $^1P_1$ transition is broad and small amounts of leakage light can cause strong light scattering with the atoms, every light port has a shutter. The shutters are based on servo-motors and are controlled by an Arduino, which has been developed by my colleague Leon Schaefer.

The second part of the blue laser system is the injection module output. 30 mW from the ECDL is injected via the optical isolator cube into the laser diode to output 500 mW at 500 mA. A separate controller (Moglabs ILD605) controls the temperature and current of the injection diode. The diode current is actively controlled to maximize the output power. This ensures a stable injection locking. Since it is the same diode as the ECDL, the injection module beam is similarly beam shaped and branches out via PBS cubes into the 3D MOT double pass AOM setup for 3 individual MOT beams, the 2D MOT beam double pass AOM and a single pass AOM for the mini Zeeman slower beam.

The 2D MOT beam setup has another purpose of being the second imaging beam that we need for our free-space imaging technique. For that, we need enough power to have an intensity at the atoms that is reaching an intensity much higher than the saturation intensity of the blue $^1P_1$ transition. Since the 2D MOT beam is not used after the 3D MOT, we recycle the beam during the free-space imaging and shutter of either beam path. For the free-space imaging, the alternating pulse generation of both beams needs to be in sync. Therefore, the AOMs of both beams are controlled from the same DDS sub module. To generate clean light pulses and avoid hysteresis during switching, we coupled the AOM and the fiber while the beams were continuously switched on and off.

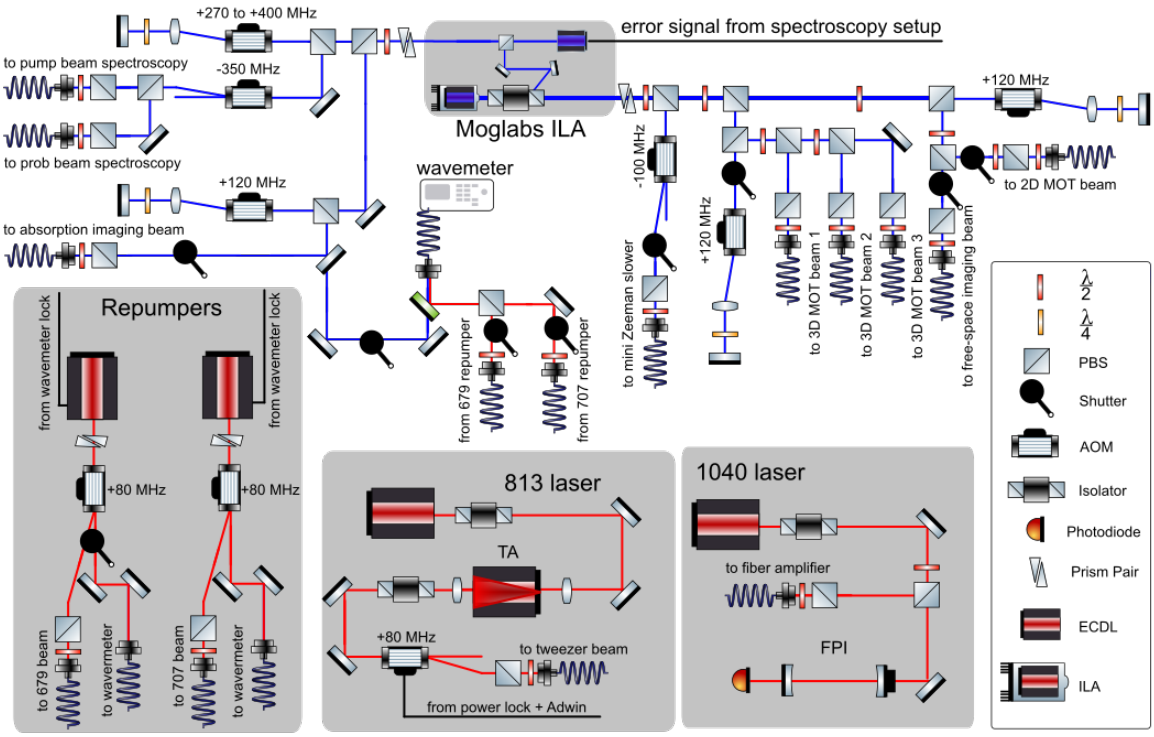

FIGURE 2.14: Blue laser system, dipole trap laser systems and repumper laser systems. Figure created with [81].

2.4.2 Red laser system

The red laser system is driving the narrow transition to the $^3P_1$ state and consequently requires precise frequency stabilization. The overall system design is an ECDL (Toptica DL Pro Narrow LW) amplified by two injection lock modules (Thorlabs HL6738MG diode and Uchio HL69001DGz diode). The laser system provides light for 3 MOT beams, a cooling beam for Sysiphus cooling in the tweezer, a beam to lock the laser to a cavity, a beam to offset-lock the OSG beam laser, and light for lasing mode diagnosis on a Fabry-Perot interferometer. A diagram of the full laser system is given in figure 2.15.

The injection lock modules are home-built. The diode controller (Thorlabs ITC102) provides typically 110 mA of laser current and acts on a TEC in the module structure for temperature stabilization. The diode collimator (SK 20C-A4-02) collimates one axis of the diode output beam. We couple ECDL light out of a fiber into the diode via an optical isolator (Isolator I-67SD-5M and Soliton IPO.189.13407).

The injection locking consists of two steps. First, we merge the diode's lasing mode with the ECDL mode on the FPI (Thorlabs SA30-73). Once the diode is solely lasing on the desired frequency, we optimize the mode stability by modulating the laser current and observing the reflection from an interference filter (Laser Optik L-07557-02). The interference filter is tuned to maximal transmission at the desired laser frequency. Once the injection lock diode falls out of the lock, the reflection increases. The injection coupling is optimized for the broadest current plateau at minimal reflection. With 2 mW in the injection beam, we obtain 65 mW from the Thorlabs diode and with 1 mW we obtain 80 mW from the Ushio diode.

Similarly, the interference filter reflection is used for automatically relocking the injection modules. For that, we record the interference filter with a RedPitaya controller. If the interference reflection increases above a threshold, the RedPitaya module modulates the

laser current until the reflection jumps back to its locked value. For confirmation of proper diode injection, we look at the peaks on the FPI and compare it with the expected lasing mode. If we still have a small parasitic mode in the spectrum, the current modulation sequence is triggered again, and the diode is relocked again

After amplification, each beam is sent to dedicated double-pass AOMs (GH 3350-125) to generate the red MOT light and the stirring light. The RF source is the Wieserlabs DDS with which we can generate programmable frequency ramps and frequency shifts. For power ramps, we use VCAs (minicircuits ZX73-2500+) before the amplifiers (AA AMPB-B-34-10.5). The frequency of the laser is set in between the $^3P_1$ $F = 11/2$ and $^3P_1$ $F = 9/2$ transitions, such that one 350 MHz AOM is shifting the frequency down to set the rMOT beam frequency and the second AOM shifts the frequency up for stirring light. After the double-pass AOMs, both beams are recombined on a PBS and split into the horizontal MOT beams and vertical MOT beams. Due to the PBS and recombination, we only send stirring light in the vertical beams. A small part is still sent to the horizontal beam path and reflected off into the Sisyphus cooling beam path. The cooling beam can only be switched on independently of the MOT beams via shutters.

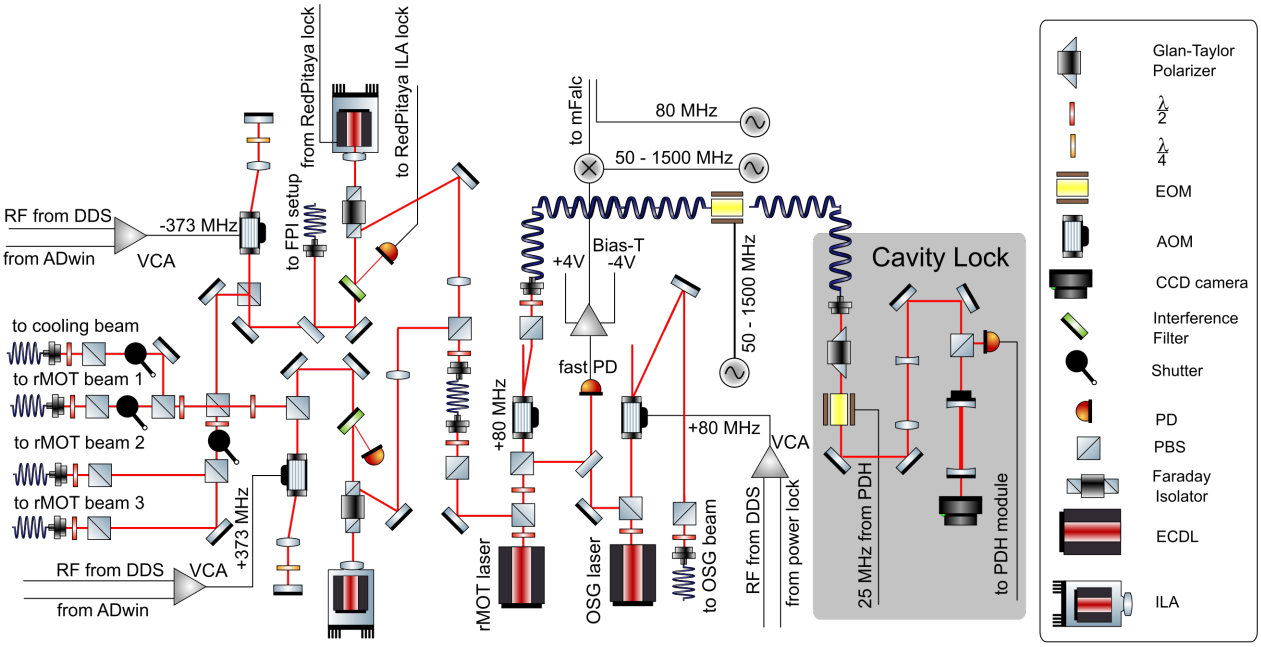

FIGURE 2.15: The red MOT laser system including the setup for the cavity lock and offset lock to the OSG laser system.

Frequency stabilization

A precise frequency stability is achieved through a PDH lock to a high-finesse cavity system (SLS 106020-4). The cavity reference is characterized with a cavity ring down measurement as presented in the inset of figure 2.16. The fit of the transmission decay gives a finesse of $F = 256256 \pm 186$ which translates into a cavity linewidth of 5.85 kHz.

The vacuum chamber of the cavity system rests on a vibration isolation stage (MinusK 150BM-8). We use 2 mW from ECDL and send it via a fiber EOM (Jenoptik PM-705) to the cavity breadboard. Prior to the fiber EOM the light passes through an AOM (GH 3080-125) for potential power stabilization of the cavity input beam. The fiber EOM creates a sideband at a variable frequency up to 1.5 GHz (Rigol DSG836 frequency generator).

The sideband frequency is adjusted such that simultaneously the sideband is resonant with the arbitrarily positioned cavity resonance and the ECDL output is resonant with the atoms. On the cavity breadboard, the locking beam passes through a telescope for mode matching with the cavity TEM_{00}-mode and another EOM (Qubig PM7-NIR 25) to create 25 MHz sidebands for the PDH locking method. The PDH error signal is generated from the cavity reflection signal (Thorlabs PDA10A-EC) with the PDH module in the DLC. The error signal is processed by a TOPTICA Falc lock box and fed back to the laser current via a fast locking branch and the piezo set voltage via the utility inputs on the DLC pro.

Once the laser frequency is stabilized to the cavity, it would be advantageous to obtain a quantitative measure of the resulting laser linewidth. However, without a homodyne or heterodyne measurement, we only optimized the lock based on a spectral analysis of the error signal. As presented in figure 2.16, we adapted the feedback system to have the smallest servo bumps. Furthermore, we maximized the feedback bandwidth by pushing the servo bumps to higher frequencies. In the end, the laser frequency stability was found to be sufficient for our purposes, such as creating a MOT and performing spectroscopy scans on the narrow 7.4 kHz transition.

Since the cavity length and resonance position are only passively stabilized by keeping the temperature at the zero crossing of the Zerodur spacer, the accuracy of our frequency stabilization relies on a continuous comparison of the laser frequency to the atomic resonance. This is done by a daily check of the red MOT performance and potential adjustment of the AOM frequency. A tracking of the frequency adjustments revealed that the cavity resonance has a drift of 10 kHz per day.

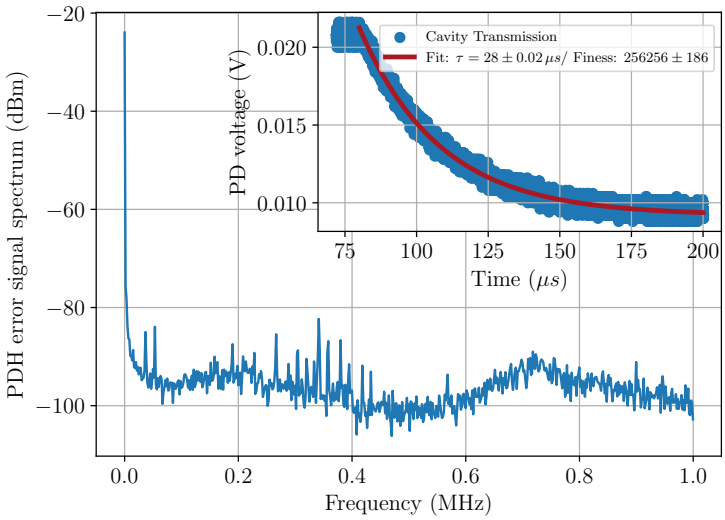

FIGURE 2.16: Characterization of 689 nm laser frequency lock. The figure shows the spectrum of the PDH error signal. The spectrum is used to optimize the lock settings for small servo bumps at maximal frequency position. The typical servo bump around 750 kHz is shown. The inset shows a fit of a cavity-ring down measurement of the high finess cavity giving a cavity linewidth of 5.85 kHz.

OSG laser frequency stabilization

The red laser system is connected to the OSG laser system with an offset lock. The OSG laser system is a Toptica DL pro as illustrated in figure 2.15. Since we want to create state-dependent potentials with the OSG beam, the frequency has to be close to the $^3P_1$

transition. Therefore, we use a variable offset lock with the red laser system to have the flexibility to choose the OSG detuning within the excited state manifold of the $^3P_1$ state.

The lock method requires a beat note by interfering the red MOT laser with the OSG laser on a fast photodiode (Hamamatsu G4176 directly mounted on a minicircuits bias tee ZFBT-4R2G+). The beat frequency is mixed with a variable frequency generator (Windfreak Synth USBII) to give a remaining 80 MHz beat that can be down-converted with another frequency source (Rigol DG4102) inside a mFALC module to directly generate an error signal. The error signal is again fed back via the mFALC to the current and piezo of the OSG laser and optimized to transfer the linewidth of the red laser onto the OSG laser.

The remainder of the OSG laser system deals with high-resolution switching of the beam. Since the OSG beam will create the OSG potential for the atoms, a high temporal power stability and precise timing are necessary for a consistent application in the spin separation sequence. Therefore, the Wieserlabs DDS is the RF signal source used to switch the OSG beam in sync with the tweezer beam with high timing resolution. A RedPitaya is used to stabilize the power of the OSG beam after the fiber by acting on a VCA (minicircuits ZX73-2500+) and measuring the power on the experimental table (Thorlab PDA8A2). With the RedPitaya program Pyrpl [82], the power is stabilized in a Sample and Hold fashion with active stabilization behind a shutter and release of stabilization during the light pulses. The typically 5 μs long pulses are stabilized to 2.5 mW with a stability of $I_{SD}/I = 3.3\,\%$ that we measure with an out-of-loop photodetector over a time span of 1 hour.

Another feature of the OSG beam path is the extended beam path after the AOM. Although the self-built shutters have switching times of 10 ms, we were concerned that light from the zero-order beam of the AOM makes it into the fiber and creates unwanted background illumination. This light can result from internal reflections or scattering within the AOM crystal. With the extra beam path, this leakage light is suppressed.

2.4.3 Repump lasers

The repump laser system involves two Toptica DLC pro lasers and a wavemeter lock as presented in figure 2.14. The setup consists of initial beam shaping with an anamorphic prism pair, switching with an AOM (GH 3080-125) that is controlled by a home-built AOM driver and delivered to the experiment table via fibers. The zero-order of the AOM is transported to a wavemeter setup for locking the repump frequency. The repumping on the 707 nm transition in ^{87}Sr requires a frequency modulation over a span of 2 GHz. To achieve that, the piezo voltage is modulated with a 500 Hz Sine signal. Furthermore, the 707 nm laser system requires a shutter during the blue MOT and reservoir state loading as the 707 nm light depumps the atoms from the $^3P_2$ state.

For the wavemeter lock, we use a RedPitaya controlled by a PC program. The program retrieves the current frequency from the wavemeter. Subsequently, the RedPitaya adjusts the externally controlled piezo voltages of the laser via the DLC pro. The lock does not require a full PID logic but rather simply adjusts the piezo voltage based on the piezo frequency-voltage calibration. With that, the lasers are stabilized with a 20 MHz resolution given by the resolution of the wavemeter (High Finesse WS6-200). Additionally, the locking process alternates between the 707 nm and 679 nm repumper by activating shutters in the wavemeter setup.

2.4.4 Dipole trap lasers

For the dipole trap laser, we use a cost-efficient diode laser seed and fiber amplifier architecture at 1040 nm. The seed laser is a self-built diode laser with a cat-eye design. The laser

system has been built by our master student Etienne Cardi and presented in figure 2.14. The manufacturing is inspired by a design from [83] that uses a laser diode (Sacher laser SAL-140-160) with 50 mW output. Current, temperature, and piezo voltage are controlled by Thorlabs Benchtop laser controllers (TED200C, LDC205, MDT693B). To isolate the seed laser from environmental noise, the laser is built on a vibration-isolated breadboard. The laser achieves a mode-hop free tuning range of 2 GHz. The single-mode operation is continuously monitored on a self-built FPI setup (Thorlabs E03 mirrors). For that, we use a scan signal from a RedPitaya via the Piezo voltage amplifier and the readout of the cavity transmission on a photo diode (Thorlabs PDA 110). Via a PM fiber, we send 30 mW to a 50 W fiber amplifier (ALS 1040).

The second dipole trap laser system is the tweezer laser system at 813 nm. It follows the same architecture idea consisting of a self-built seed diode laser and an amplifier, as shown in figure 2.14. The laser system has been built by my colleague Leon Schaefer. The seed laser is again a cat-eye laser (Thorlabs diode L820P100) generating 38 mW of seed light for a self-built TA system. The TA (Toptica TA-0808-3000-3) amplifies the seed light to typically 500 mW at 1.4 A. The seed laser is driven by a Koheron (Koheron DRV200-A-200) current driver and temperature stabilized by a Meerstetter (Meerstetter TEC-1161-4A-NTC) controller. The dual controller also stabilizes the temperature of the TA. The TA current up to 2 A is provided by a Thorlabs LDC204C. The TA chip is embedded in a cage system with aspheric lenses (Thorlabs A230TM-B). After the TA and diffraction from a 80 MHz AOM (GH 3080-125), the light is coupled to a fiber for delivery to the atoms. We typically use 150 mW at the fiber output for the experiments presented in this thesis.

Temporal control of the tweezer power is essential in our experimental sequence. Therefore, we synchronize the AOM control of the tweezer and OSG beam with the Wieserlabs DDS. Controlling the tweezer trap depth is done with a VCA (Minicircuits ZX73-2500M-S+). Additionally, we power stabilize the tweezer beam with another independent VCA circuit, which is controlled by a RedPitaya. We do a sample and hold procedure to avoid power stabilization during power ramps. With an out-of-loop photodetector, we measure a power stability of $I_{SD}/I = 2.1\,\%$ over a time span of 1 hour.

2.5 Optical systems for the experiment

2.5.1 Atomic beam setup

The cooling procedure starts with creating an atomic beam out of the AOsense oven system towards the glass cell. The associated optical cooling setup is mounted on the translation stage surrounding the AOsense system. The beams possess the beam profile, power, and polarization specified by the AOsense system. The optical system is illustrated in figure 2.17. Additionally, a differential absorption measurement is employed within the vacuum chamber to determine the atomic flux.

The Zeeman slower beam requires a beam diameter of approximately 5 mm, a typical power of 100 mW, and left circular polarization. Unfortunately, we could never measure an increase of flux with an activated Zeeman slower beam. As will be explained in the next chapter, the Zeeman slower beam is converted into the mini Zeeman slower beam in the blue 3D MOT setup.

Apart from the Zeeman slower beam, the AOSense beam source requires two 2D MOT beams. The two beams have a common fiber port source and are split and power balanced using a PBS. Afterward, the beams are shaped into 5×20 mm beams. Prior to beam shaping, a pair of quarter-wave and half-wave plates is used to set the polarization before the vacuum windows with a polarimeter. The beams are coupled to the in-vacuum optics and retro-reflected with a pair of kinetic mirror mounts in a periscope arrangement. We

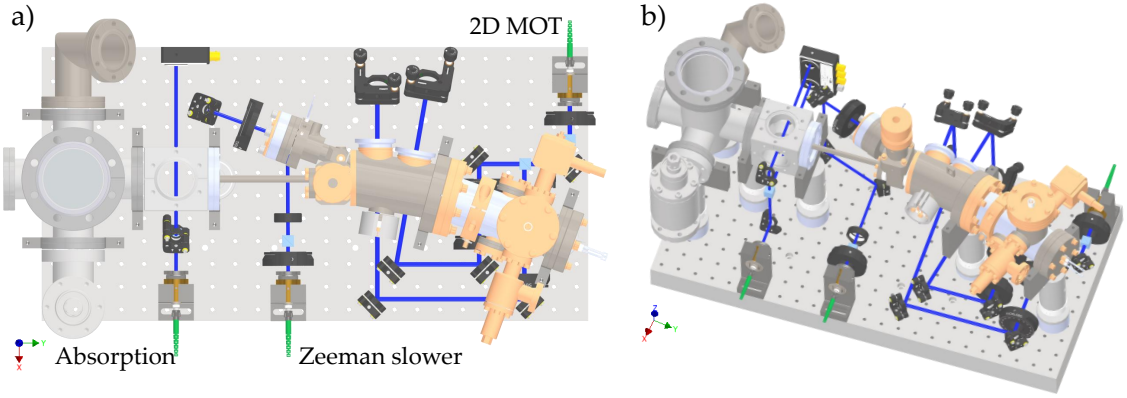

FIGURE 2.17: Optical system for the atomic beam source. The optical system creates two 2D MOT beams with a beam shape of 5 mm×20 mm and a Zeeman slower beam with 5 mm beam diameter. Additionally, a differential absorption measurement setup measures the atomic flux in the vacuum cube after the AOSense output.

initially optimized the alignment, power balancing and polarization with the output flux signal. Later, we optimized the beam power distribution towards the 3D and 2D MOT beams by looking at the 3D MOT atom signal. Typically, we have a beam power of 22 mW for the first beam and 18 mW for the second beam with a detuning of $0.5\,\Gamma_{461}$. The absorption measurement setup in the vacuum cube measures the atomic flux by measuring the power difference of a 1 mm beam going through the atomic beam and a twin beam passing under the vacuum cube on a balanced photodiode (Thorlabs PDB210A).

2.5.2 MOT system

After the atomic beam reaches the glass cell, the atoms are captured and cooled using a two-stage Magneto-Optical Trap (MOT) setup. Figure 2.18 shows a CAD illustration of the complete optical setup. The optical setup includes the blue MOT (bMOT) system, a mini Zeeman slower beam, repumper beams and the red MOT (rMOT) system. A fluorescence imaging system aligned along the main coil axis captures images of both MOTs.

Blue MOT beams

The full optical system is mounted on breadboards with three different levels. The lowest level consists of the optical table. The largest access to the atoms is provided by the horizontal atom plane, which features a custom breadboard equipped with miniaturized opto-mechanical components. Another custom breadboard represents the top level. The top breadboard has a center hole for a potential top microscope setup and a square hole on the side that allows for shining MOT beams onto the atoms. It is made of fiber-enforced material to avoid the formation of eddy currents when switching the magnetic fields. From the top breadboard, the blue and red MOT beams are directed toward the atoms at an angle of 50° with respect to the vertical axis. The blue and red MOT beams are implemented as separate systems to avoid the use of costly bichromatic optics and to enable independent alignment and positioning.

In the blue MOT setup, each beam is first polarization cleaned after the fiber outcoupler and then beam shaped into a 1 cm diameter beam with a telescope. The beam size results from a design constraint of clipping the beams at the microscope. All three beams have an equal power of typically 10 mW. The blue MOT is typically operated at a detuning of

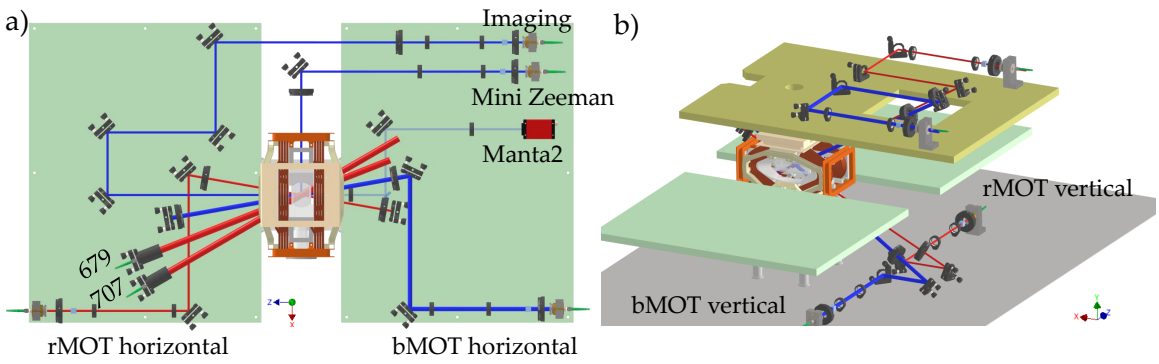

FIGURE 2.18: MOT setup including blue, red and repumper beams as well as a fluorescence imaging setup. a) The horizontal MOT beams (green breadboard) are polarization cleaned and beam shaped to a beam size of 1 cm diameter for the blue MOT beams and 7 mm for the red MOT beams. The single-pass repump beams have a beam size of 8 mm. The fluorescence imaging system is a 4f system with a magnification of $M = 1$. b) The vertical MOT beams are guided through the glass cell center with angled mirror mounts from the top breadboard (olive) and the table breadboard (gray).

$1.5\,\Gamma_{461}$ and a field gradient of 45 G/cm along the strong coil axis. The MOT beams are guided through the glass cell center using a pair of kinetic mirrors and retroreflected by a single kinetic mirror. The last optical element before the glass cell is the quarter-wave plate to set a circular polarization. To set up the MOT beams, we first used the retractable vacuum system and overlapped all MOT beams at the center of the coils, without the glass cell in place. The polarization is set at the position of the atoms with a polarimeter. The large angle of incidence of the MOT beams on the uncoated glass cell results in pronounced interference fringes. These fringes are highly sensitive to beam position and affect the shape and signal strength of the blue MOT. Alignment optimization is performed using real-time imaging of the blue MOT fluorescence.

Additionally, the blue MOT system consists of the mini Zeeman slower beam along the short axis of the glass cell, counter propagating the atomic beam. The beam has a diameter of 5 mm and a power of 1 mW. The beam parameters were found by experimental exploration and simulation as presented in section 3.2.1.

Red MOT beams

The red MOT beams are similarly constructed as the blue MOT beams but have a smaller diameter of 7 mm. The three beams have equal powers of maximally 3 mW. In contrast to the blue MOT beams, the red MOT beams must be aligned with higher precision by taking images after the full red MOT sequence.

Repumper beams

For seeing the live blue MOT, the two repumper beams are necessary. The repumper beams in the MOT setup are single-pass beams, each with a diameter of 8 mm, and maximum power of 8 mW at 679 nm and 10 mW at 707 nm.

Low-NA imaging

We have a low-NA fluorescence imaging system (referred to as the Manta2 imaging system) along the main coil axis. A multi-coated lens (Thorlabs LA4380-YAG-ML) collects

the fluorescence light. The imaging light is reflected from a dichroic mirror (Thorlabs DMLP490). Finally, a mirror and a focusing lens (Thorlabs LA1509-A) image the light onto a CCD camera (AlliedVision Manta G-201B-30) with a magnification of $M = 1$.

In addition to fluorescence imaging, the Manta2 imaging system takes absorption images with an absorption beam coming from the other side of the glass cell, as shown in figure 2.19. The absorption beam has a beam diameter of 2 mm and is referenced to the atom position and retro-reflected from the glass cell. The absorption imaging beam is coupled to the reservoir dipole trap setup as explained in the next section.

2.5.3 Reservoir dipole trap

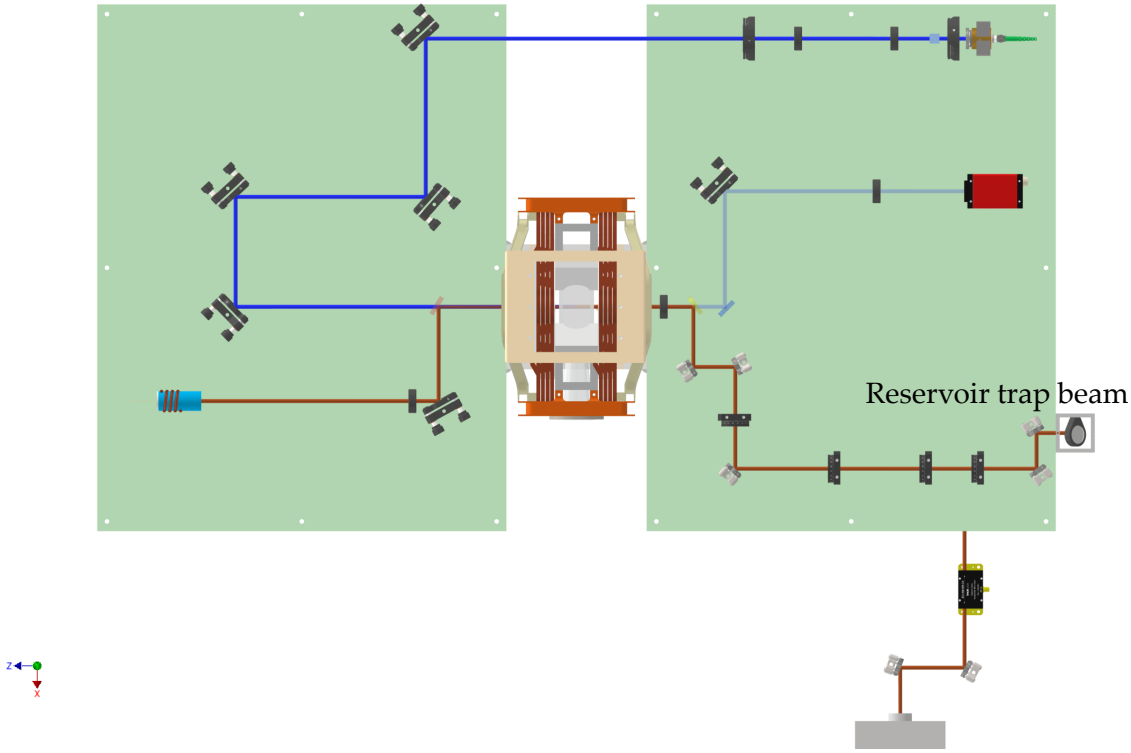

FIGURE 2.19: Optical setup of the reservoir dipole trap. The beam is guided from the fiber amplifier output on the optical table via a periscope to the horizontal breadboard at the atomic height. The reservoir beam is overlapped with the absorption beam for prealignment. For beam characterization the vacuum system is retracted and a camera at the atom position measures the beam shape.

The following section describes the 1040 nm reservoir dipole trap used to transfer atoms from the red MOT into a conservative dipole trap.

To achieve an efficient transfer into the reservoir trap, the trap geometry must be matched to the size and temperature of the final cold red MOT. The red MOT typically has a size of $400 - 600\,\mu$m along the x-axis and about $50\,\mu$m along the y-axis. Accordingly, the reservoir trap dimensions are chosen to be $w_x = 260\,\mu$m and $w_y = 20\,\mu$m, providing enough confinement in the vertical direction. Using the equation from Appendix B to calculate the light shift, we find that the chosen trap geometry yields a trap depth of approximately $19.5\,\mu$K at a beam power of 4 W. The resulting trap depth is sufficiently deep to capture a significant fraction of the red MOT even when the red MOT's temperature is

more than an order of magnitude larger than its Doppler temperature limit. The resulting trapping frequencies are $\omega_x/2\pi = 52\,\text{Hz}$, $\omega_y/2\pi = 686\,\text{Hz}$ and $\omega_z/2\pi = 8\,\text{Hz}$.

To deliver the necessary power to the reservoir dipole trap, a free-space beam setup guides the output of the fiber amplifier directly to the atoms. By utilizing the good beam quality of the fiber amplifier outcoupler (specified with $M^2 = 1.1$), the setup avoids power losses and thermalization process of a beam delivery through a costly high-power fiber. As shown in figure 2.19, the output beam is first sent through an AOM (GH 3110-197) which is controlled by a home-built AOM driver and then guided through a periscope to the first-level breadboard. The 1 mm diameter beam is shaped with two consecutive telescopes in cage systems. A kinetic mirror mount is used to center the beam on the cage system. Furthermore, the cylindrical lenses are made of UV fused-silica to reduce thermal lensing and are mounted in rotational mounts.

With a retracted vacuum system, we prealigned the reservoir trap beam and measured the beam quality and shape at the position of the atoms. For a more precise alignment of the reservoir beam to the atoms in the red MOT, the reservoir beam is overlapped with the absorption beam. The two beams are overlapped using a dichroic mirror (Layertec 160937). The perpendicular alignment of the absorption beam to the glass cell assures minimal aberrations from the glass wall for the focusing of the reservoir beam. After the glass cell, the reservoir beam is separated from the absorption beam with a hot mirror (Thorlabs M254H45) and guided to a water-cooled beam dump.

2.5.4 Microscope setup

The microscope setup consists of several sub-systems, which are necessary to trap, image, and manipulate single atoms. The central object is the microscope objective that focuses the potential beams down to micrometer scale and is used to collect the fluorescence on an EMCCD camera for imaging. The following sections describe the layout and alignment of the optical systems that make the spin-resolved imaging of single strontium atoms possible. These systems include the single tweezer beam, the fluorescence imaging path, free-space imaging beams, a cooling beam, and the OSG beam.

Tweezer beam setup

For creating a single tweezer trap, a custom-made high-NA objective focuses a 813 nm collimated beam down to a micrometer-scale beam into the glass cell from below. The microscope objective has been designed and manufactured by Special Optics. It has a NA of 0.55 and an air-spaced lens design. Its working distance is designed for 1 mm of air, 5 mm of fused-silica glass cell wall (SK 1300), and 12 mm of vacuum inside the glass cell. The housing is made of non-magnetic material (Ultem 2300). Collimated beams at 520 nm and 813 nm with beam diameters of 17.2 mm at the objective entrance will give diffraction-limited spots in the focal plane corresponding to a NA of 0.55. The effective focal length is 18 mm. In order to image atoms in the focal plane of the objective with 461 nm light, the light at 461 nm is diverging at the objective output with a half-angle of 0.163 deg. The AR coating has been designed to minimize losses at 461 nm, 520 nm, 689 nm, 813 nm and 1064 nm, however, test measurements revealed that the transmission for 461 nm is only 50 %. The objective is mounted on a 5-axis aligner (Newport 9081), allowing precise adjustments of position and angle. The upright assembly provides all necessary degrees of freedom to align the objective perpendicularly to the glass cell and to set the working distance accurately at 1 mm. The objective itself is mounted in a piezo translation stage (PI Pifoc P-725.4CDE2) to set the focal position with 10 nm resolution.

The tweezer beam is created with a setup on the first-level breadboard as shown in figure 2.20 a). The tweezer beam shaping starts with a collimated beam out of a standard fiber outcoupler (Thorlabs SM1ZA assembly). Afterward, two PBS clean the polarization. The reflection of the second PBS is the pick up for the power stabilization as presented in section 2.4. With a cleaned polarization, a pair of quarter-wave and half-wave plates is used to tune the polarization. The polarization has been tested at the position of the atoms with a polarimeter and set in the z-direction along the direction of the cooling beam. A 10:1 telescope increases the beam size to 19 mm diameter before the beam is reflected on a dichroic mirror towards the objective. A pair of mirrors aligns the beam straight on each telescope lens in order to minimize aberrations in the beam. We checked the beam quality before the objective by focusing down with a $f = 50$ mm test lens (Thorlabs AC254-050-B) and analyzing the focus quality with a camera. We had to place the final lens in a kinetic mount to reduce the aberrations. We also found that dichroic mirrors are a common source of aberrations. Reflecting a beam from a dichroic beam with a large number of dielectric layers causes wavefront distortions [84]. This led us to replace the initial dichroic mirror (Semrock SEM-FF749-SDi01-25x36x0.3) with a Thorlabs BB1-EO3 backside polished mirror. Under a shallow angle of $8\,^{\circ}$ we measured a reasonable transmission for 461 nm and proved its suitability for the subsequent imaging system.

The final alignment step of the tweezer setup is the coupling of the tweezer beam into the objective. For incoupling, we cropped the large tweezer beam and overlapped it with an alignment beam coming out of the objective, as presented in the next section. The final alignment optimization is done with the atoms as reference and presented in chapter 4.

High-NA imaging

The objective is simultaneously part of two fluorescence imaging systems for separately imaging the tweezer loading in the red MOT and individual atoms on an EMCCD camera. Following the dichroic mirror, a flip mirror directs the image light either to a second CCD camera (AlliedVision Manta G-201B-30) or allows transmission towards an EMCCD camera (Andor EMCCD 987). The focusing lens (Thorlabs LA1417-A) in the Manta1 imaging system creates an image with a magnification of $M = 7.64$. With the Manta1 imaging system, we have a second view of the red MOT from below. On the other side, the single-atom imaging beam path uses a minimal amount of optical elements and a 2" achromat lens (Thorlabs LA1727-A) to create an image with a magnification of $M = 47.64$. A final kinetic mirror conveniently moves the image on the Andor camera. The Andor camera is typically cooled to $-80\,^{\circ}$C and is therefore water cooled with a dedicated chiller (Neslab RTE-111). Furthermore, the camera assembly is wrapped in black aluminum foil to minimize stray light from laboratory lighting and blue light from the locking setup, which significantly contribute to background noise. Additionally, a mechanical shutter in the imaging beam path needs to be triggered when taking a picture in order to prevent blue light from the blue MOT beams from flashing the EMCCD.

The precise alignment of the microscope objective required several steps. Crucial for the alignment of the objective and imaging system was a 461 nm alignment beam referenced to the red MOT position from the top-level breadboard. The associated optical setup is presented in figure 2.20 c). The blue light comes from a temporary pickup of the imaging beam and is transported to the top-level breadboard with a fiber. The alignment beam is focused such that its focal point coincides with the atom position at the center of the glass cell. The beam path is referenced to the final red MOT position by shooting out atoms with a 5 ms imaging pulse before imaging the remaining red MOT with the Manta2 imaging system. To fix the angle, the beam is set perpendicular to the glass cell by

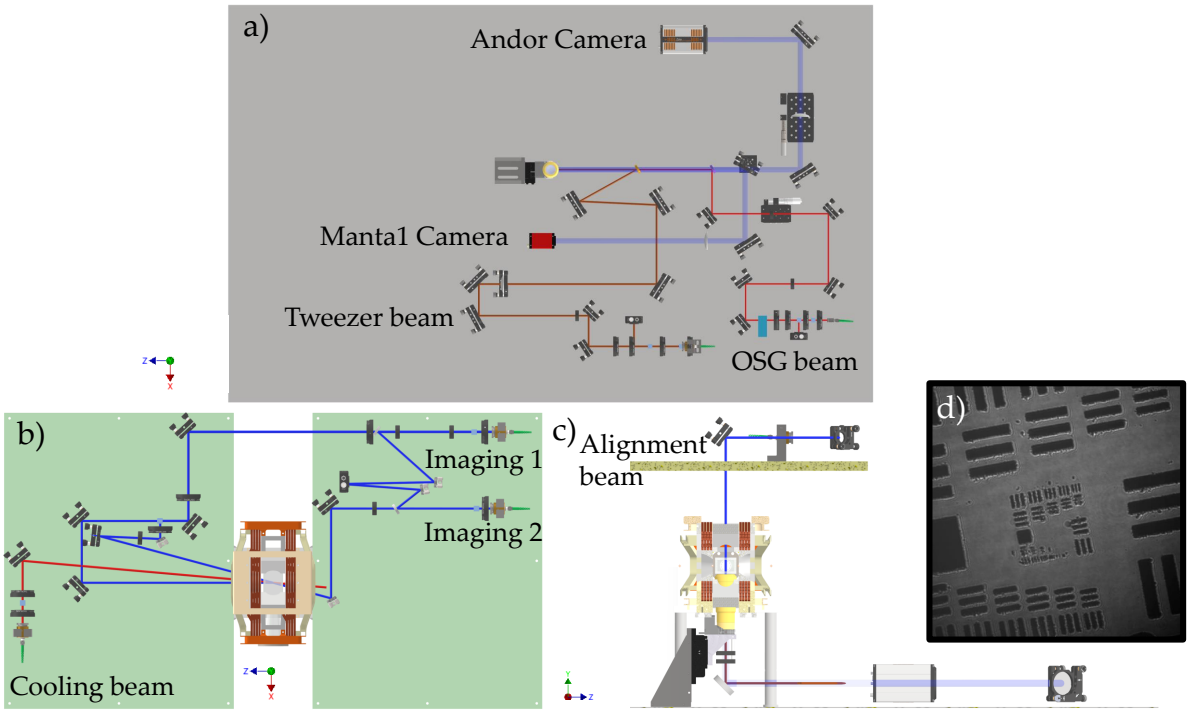

FIGURE 2.20: Gallery of the tweezer setup and OSG setup. a) The table breadboard hosts the tweezer beam setup, the Manta1 imaging system, the single-atom imaging system with the Andor camera and the OSG beam setup. b) On the first level breadboard are the absorption beam used as a single atom imaging beam, two counter propagating beams for the free-space imaging and a red cooling beam. c) Frontal view of the alignment beam from the top bread board setting the alignment of the objective and subsequent imaging optics. The alignment beam illuminates a target at the atom position in order to prealign the imaging system. d) An image of the target on the prealigned Andor imaging system.

overlapping the retro-reflection from the glass cell. Then, the objective is positioned centered to the incoming alignment beam. The angle of the objective is aligned such that the multiple reflections from the internal optics are overlapped with the incoming alignment beam. At the same time, the alignment of the objective has to ensure a centered output of the alignment beam. This procedure fixes all transversal and angle degrees of freedom. The remaining freedom is the distance to the glass cell bottom, which needs to be 1 mm. This distance is set by taking pictures from the side and referencing the gap to the 5 mm glass wall thickness. Thanks to the focus of the alignment beam at the glass cell center, the alignment beam leaves the objective input fairly collimated. This output beam is used to assemble the imaging system by centering the imaging lenses and mirrors on it and directing the alignment beam to the Manta1 and Andor Camera.

The objective distance is further optimized by creating a sharp image of a test target (Thorlabs R1DS1P1) in the alignment beam at the atom position. To place the target at the atom position, we retracted the glass cell. To mimic the imaging plane of the atoms, the target is positioned at the height of the cooling and imaging beam and aligned perpendicular to the alignment beam by overlapping the retro-reflection from the target's glass plate. Additionally, we placed a 5 mm glass plate (Laser optics S-00925) 12 mm underneath the target to mimic the influence of the glass cell bottom wall on the imaging quality. In the end, the prealigned imaging system creates a sharp image of the smallest structures with a 1 μm stripe gap on the Andor camera as presented in figure 2.20 c).

Single-atom imaging beams

In the single-atom imaging process, we use a single-pass 461 nm imaging beam and a 689 nm single-pass cooling beam. The two beams are located on the second level breadboard as shown in figure 2.20 b). The beam sizes are reasonably large to homogeneously illuminate the tweezer trap.

For the blue beam, we use the absorption beam and strongly reduce the power during the imaging. The blue imaging beam has a horizontal polarization to maximize the dipole radiation characteristic towards the objective.

In contrast to the blue imaging beam, the cooling beam is angled with $5\,^{\circ}$ to the glass cell wall to avoid the formation of a standing wave of cooling light from counter-propagating glass cell reflections. The red cooling beam diameter is 0.5 mm and its intensity can reach up to $250\,\mathrm{I}_{sat}$. The polarization is circular to facilitate optical pumping within the ground-state nuclear spin manifold of ^{87}Sr atoms. The initial alignment of the cooling beam is done in the same way as the absorption beam. The alignment optimization to the tweezer trap is optimized by kicking out atoms from the tweezer trap on resonance.

Free-space imaging beams

Associated with the spin-resolved imaging procedure is an imaging in free space. For the free-space imaging, we use two additional fluorescence imaging beams. On one side, the imaging beam is derived from the absorption beam and sent towards the tweezer trap under an angle of $15\,^{\circ}$. Again, the angle of incidence avoids a lattice formation of imaging light. On the other side, the counter propagating beam is delivered to the breadboard from the 2D MOT AOM setup. Free-space imaging requires a large light intensity. Therefore, both imaging beams are focused. The first beam is focused to 300 μm beam diameter, and the second beam is focused to 1 mm beam diameter. The power in both beams is increased for the free-space imaging such that both beams have at least a peak intensity of $20\,\mathrm{I}_{sat_{461}}$. Both beams require a clean polarization in the horizontal direction. Furthermore, a small pick-up fraction of both beams is combined on a PD for monitoring the imaging pulses. The initial alignment of both beams is similar to the absorption imaging beam. An alignment optimization and intensity balancing is done by imaging atoms in the tweezer and presented in chapter 5.

2.5.5 OSG beam setup

The last optical setup for performing spin-resolved microscopy of single strontium atoms is the OSG beam. Similarly to the tweezer beam, the single OSG beam enters the microscope objective via a dichroic mirror (Laser optics L-07090) and is aligned next to the tweezer trap. The OSG beam setup is illustrated in figure 2.20 a). The OSG beam is a collimated beam from a fiber coupler (SK 60FC-4-M4-10) with a beam diameter of 2 mm. The polarization is cleaned with a pair of cubes. The second cube reflection is the pickup for the power stabilization. For the employed sample-and-hold method, the beam is power-stabilized behind a home-built shutter box. After the cleaning cubes, a pair of half-wave and quarter-wave plates sets the polarization to linear polarization in the z-direction. Before a pair of kinetic mirrors couples the beam into the objective, a 1:1 telescope is used to change the position of the focus on the atoms with a translation stage. An input beam diameter of 2 mm at the objective entrance gives an expected focus waist of 3.9 μm at the atom position. Translating the second lens also changes the beam waist in the focus. However, a precise positioning of the focus to the tweezer trap in order to obtain the cleanest

light potential is more important than obtaining a certain potential size. The initial alignment of the OSG beam is done by overlapping the beam with the tweezer beam. A more precise alignment with atoms in the red MOT and tweezer trap is presented in chapter 5.

Chapter 3

Production of cold strontium gases

In this chapter, we detail the performance of the various optical cooling methods for creating cold ^{88}Sr and ^{87}Sr gases. The chapter starts with a measurement of the atom flux out of the AOSense oven in section 3.1. In section 3.2, the created atomic beam is captured in a blue 3D MOT. Section 3.3 presents the subsequent transfer from the blue MOT to the red MOT, where the temperature of the atoms is further reduced. Section 3.4 describes the loading of the reservoir dipole trap from the red MOT.

3.1 Atomic beam

The cooling process begins with the AOsense atomic source, which is designed to produce an atomic beam with a flux of 1×10^{10} atoms/s at a typical oven temperature of 430 °C. After atoms leave the oven, a Zeeman slower beam slows the atoms in longitudinal direction. Afterward, two consecutive 2D MOT beams transversely cool the atomic beam and redirect it towards the differential pumping tube connected to the remaining vacuum system. We measure the atomic flux after the atom source with the differential absorption measurement setup (Setup 2.5.1) to verify the correct operation of the atom source and the creation of an atomic beam towards the glass cell.

On the one hand, the absorption measurement allows us to precisely set the polarization, detuning, and power balancing of the 2D MOT beams and the Zeeman slower beam to produce the strongest atomic beam. On the other hand, from the absorption strength, we can derive the atomic flux. Firstly, the measurement revealed a non-working Zeeman slower beam. Checking various beam polarization settings, detunings, and alignments at a maximal Zeeman beam power of 100 mW has never shown a measurable increase in atom flux. Since we did not want to break the vacuum and detach the AOSense source, we continued the experiment with the atom flux generated solely by the 2D MOT beams. For a total power of 40 mW in the 2D MOT beams, with 70 % of the power directed into the first 2D MOT beam, we observed a maximal absorption of 0.02 % at a detuning of roughly $-\Gamma_{461}$. The scan of the absorbed power fraction as a function of the 2D MOT beam detuning is shown in figure 3.1.

The maximally absorbed light fraction is translated into an atom column density in the atomic beam according to the Beer-Lambert law [85] with

$$ln\left(\frac{I_0}{I}\right) = n^{col}(x,y) \times \sigma \tag{3.1}$$

where σ is the scattering cross-section and I_0 the measured reference intensity. With an absorption beam, operating at a low intensity of $0.05\,\mathrm{I}_{sat}$ and at resonance, the scattering cross-section is given by $\sigma_0 = 3\lambda^2/2\pi$. The measured density in the atomic beam yields a density of $n = 1.97 \times 10^5\,\mathrm{atoms/cm^{-2}}$.

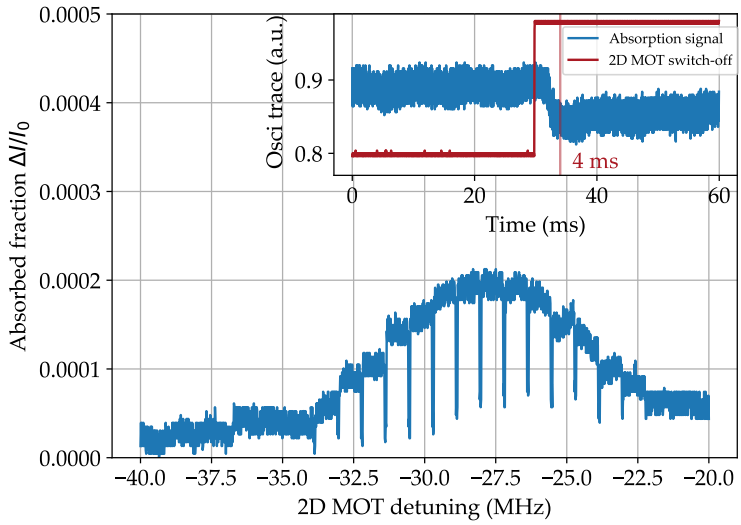

FIGURE 3.1: Absorption of the atomic beam in the vacuum cube. The absorbed power fraction is measured with a balanced photodiode (Setup 2.5.1) depending on the detuning of the 2D MOT beams to the blue cooling transition. Inset: Time trace of absorption signal with respect to a sudden switch off of 2D MOT beams and interruption of the atomic beam 20 cm prior the measurement position. The delay between absorption signal and no-absorption signal is used to estimate the atom velocity and atom flux.

In addition to the measured density, the atom velocity is required to translate the absorption measurement into an atom flux. The atom velocity is inferred from an estimation of the time delay between the switch off of 2D MOT beams and the vanishing of the absorption signal 20 cm downstream in the atomic beam. As presented in the inset of figure 3.1, a determined delay of 4 ms corresponds to an atom velocity of approximately 50 m/s, resulting in an estimated atom flux of 9.8×10^8 atoms/s. The measured atom flux is an order of magnitude lower than the expected flux, which is expected from a non-working Zeeman slower beam. Nevertheless, the atom flux shows a linear dependence on the 2D MOT beam power, providing a means to compensate for the absence of a Zeeman slower by increasing the power in the 2D MOT beams. Increasing the power can be achieved by amplifying the 2D MOT with an additional blue injection-locked amplifier.

All in all, the measurement verifies that an atomic beam with substantial flux is directed toward the glass cell, where it can be captured by the blue 3D MOT beams.

3.2 Blue MOT

A fraction of the created atomic beam is captured in the 3D magneto-optical trap (MOT), created with the setup 2.5.2 inside the glass cell. The first stage is the 3D blue MOT (bMOT), operating on the broad $^1P_1$ transition. The broad transition enables rapid deceleration and cooling of atoms, reducing their temperature quickly to the mK-range. It serves as an initial cooling stage before transferring atoms to the narrow-line red MOT (rMOT). Due to the decay channel from the $^1P_1$ state to the $^3P_2$ state (figure 2.1), the bMOT offers a robust sequential cooling procedure by accumulating atoms in the magnetically trapped $^3P_2$ state. This technique is referred to as reservoir state loading [86]. The reservoir state loading circumvents the atom number limitation of a saturated blue MOT and allows for a robust transfer of atoms to the subsequent rMOT.

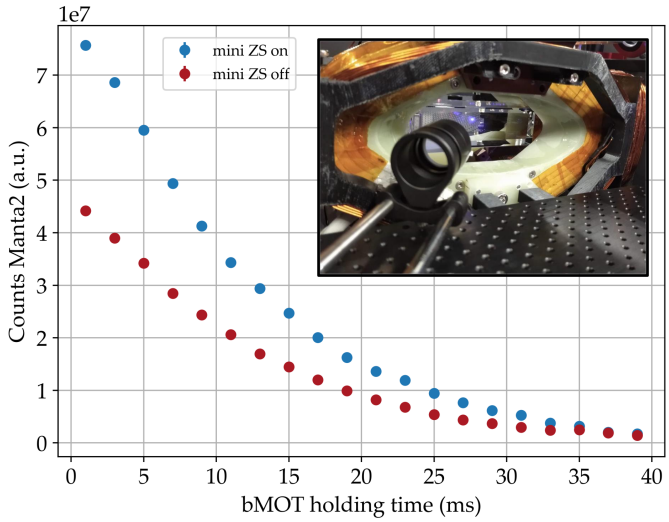

FIGURE 3.2: Positive effect of the mini ZS beam on the captured atom number in the bMOT. Fluorescence counts on the Manta2 camera as function of the blue MOT time for mini ZS on and off. The larger initial fluorescence stems from a better capture efficiency of atoms when the mini ZS is on. The inset shows a picture of the live repumped blue MOT in the center of the glass cell.

3.2.1 Mini Zeeman slower beam

The bMOT setup is aligned and optimized by continuously imaging the fluorescence of the bMOT on the Manta2 camera. All beams involving the initial atom capturing and blue cooling stage are set to yield the largest atom number in the continuous bMOT. A picture of the repumped bMOT is shown in the inset of figure 3.2. Although the initial 3D blue MOT setup successfully trapped atoms, we found by experimental exploration that the additional mini Zeeman slower (mini ZS) beam increases the number of atoms in the blue MOT. Since the beam has become a crucial part of stable MOT operation and has only been optimized in terms of alignment and beam power, we present in the following section an exploration of the MOT dynamics with the additional mini ZS beam.

Due to the diamond-shaped coils and resulting constraints on the MOT beam orientations, our MOT setup has a non-optimal beam configuration for a uniformly large capture efficiency. The MOT beams exhibit large angles of 50 ° against the y-direction. At the same time, the velocity capture range of arriving atoms is reduced by the 40 ° angle of the beams to the x-axis, which coincides with the magnetically weakest axis of the diamond coils. The counter-propagating mini ZS beam restores part of the reduced velocity capture range in the x-direction by providing a light pressure against the atomic beam propagation. The beneficial impact of the mini ZS beam is demonstrated by measurements of the bMOT lifetime (figure 3.2), which show that its application results in a 1.7-fold increase in the initial atom number.

To explore the optimization potential of the mini ZS beam, we perform 1D simulations of the light pressure of our MOT setup. The heuristic formula for the light pressure in a magnetic field gradient is given by the following expression [87]

$$f = \sum_i \frac{\hbar \vec{k}_i \Gamma}{2} \frac{s_i}{1 + s_i + 4(\Delta_i^2 - \vec{k}_i \cdot \vec{v} - \mu_B B' x)/\Gamma^2} \tag{3.2}$$

The expression takes each beam i into account, with the atomic decay rate $\Gamma = 2\pi \times 30.5\,\mathrm{MHz}$, the saturation parameter $s_i = I/I_{sat}$ with $I_{sat} = 40.76\,\mathrm{mW/cm^2}$, the detuning

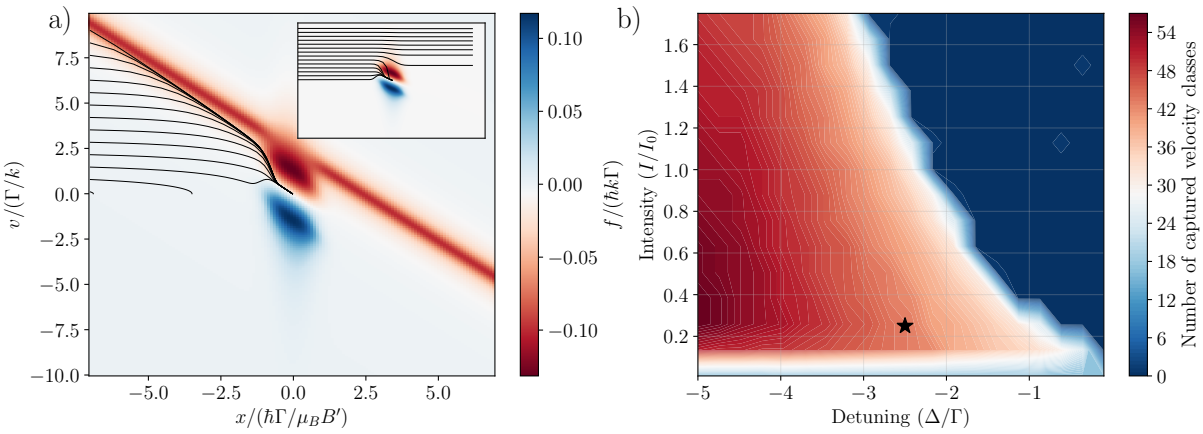

FIGURE 3.3: Simulation of the increased capture efficiency by calculating the light pressure of the bMOT with the additional mini ZS beam. a) The 1D light pressure profile along the x-axis is simulated in phase space with the current setting of the mini ZS beam and MOT beams. The black lines show trajectories of the atoms with different velocity classes in the MOT field towards the trap center. If reaching the trap center, the atoms can be considered to be trapped in the MOT. Inset: The same phase space analysis without the mini ZS beam, showing more velocity classes not being captured. b) Number of captured velocity classes out of 100 simulated velocity classes in a range of $v = 0.1\,\Gamma/k - 10\,\Gamma/k = 0.14 - 140\,\mathrm{m/s}$ as function of detuning and intensity of the mini ZS beam. For comparison the non-optimized current mini ZS beam setting is indicated with a black star.

Δ_i and the field gradient $B' = 22\,\mathrm{G/cm}$. The equation is included in the simulation tool PyLCP [88]. In the simulation tool, 2 counter-propagating MOT beams are defined with a k vector in the xy plane, a waist of 5 mm, and a mini ZS beam with a waist of 2.5 mm along the x-axis. For the MOT beams, we use a detuning of $\Delta = -\Gamma$ and an intensity of I_{sat}. The settings for our current mini ZS beam are $\Delta = -2.5\,\Gamma$ and $I = I_{sat}/4$.

We analyze the simulated light-pressure profile in 1D phase space along the direction of the incoming atomic beam. Additionally, we analyze the trajectories of various atom velocities arriving from the glass cell entrance. The majority of the velocity classes are slowed down along the counter-propagating mini ZS beam until the atoms reach the trap center, where the MOT beams are strong enough to confine them in 3D space. The simulations in figure 3.3 a) show that the deceleration from the current settings can even reverse the trajectories of the slowest atoms. In contrast, the inset in figure 3.3 a) shows the MOT dynamics without the mini ZS beam, where higher velocity classes are not captured by the MOT beams.

In order to find the optimal beam setting for future implementations in the experiment, we simulate 100 velocity classes in a range of $v = 0.1\,\Gamma/k - 10\,\Gamma/k = 0.14 - 140\,\mathrm{m/s}$ for variable intensities and detunings of the mini ZS beam and plot how many velocity classes are captured in the center area of $x = \pm 1\,(\hbar\Gamma/\mu_B B') = 1.48\,\mathrm{cm}$. The simulations in figure 3.3 b) indicate a potential increase of velocity capture range for larger detunings and higher intensities up to 0.75 I_{sat} when compared to our current setting (black star). On the other hand, for our available frequency setting, the simulations show that our beam intensity is just in the correct region, as too much power quickly becomes detrimental to the total MOT operation, which matches with experiences in the experiment.

3.2.2 Reservoir state loading

The reservoir state loading is essential to a robust operation of the experiment. It enables an enhanced transfer of pre-cooled atoms from the bMOT to be captured by the subsequent narrow red MOT [86]. The transfer from bMOT to rMOT is affected by the vastly different temperature difference of the Doppler temperature limit of 732 μK in the bMOT and the smaller recoil temperature limit of 230 nK in the rMOT. Furthermore, the initial bMOT is limited in density due to collision and light-assisted collisions, which limits the atom number in the subsequent cooling processes.

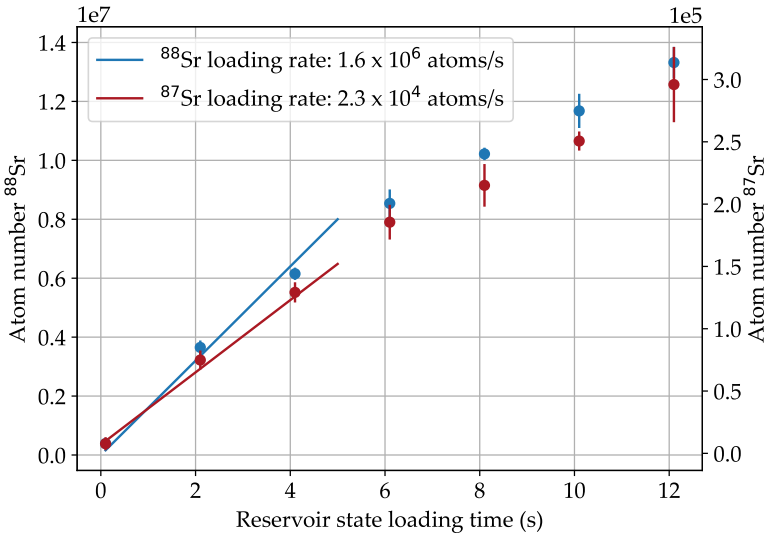

FIGURE 3.4: Loading curve of atoms from the reservoir state that are subsequently transferred and captured in the red MOT stage. A loading rate is fitted to the initial atom accumulation as a performance measure of the total blue cooling stage. The atom number is estimated from fluorescence images after repumping the atoms from the reservoir state and recapturing the atoms in the repumped blue MOT.

In the reservoir-state loading, the 2D MOT, 3D MOT, and mini ZS beams continuously operate as optimized before, atoms in the $^1P_1$ state decay via the $^1D_2$ state into the metastable $^3P_2$ state. As a consequence, the weak-field seeking m_F states of the $^3P_2$ state become trapped in the MOT gradient field, which creates a deep trap with up to mK depth, depending on the m_F state. Atoms can be accumulated in the trap over the timescale of the $^3P_2$ decay time of several seconds. Thus, it allows to accumulate more atoms than with a repumped bMOT. Furthermore, the reservoir-state loading allows us to compensate for a missing Zeeman slower, the significant differences in isotope abundances, and drifts in the blue MOT performance by extending the reservoir-state loading time.

In order to characterize the total blue cooling stage, we record a loading curve of the reservoir state. Currently, we don't have a protocol to measure the temperature or density of the blue MOT or the atoms coming out of the reservoir state with our absorption imaging setup. To quantify the reservoir state loading, we have to rely on the fluorescence signal from a subsequent recapturing in the repumped blue MOT. During the reservoir-state loading, we operate the coils at 142 A and thus have a gradient field of 45 G/cm in z-direction, 22 G/cm in x-direction and 43 G/cm in y-direction. For a conversion of fluorescence counts from the recaptured bMOT into an atom number, we can assume that we strongly saturate the blue transition at the intersection of the 3 MOT beams. Furthermore, we can assume to scatter blue photons at best with $\Gamma/2$ when shifting closer to resonance

for the imaging time. Figure 3.4 displays the loading curve, from which a loading rate of up to 1.6×10^6 atoms/s is derived for ^{88}Sr, and 2.9×10^4 atoms/s for ^{87}Sr.

The loading curves indicate a limit to the reservoir-state loading technique by showing an onset of saturation beyond 10 s of loading time. Furthermore, comparing the loading curve of ^{87}Sr and ^{88}Sr shows a considerably lower performance, even taking into account the lower abundance. The reason for that is the different magnetic moments of the Zeeman levels in the $^3P_2$ state and the resulting trapping forces in the magnetic gradient field. The $F = 5/2$ and $F = 7/2$ states exhibit the weakest trapping forces (see Appendix A). The states $F = 11/2$ and $F = 13/2$ are the most reliably trapped states in the magnetic gradient field. As a result, it is not worth it to repump the full $^3P_2$ state manifold but rather only address with the 707 nm repumper the transitions $F = 11/2 \rightarrow F' = 13/2$ and $F = 13/2 \rightarrow F' = 13/2$ transitions to get out of the reservoir state. A possible improvement for the ^{87}Sr reservoir state loading could be a drastically higher gradient field, such that all hyperfine states are trapped by adding another 200 A power supply in the MOT coil circuit.

After the reservoir-state loading, we hold the atoms for 100 ms while shuttering off all blue light that could be harmful during the repumping for the subsequent rMOT. After the holding, we repump the atoms with 707 nm and 679 nm light for 50 ms while the rMOT beams are already on and the MOT field is reduced accordingly. Once atoms are in the rMOT, the absorption imaging can be used to evaluate the red MOT performance more precisely, as described in the next section.

3.3 Red MOT

Following the initial cooling stage in the blue MOT, the subsequent red MOT operates on the $^1S_0 \rightarrow {}^3P_1$ transition, which has a linewidth of 7.4 kHz. The narrow laser cooling transition allows a further reduction in temperature with a recoil temperature limit of 230 nK and creates a cold and dense cloud of atoms that can be efficiently loaded into dipole traps. Due to its narrow linewidth, the red MOT operation requires a more precise tuning of the MOT beam alignment and a sequential reduction in temperature to effectively cool the atoms. This section presents the key aspects of the red MOT sequence employed to obtain robust and cold atomic clouds of ^{88}Sr and ^{87}Sr.

3.3.1 General red MOT sequence

The complete red MOT sequence has three distinct stages to achieve a transfer of the atoms from the reservoir state loading to the final, cold red MOT. The typical sequence is visualized in figure 3.5. The initial stage employs a broadband red MOT (BBrMOT) to match the spatial spread and velocity spread of atoms in the gradient field trap. During this stage, periodic frequency ramps generate additional frequency components, increasing the spatial capture volume and velocity acceptance of the red MOT light, enabling cooling of several velocity classes present at the end of the blue MOT. The laser frequency is swept over 2 MHz within a ramp time of 50 μs. For the same reason, the magnetic gradient field with respect to the weak x-axis is reduced from 22 G/cm to 1.5 G/cm to improve the capture efficiency. An image of atoms in the BBrMOT is shown in the collection of red MOT images in figure 3.6 a).

In the second stage, the frequency modulation span of the red MOT light is decreased to compress the atom cloud. This stage provides the best sensitivity for in-situ imaging, allowing precise adjustments of the beam alignment. Furthermore, the SFrMOT is sensitive to beam power balancing, where small imbalances change the shape and position.

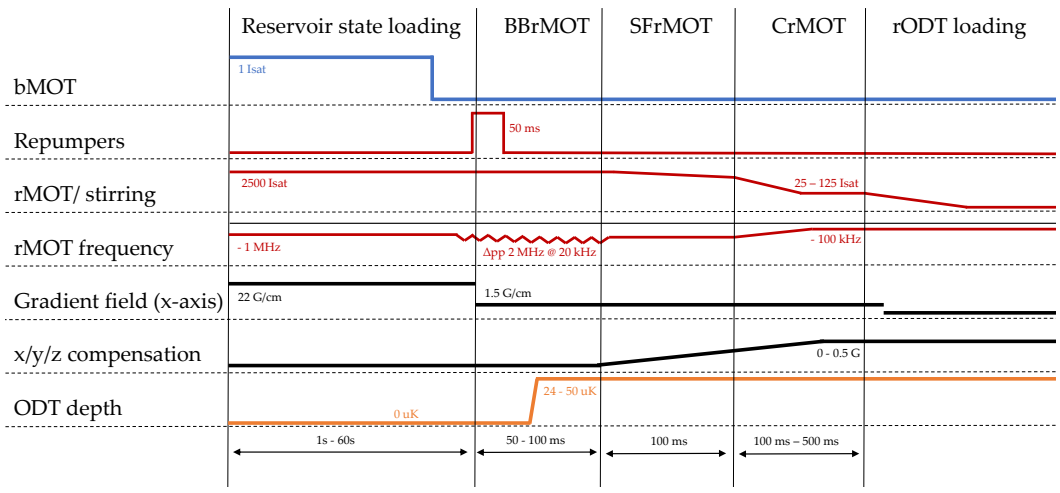

FIGURE 3.5: The typical experiment sequence of cooling down atoms in the blue MOT and accumulating in the reservoir state to the red MOT until the atoms are cold enough to be loaded in the reservoir dipole trap. The different stages of the red MOT are the broadband (BBrMOT), the single-frequency (SFrMOT), and the cold red MOT (CrMOT). The reservoir dipole trap is denoted with rODT.

The typical power ratio between the downward, upward, and horizontal beams is approximately 1.1 : 1.25 : 1, with most power in the downward-to-upward beam. The single frequency red MOT (SFrMOT) is shown in figure 3.6 b).

The final stage of the red MOT sequence ramps down the beam power to reduce the power broadening of the cooling transition and approaches the temperature limit of the cold red MOT (CrMOT). In this stage, the red MOT cloud gets cold and dense as shown in figure 3.6 c). As we ramp down the beam intensity to $I = 25\, I_{sat}$ over a time span of 100 ms, we also ramp the compensation fields. With the compensation field ramps, we can precisely align the CrMOT position for further loading into dipole traps.

At the end of the red MOT sequence, we perform TOF measurements to optimize the sequence parameters based on the final temperature and remaining atom number. For ^{88}Sr we obtain a red MOT cloud of up to 1.0×10^6 atoms and a temperature of around 1.2 μK. The cloud size is $w_x \times w_y = 550\,\mu m \times 200\,\mu m$. To achieve this, we have to load the reservoir state for 5 s. During the CrMOT phase, the atom-light interaction is minimal, causing atoms to fall through the laser beams, which constrains the cloud's lifetime to a few 100 ms depending on the final power of the MOT beams. The ^{88}Sr isotope is usually used to implement and maintain this red MOT sequence.

3.3.2 ^{87}Sr red MOT

The overall sequence structure remains the same for ^{87}Sr. However, the average rMOT trapping force is lower and requires additional techniques to create a stable ^{87}Sr red MOT. The reduced red MOT force is primarily due to competing trapping forces arising from the several Zeeman levels in the ground and excited state. Figure 3.7 illustrates the more complex red MOT operation with ^{87}Sr atoms. For comparison of the prototype MOT operation of ^{88}Sr, the three available Zeeman levels in the $^3P_1$ state are shown in green. The excitation can only happen with a MOT beam towards the trap center. In case of ^{87}Sr, the 12 Zeeman levels of the $^3P_1$ $F' = 11/2$ state unfold in the gradient field. The narrow linewidth resolves individual Zeeman states, leading to different trapping regions for the Zeeman levels. The Zeeman levels in the ground state have a negligible Zeeman shift.

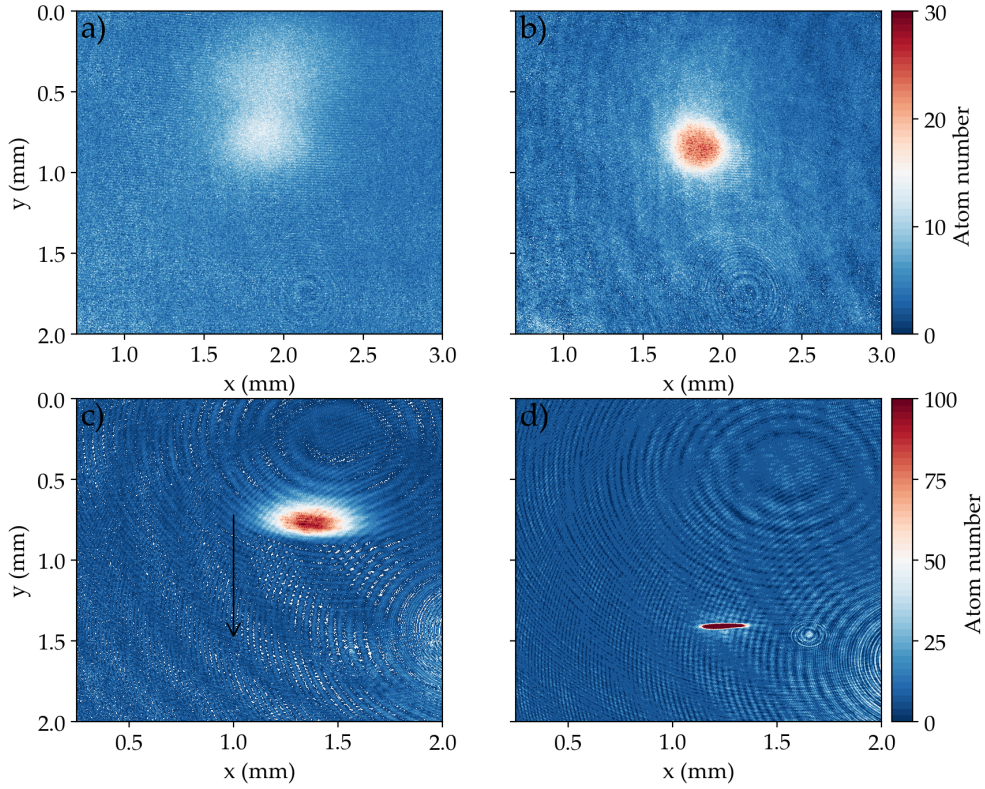

FIGURE 3.6: Absorption image collection of different red MOT stages with ^{88}Sr atoms. a) BBr-MOT b) Compression to the SFrMOT c) cold and dense CrMOT that is shifted downwards with compensation coils towards the position of the reservoir dipole or tweezer trap. c) Atoms in the reservoir dipole trap after the full loading sequence.

Consequently, a ground-state Zeeman level can be selectively excited and moved either towards or away from the trap center. This effect is most visible with the $m_F = 9/2$ ground state level in figure 3.7. This level can be either correctly excited to $m_{F'} = 11/2$ or pushed away from the center by a wrong excitation to $m_{F'} = 7/2$.

The additional stirring MOT beam driving the $F = 9/2 \rightarrow F' = 9/2$ transition partially restores the weak average MOT force. In the $F' = 9/2$ manifold, the Zeeman shift is 5 times smaller (see Appendix A), which moves wrong excitations away from the trap center. The stirring beam randomizes the spin state and keeps the average driving of all states higher than it would be without it [89]. The stirring beam is superimposed with the red MOT beams and similarly implemented in the sequence.

Another reason for a weaker average MOT force is the varying m_F-dependent transition strengths that are partially re-increased by ramping the detuning closer to resonance. The driving strength is given by the Clebsch-Gordon coefficient as calculated in Appendix B. The transition strength is maximal for ^{88}Sr. For ^{87}Sr, the transition strength reduces for smaller $|m_F|$ states. Averaged over all Zeeman levels, the transition strength is reduced. The resulting lower MOT trapping force is mitigated by reducing the detuning when the cold red MOT stage is approached.

Overall, the weaker MOT force is reflected in the lower density of the final red MOT cloud. We have to use a larger intensity of $I = 125\, I_{sat}$ in the beams to have a reasonable holding time of the red MOT, which increases our typical final temperature to $10 - 20\,\mu$K. Furthermore, the atom loss limits the final atom number to 1.0×10^5 atoms for up to 60 s of reservoir state loading. We have reached substantially lower temperatures down to $2\,\mu$K

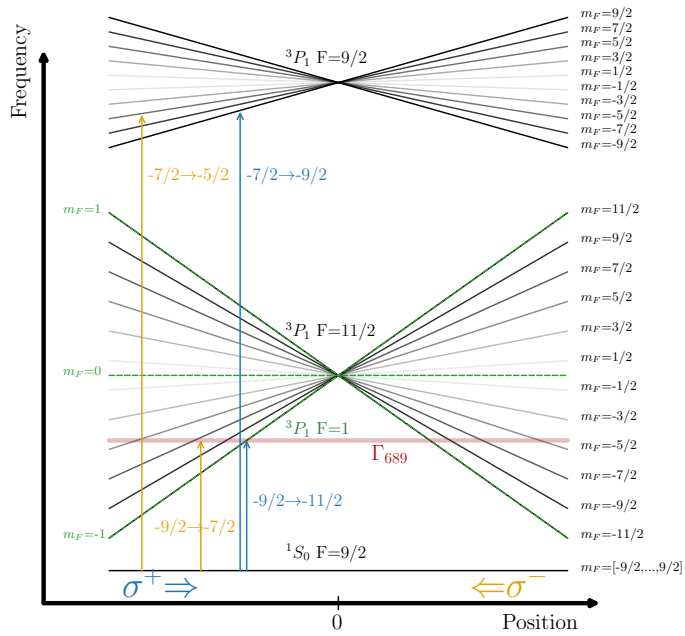

FIGURE 3.7: Working principle of the ^{87}Sr red MOT in 1D. The Zeeman shifts of the red MOT transitions in a 1D magnetic field gradient are plotted, showing detrimental excitations in the MOT operation. The antitrapping excitation is presented in orange pushing a ^{87}Sr atom exemplary in the starting level of $m_F = 9/2$ away from the trap. The correct excitation to $m_{F'} = 11/2$ in blue would push the atom back to the trap center. The MOT operation is boosted with a stirring beam to the $F' = 9/2$ manifold, in which the antitrapping MOT operation is further away from the trap center. The stirring light randomizes the spin state and provides a restoring force on average [89]. The gray scale represents the transition strength to each Zeeman level, indicating an averaged lower MOT force in comparison to ^{88}Sr, that operates solely on the simpler $^3P_1$ $F = 1$ transition as indicated in green.

by adding an extra MOT beam from below. This additional beam helped to hold the atoms against gravity, enabling a colder red MOT in the final stage. However, this temporary MOT beam had to be removed to make space for the microscope objective setup.

3.4 Reservoir dipole trap loading

The optical cooling sequence ends in loading the reservoir dipole trap, which increases the density and confines the atoms along gravity. Originally, the reservoir dipole trap was designed to facilitate the production of degenerate strontium gases. The geometry has been adapted from previous demonstrations of efficiently creating degenerate gases within an enlarged reservoir trap [38]. However, for the here presented work, the reservoir trap is aligned to the height of the tweezer trap and has two benefits for the subsequent tweezer setup. Firstly, it drastically increases the density and holding lifetime in comparison to the standalone red MOT. Consequently, it boosts the tweezer trap loading efficiency. Secondly, it provides a confinement in the imaging plane for the free-space imaging procedure. In the following section, we present the characterization of the reservoir dipole trap.

For the loading procedure, a final ramp down of power in the red MOT sequence (figure 3.5) smoothly loads the atoms into the prealigned reservoir trap. For ^{88}Sr, the trapped atoms are visible in in-situ images, as shown in figure 3.6 d). We use the in-situ images to align the trap to the red MOT position. For optimized loading, we fine-adjust the position

of the red MOT with the compensation fields. Additionally, we ramp down the red MOT power to zero over 100 ms to further cool the atoms as they are held by the reservoir trap. In the case of ^{87}Sr, the density in the reservoir trap is too low for in-situ images. However, we can fall back on the imaging method of recapturing in the blue MOT to optimize the trap loading procedure and estimate the loading efficiency.

Once atoms are in the reservoir trap, a power modulation spectroscopy verifies the trap geometry [90]. Power modulation is performed using a Red Pitaya FPGA signal generator connected via the external modulation port of the AOM drivers. The Red Pitaya outputs a triggered burst of programmed oscillations at variable frequencies. The modulation depth is 10 % for a fixed number of cycles. Subsequently, the atoms are imaged in TOF. Figure 3.8 shows the atom number depending on modulation frequency, showing resonances at 465 Hz and twice its frequency around 930 Hz. Taking into account the measured waist (Section 2.5), a trap geometry of $w_x \times w_y = 290\,\mu m \times 25\,\mu m$ fits best to the measured trap frequencies for a power of 4 W. For the same power, we achieve up to 90 % loading efficiency for ^{88}Sr atoms. For ^{87}Sr atoms we achieve up to 15 % loading efficiency for an increased power of 9 W. The reservoir trap alignment is further optimized by measuring the atom number after a ramp-down to lower trap powers. Detrimental tilts in the reservoir beam cause a strong atom loss and are compensated by aligning the reservoir trap beam and maximizing the atom holding time at minimal trap power.

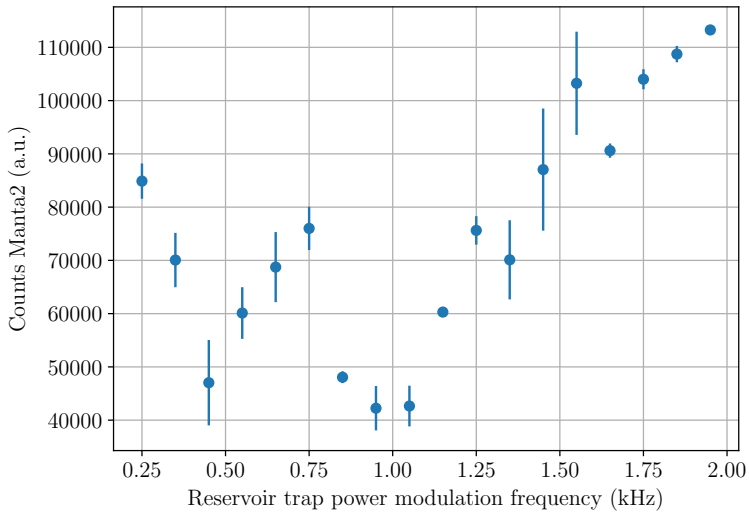

FIGURE 3.8: Reservoir dipole trap modulation spectroscopy for characterizing the trap geometry. The atom number is measured with absorption imaging on the Manta2 camera as function of the reservoir trap modulation frequency with 10 % modulation depth. The power modulation parametrically heats atoms out of the trap at resonances of multiples of the vertical trap frequency.

Chapter 4

Single atom production

In order to develop single-atom spin-resolved imaging, a first step consists of single atom preparation and detection. Commonly, tweezer setups are used to prepare and detect single atoms, which is the topic of this chapter [91, 92, 93]. Preparation of single atoms in tweezer traps involves loading the trap from the cold atomic cloud, isolation of a single atom, and detection with fluorescence imaging.

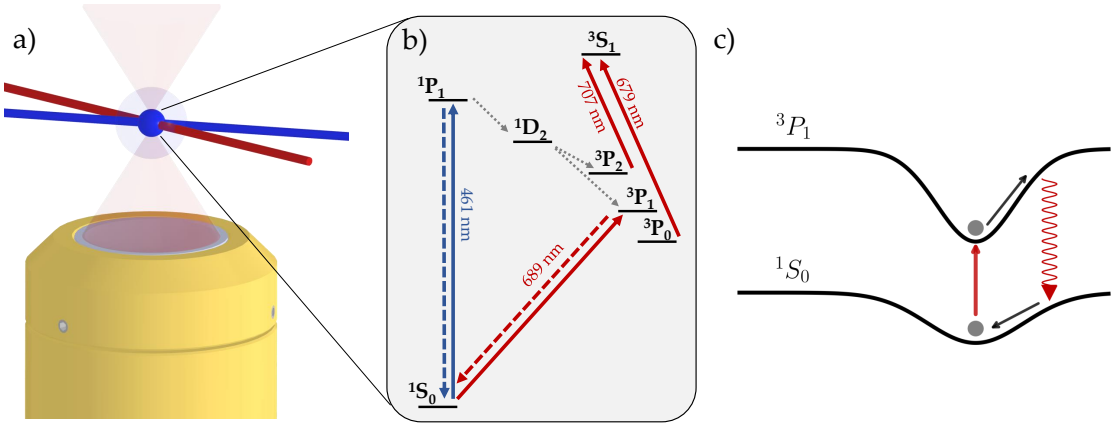

FIGURE 4.1: Illustration of imaging a single strontium atom inside a tweezer trap. a) The essential components of the tweezer setup include a strongly focused 813 nm tweezer beam, a blue imaging beam and a red Sisyphus cooling beam. b) Imaging includes the broad 461 nm imaging transition, simultaneous Sisyphus cooling on the narrow 689 nm transition and repumping. c) The Sisyphus cooling mechanism exploits the steeper trapping potential experienced by the excited state compared to the ground state in order to remove energy in an absorption-spontaneous emission cycle [91].

The working principle is illustrated in 4.1. In our setup, a 813 nm laser beam passing through a high-NA objective creates a tight tweezer trap. Once atoms are excited with blue or red light, they undergo light-assisted collisions and leave pairwise the trap [51]. This process deterministically reduces the number of atoms to either one or zero and is referred to as parity projection. The remaining one or zero atoms are illuminated with blue light on the broad 461 nm transition, and the resulting fluorescence is collected through the objective onto the EMCCD camera. The downside of blue imaging is the simultaneous strong heating rate. Moreover, the blue imaging transition is not closed, which makes repumping necessary. A Sysiphus cooling mechanism on the $^3P_1$ transition mitigates the heating from imaging. As presented in figure 4.1 c), the narrow transition selectively excites atoms from the trap bottom to the $^3P_1$ state. The trapping potential for the $^3P_1$ state is steeper than the

ground state potential. On average, the atom transfers more kinetic energy into potential energy than it regains when it decays back into the ground-state potential [91].

This chapter is organized as follows: First, we characterize the tweezer setup, including the initial trapping of atoms in section 4.1. Next, we describe the preparation and imaging of a single atom, followed by an investigation of cooling optimization for a single atom within the tweezer in section 4.2. The chapter concludes with an assessment of the fidelity in achieving the goal of preparing cold single strontium atoms.

4.1 Tweezer setup characterization

Usually, tweezer experiments use a pair of microscope objectives to image the focus produced by one objective and vice versa. In our setup (Setup 2.5.4), which uses a single objective, we rely on the atoms as a probe for the tweezer trap. In this section, we present the characterization of the tweezer trap and the Sisyphus cooling beam with ^{88}Sr atoms.

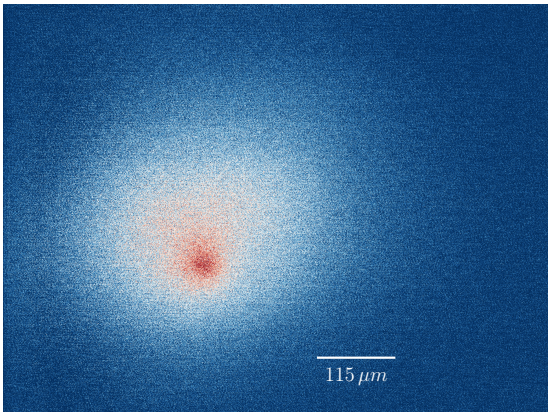

FIGURE 4.2: Image of the cold ^{88}Sr red MOT with the tweezer trap. The fluorescence image is taken from below via the objective and Manta1 camera setup and 100 μs illumination with the blue MOT beams. For a successful loading of the tweezer trap the cold red MOT is precisely moved into the focus of the objective until a localized increase of density is visible.

The tweezer trap is loaded with atoms from the final stage of the cold red MOT. With a pre-aligned objective (Section 2.5.4), the initial loading of the tweezer is visible in a local increase of density with the Manta1 imaging system. The first step is to move the final cold rMOT into the focus of the Manta1 camera. In order to have a deep enough trap, we start with 150 mW in the tweezer beam. Then, the imaging system shows the local density increase with respect to the entire rMOT size as presented in figure 4.2. Crucial for a successful loading is the precise tuning of the red MOT height. For ^{87}Sr, the local density increase is better visible with the help of the reservoir dipole trap. A tweezer loaded with ^{88}Sr atoms produces a sufficiently strong fluorescence signal that it can be further characterized in terms of its trapping frequencies.

4.1.1 Tweezer trap

The first characterization step measures the tweezer trap depth and geometry. For successfully trapping strontium atoms, the tweezer trap can have any geometry provided that its trap depth largely exceeds the cold red MOT's temperature. However, for a successful parity projection and Sisyphus cooling mechanism, the trap confinement needs to be strong enough. As a target trap frequency, we used 100 kHz, similar to what has been used in

other experiments [91]. This trap frequency ensures that atoms are squeezed close to each other to perform light-assisted collisions. Furthermore, the resulting oscillation time is small in comparison to the lifetime of the $^3P_1$ state and thus small enough that the atom in the excited-state trap gains substantial potential energy before it decays back into the ground-state trap. To check that our tweezer setup yields a strong enough confinement, we used power-modulation spectroscopy and a spectroscopic light-shift measurement.

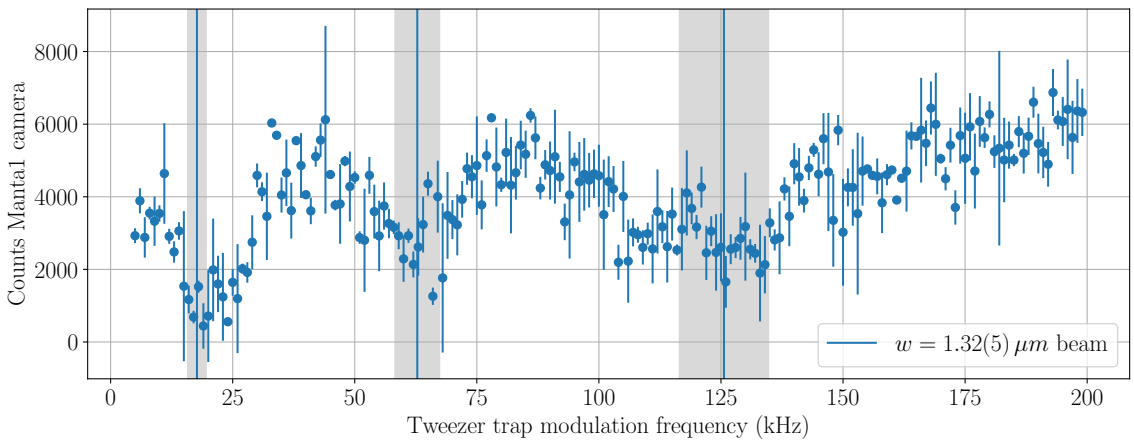

FIGURE 4.3: Power modulation spectroscopy for characterizing the single tweezer trap at 56 mW. The atomic fluorescence signal on the Manta1 camera as function of the modulation frequency shows a longitudinal trapping frequency of 12.3 kHz and a radial trapping frequency of 63.6 kHz corresponding to a beam waist of $w = 1.32(5)\,\mu$m. The gray region indicates the considered uncertainty on the resonance position and consequently the beam waist.

The power modulation spectroscopy measurement sequence is the same as in the reservoir dipole trap characterization (Section 3.4). The measurement had to be done at a power of 56 mW in order to keep the expected trap resonance within the modulation bandwidth of the tweezer beam setup. We obtain 63 kHz radial and 12.4 kHz longitudinal trapping frequency, which is translated into a tweezer beam waist of $w = 1.32\,\mu$m. The uncertainty on the tweezer waist analysis is estimated in figure 4.3 with the resonance region of a ± 50 nm modification of the beam waist. The result shows that our microscope setup does not produce the expected beam waist of $w = 900$ nm that the objective was designed for. An optimization of the tweezer beam waist requires a refinement of the microscope setup. Proper alignment involves focus adjustments, centering, and tilting of the objective and optical path components to produce minimal aberrations. Another source of aberrations to be checked is wavefront distortions in reflections from dichroic mirrors. As a consequence of the enlarged tweezer waist, we had to use the full power of 150 mW from the 813 nm laser system in the single tweezer beam to reach a radial trapping frequency of around 100 kHz. The resulting trap depth at full power of 150 mW and $w = 1.32(5)\,\mu$m waist is 2 mK.

The alternative measurement of the tweezer beam waist derives the beam waist from the light shift that is induced by the 813 nm tweezer light at full trap power. The light shift can be directly measured by performing spectroscopy on the narrow 689 nm transition with trapped atoms.

After loading the tweezer trap, we apply the red MOT beams for 10 ms, and monitor the fluorescence signal from the atoms in the tweezer trap as a function of the red light frequency. The excitation to $^3P_1$ causes light-assisted collisions and is measured as losses

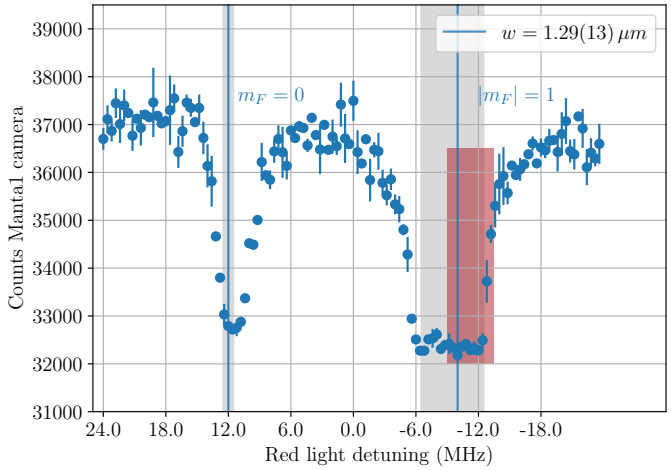

FIGURE 4.4: Light shift measurement of tweezer trap at 150 mW with spectroscopy on the 689 nm transition. The atom loss from the tweezer trap is induced through excitation to the $^3P_1$ state with the red MOT beams and subsequently imaged on the Manta1 camera as function of the red light frequency. The tweezer beam waist is estimated from the light shift difference of the $^3P_1$ Zeeman states. The gray regions indicate the uncertainty on the resonance position and the estimated beam waist of $w = 1.29(13)\,\mu$m. The red shaded region indicates the expected frequency region where the Sisyphus cooling mechanism works.

from the tweezer trap. The 689 nm transition is sufficiently narrow to resolve the differential light shift of the $^1S_0\, m_F = 0 \rightarrow {}^3P_1\, m_F = 0$ and the $^1S_0\, m_F = 0 \rightarrow {}^3P_1\, m_F = \pm 1$ transition that arises from the tensor part of the excited state polarizability of the $^3P_1\, m_F = 0$ and $^3P_1\, m_F = \pm 1$ states. The measured loss spectrum is presented in figure 4.4.

In order to obtain the tweezer beam waist from the light shift difference, we analyze the formula for the total light shift of an atom in the state $|F, m_F\rangle$ in a linearly polarized light field with wavelength λ [94].

$$\Delta E_{F,m_F} = -\frac{I}{2c\epsilon_0}\left[\alpha^{(s)}(\lambda) + \alpha^{(t)}(\lambda)\,\chi(\theta)\,\frac{3m_F^2 - F(F+1)}{F(2F-1)}\right] \tag{4.1}$$

The energy shift stems from the coupling of the electric field to the polarizability of the atom. The electric field of the light is expressed through the beam intensity I. The polarizability of linear polarized light is composed of the scalar $\alpha^{(s)}$ and tensor polarizability $\alpha^{(t)}$. The polarizabilities are atom specific quantities and calculated for strontium in Appendix B. The scalar light shift is independent of the Zeeman level m_F and the polarization of the light. In contrast, the tensor light shift depends on the angle θ of the light polarization with respect to the quantization axis and thus the Zeeman level m_F. In our case, the polarization of the tweezer beam is parallel to the quantization axis that is set in the direction of the Sysiphus cooling beam. Thus the term $\chi(\theta) = (3\,cos^2(\theta) - 1)/2 = 1$.

By calculating the total light shift for the $^3P_1\, m_F = 0$ and $^3P_1\, m_F = \pm 1$ states and equating with the measured light shift difference of 23 MHz, we can isolate the tweezer beam intensity. For a tweezer beam power of 150 mW, we determine a beam waist of $w = 1.29\,\mu$m, which is consistent with the waist measurement obtained through power modulation spectroscopy. However, the $m_F = \pm 1$ resonances are less well resolved than the $m_F = 0$ resonance, resulting in an uncertainty in the beam waist measurement of ± 130 nm.

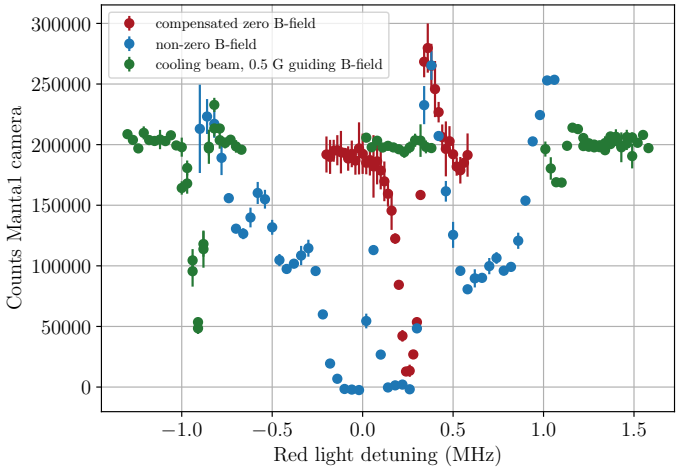

FIGURE 4.5: Spectroscopic measurement and setting of a compensated guiding B-field. The atom losses in the reservoir dipole trap are measured depending on the frequency of the red MOT beams and the cooling beam. For a zero magnetic field, the resonances of the three different m_F-states merge to one single resonance. For a guiding field of 0.5 G, properly set along the propagation of the Sisyphus cooling beam, mostly one σ-transition is visible in the spectrum.

4.1.2 Sisyphus cooling beam

In addition to a sufficiently deep tweezer trap, an essential aspect is an effective Sisyphus cooling beam. To effectively cool, the cooling beam requires the correct frequency and polarization setting.

An acceptable cooling frequency range for the Sisyphus cooling mechanism can be inferred from the light-shift spectrum. This region in figure 4.4 is indicated in red. In this region, the cooling beam is resonant to the $m_F = \pm 1$ states at the trap bottom.

The cooling beam necessitates circular polarization to drive the cooling transition. Subsequently, circular polarization is also required to perform optical pumping to the stretched states of the ground-state spin manifold in ^{87}Sr. In turn, achieving circular polarization requires a well-defined guiding magnetic field aligned along the light-propagation axis. We exploit the narrow 689 nm transition again to resolve the magnetically sensitive Zeeman states and measure the surrounding guiding field. Instead of the tweezer trap, we load the ^{88}Sr MOT into the reservoir dipole trap. The reservoir dipole trap operates at minimal trap depth to minimize the light shift from the reservoir. To set a zero magnetic field first, we use the red MOT beams as probe light to have all polarization components. By tuning the compensation fields, we merge the $m_F = \pm 1$ state resonances to one resonance as shown by the orange data in figure 4.5.

For the required circular polarization of the cooling beam, we only want to excite one σ-transition. We set a guiding field of 0.5 G to the incoming propagation axis of the cooling beam in order to separate the $m_F = \pm 1$ states by their Zeeman shift of 2 MHz (Appendix A). According to the green curve in figure 4.5, we have a dominant σ-transition, strong suppression of the π-transition, and minimal contribution from the opposite σ-transition. The spectroscopically checked polarization and frequency of the cooling beam enable the single-atom imaging in the next step.

4.2 Single-atom imaging and cooling

With a characterized tweezer setup, the imaging and cooling parameters are adjusted to produce and detect single atoms. Thanks to the deep tweezer trap, the loading of ^{88}Sr atoms is robust, and the fully loaded tweezer trap has a strong visibility on the EMCCD camera. Once the red cooling light with frequency in the prior found cooling frequency region is applied to the atoms before the imaging process, the fully loaded tweezer trap signal reduces to a one or zero-atom signal as shown in figure 4.6 b) and 4.6 c).

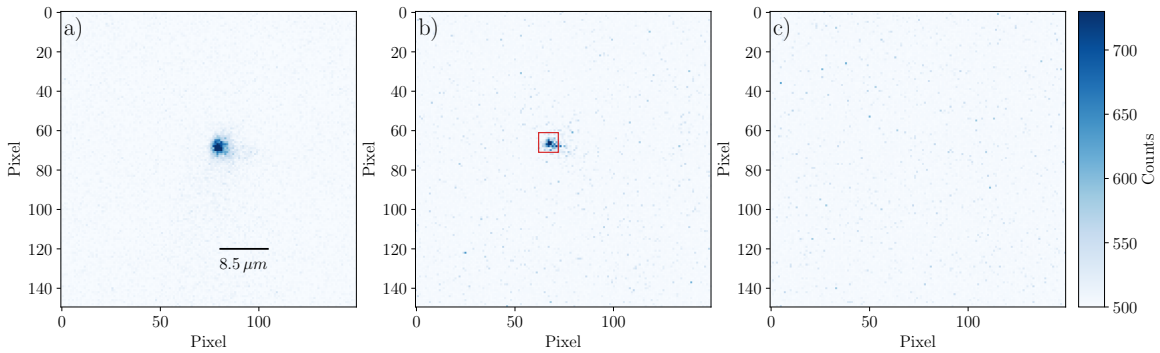

FIGURE 4.6: EMCCD images of atoms in the tweezer trap. a) Fluorescence image of a fully loaded tweezer trap. b) In case the Sisyphus cooling beam is operating parity-projection to a single atom happens and the fluorescence signal reduces to the signal of a single atom. The red rectangle indicates the ROI. c) Reference image of no atom.

We perform a sequence of two consecutive images of the presumably single-atom signal to find the correct cooling frequency and imaging intensity. Repeated imaging indicates whether a single atom has been present or not. At the correct cooling frequency, the red cooling light mitigates the heating due to blue imaging light and allows to image the same atom in two consecutive images. We alternately scan the red cooling frequency and blue imaging intensity until we can routinely prepare a single atom with high survival probability. For the scans of the two crucial parameters, we use the maximal intensity of 200 I_{sat} in the red cooling beam. The cooling beam is switched on 100 ms before the blue imaging beam to perform parity projection. During the imaging, the red cooling beam and repumpers are constantly on. For maximal survival probability, an alternating blue imaging beam with a repetition time of 50 ms and a duty cycle of 50 % is crucial. The total imaging time is usually 1.6 s at an EMCCD gain of maximally 100.

At optimized imaging parameters, we detect single atoms over a 3 MHz broad cooling frequency region (figure 4.7 a),b)). With a smaller detuning, the parity projection still produces one atom in the first image, but the cooling is not strong enough to keep it for the second image. For too large detuning, the red parity projection and cooling do not work, and only the fully loaded tweezer is imaged with the first picture.

With a properly working Sisyphus cooling, the blue imaging intensity can be varied over a wide range, as shown in figure 4.7 c),d). Thanks to the deep tweezer, the blue fluorescence can be increased to generate a large separation between no-atom and a single-atom signal before the imaging-induced heating becomes too strong. However, the typical settings are chosen to give a robust loading probability of 50 % and the highest survival probability.

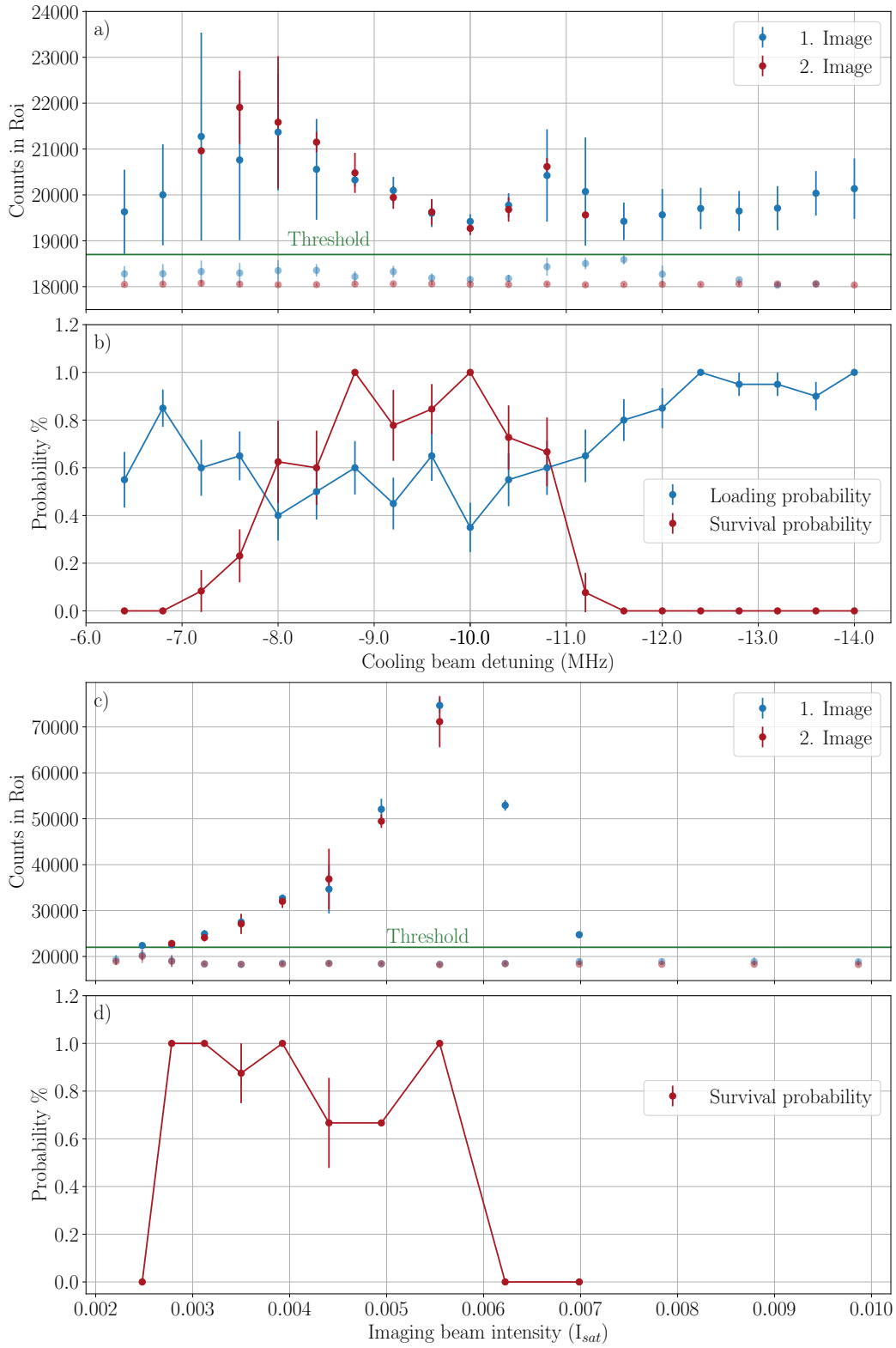

FIGURE 4.7: Sisyphus cooling frequency and blue imaging intensity scan for achieving single-atom detection in two consecutive images. a) The fluorescence signal as function of the cooling beam detuning for the 1. and 2. image. b) The loading probability is extracted from the number of 1. image shots with signal above the green detection threshold with respect to total amount of 1. image shots. The survival probability is similarly derived as the ratio of 2. image shots and 1. image shots with a positive single atom signal. c) The single atom fluorescence signal as function of the imaging beam intensity. d) The survival probability is similarly derived as in b). The uncertainty on the survival and loading probabilities are given by the standard deviation of the mean obtained through bootstrapping the data [95].

4.2.1 Single-atom detection fidelity

Ultimately, our single-atom imaging procedure has a high fidelity of detecting a single atom and allows us to do up to 200 repeated images. We have chosen a sequence that gives robust single-atom evidence rather than optimized timings. Our imaging sequence at full tweezer power uses the typical cooling frequency of 10.4 MHz and a blue imaging intensity of 0.0035 I_{sat}. The sequence is part of the subsequent cooling optimization and shown in figure 4.9.

As a consequence of the deep tweezer trap, we have a strong light shift on the blue transition of 72 MHz. With our blue imaging setup, the blue imaging beam is 30 MHz detuned from resonance, which leads to a photon-scattering rate of 11 kHz.

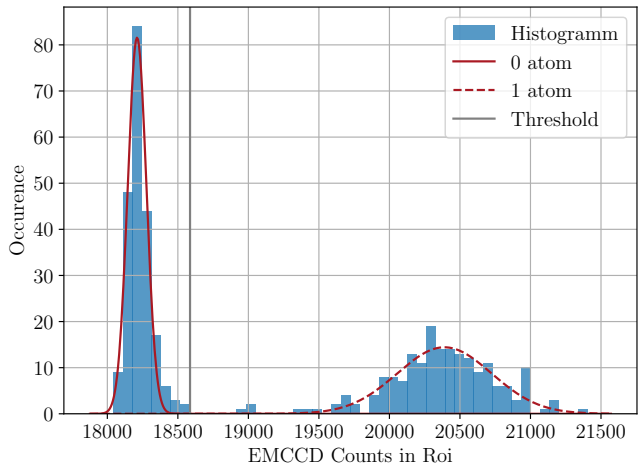

FIGURE 4.8: Single atom detection histogram. The histogram displays the distribution of EMCCD signal counts over 400 measurement shots, taken with an exposure time of 1.6 s. The images were taken at optimal imaging settings of 0.0035 I_{sat} blue imaging light and 200 I_{sat} red cooling light at 10.4 MHz detuning from the free-space resonance. The two peaks correspond to the cases with zero atoms and single atoms. The single-atom detection threshold is defined at the intersection point of the two fitted Gaussian distributions, where the error of the atom assignment is equal.

A quantification of the single-atom detection fidelity is given by a histogram of detected fluorescence signals, as shown in figure 4.8. The histogram displays the zero-atom and single-atom peaks, which are fitted with Gaussian probability distributions. The probability of a detection error in wrongly identifying a zero atom as one atom or vice versa is directly related to the overlap of the two distributions. The single-atom threshold is defined at the intersection where the two distributions have an equal overlap and minimise the combined detection error. Due to the large separation between the peaks, this overlap is small. Based on the current data and the selected detection threshold, the detection fidelity is estimated to exceed 99.9 %. However, it is important to note that we have a limited sample size, and some shots are not well captured by the Gaussian fits. To reliably quantify the error on the estimated fidelity at a level comparable to other groups, which typically have a fidelity well above 99.9 % [91], a larger dataset would be necessary. Nonetheless, the histogram confirms the presence of single atoms and robust single-atom detection. The final spin-separation experiment does not rely on a high-fidelity single-atom preparation since the required free-space imaging technique can independently detect single atoms.

Regarding the choice of isotope for single-atom imaging, the initial characterization was performed with ^{88}Sr. This isotope offered a more straightforward implementation due to its higher loading efficiency, which facilitated the robust preparation of single atoms.

However, the imaging and detection protocols developed for ^{88}Sr can be effectively transferred to ^{87}Sr. Although the loading efficiency with ^{87}Sr is lower, the overall detection fidelity and survival probabilities remain the same.

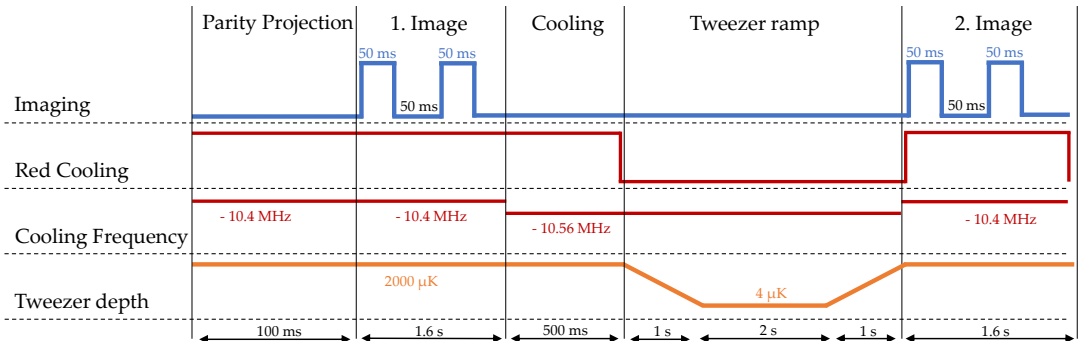

FIGURE 4.9: Sequence for Sisyphus cooling optimization. The sequence is divided in initial imaging with Sisyphus cooling, isolated Sisyphus cooling, ramp down of tweezer trap and second imaging at initial tweezer trap depth.

4.2.2 Cooling optimization

The single-atom imaging allows us to optimize the Sisyphus cooling with single-atom resolution by holding the atom in a variable trap depth. A low temperature of the single atoms is important for the subsequent spin separation. There, we want to minimize the spatial spread after the atoms will be released from the tweezer trap for the optical Stern-Gerlach separation and final free-space imaging.

For cooling optimization, we reference the atom temperature against a ramped-down tweezer trap. The full sequence is shown in figure 4.9. After the parity projection and the first image, we have a dedicated cooling stage for the cooling beam at an optimized frequency. Afterward, we ramp down the tweezer to a variable tweezer power. We hold the atom at low tweezer depth for 2 s before we ramp up again and take the second image. We then infer the optimal cooling frequency from the maximal survival probability. We can ramp down the tweezer power to 0.2 % of the initial 150 mW, which reduces the trap depth from 2 mK to 4 μK. The survival probability from the first to the second image becomes sensitive to the optimal cooling frequency, which we have found to be around 10.56 MHz red-detuned from the free-space resonance with a 100 kHz width. The spectrum of the optimal cooling frequency is shown in figure 4.10.

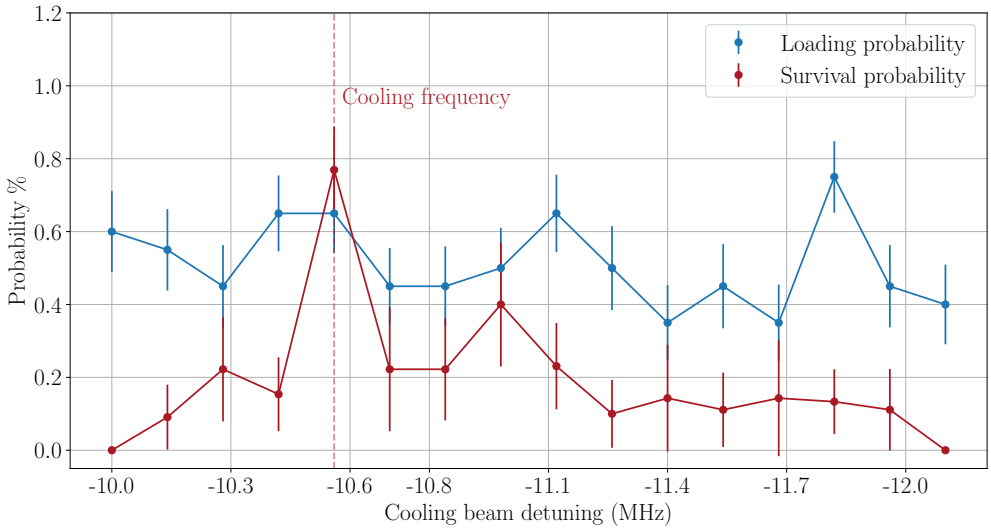

FIGURE 4.10: Sisyphus cooling optimization. Two consecutive single-atom images are taken as scan of the cooling frequency in the Sisyphus cooling stage of the cooling optimization sequence. The survival propability is extracted from the ratio of detected atoms in both images and is revealing the optimal cooling frequency. The uncertainty on the survival and loading probabilities are given by the standard deviation of the mean obtained through bootstrapping the data.

4.2.3 Imaging resolution

Finally, an image analysis of the single atoms reveals the imaging resolution of our microscope setup. We know from power-modulation spectroscopy that the tweezer waist doesn't reach the diffraction limit. Therefore, we fit a simple Gaussian to an averaged image of 200 single-atom images as shown in figure 4.11. The spatial spread is defined as the standard deviation of the fitted anisotropic Gaussian distribution. With that, the fitted images of a single atom have a spread of $\sigma_x = 901\,\text{nm}$ and $\sigma_y = 733\,\text{nm}$, which is about 2.3 times larger than the theoretical diffraction limit of $\sigma = 352\,\text{nm}$ for the 461 nm imaging light. The result indicates the presence of strong aberrations. Notably, the averaged image displays a tail to the right side, attributable to residual coma.

No further analysis of the single-atom point spread function has been done to optimize the imaging system. The only alignment procedure performed was a fine adjustment of the imaging lens position to produce the smallest possible image of a single atom on the EMCCD camera. In principle, this can be fixed by properly aligning the objective and imaging components in terms of tilt, centering, and focal position based on the single-atom image spread. The present limited resolution is sufficient to resolve single atoms in tweezers, but it will have two consequences for follow-up applications. Firstly, the resolution won't be able to resolve atoms in an optical lattice with a typical 532 nm lattice spacing. Furthermore, the present microscope setting affects the resolution of the free-space imaging, as will be discussed in the next chapter.

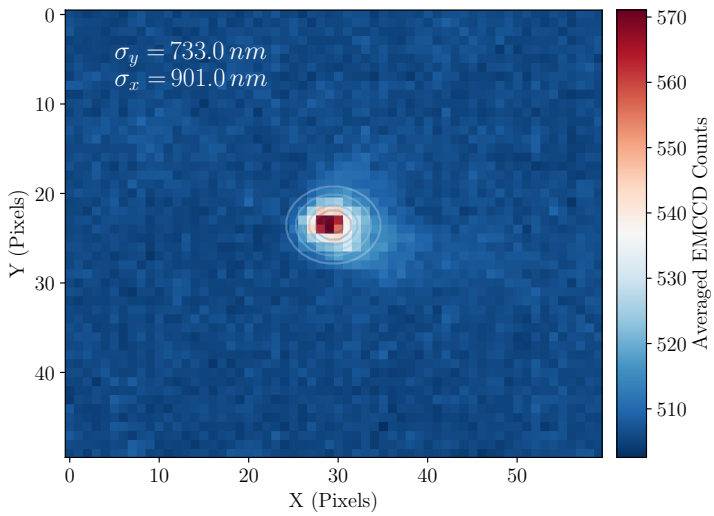

FIGURE 4.11: Averaged image of 200 single atom images. A 2D anisotropic Gaussian distribution is fitted to the image to reveal the imaging resolution of the EMCCD imaging system. The spatial spread is defined as the standart deviation σ. The imaging setup has a magnification of 47.64 and the pixel size is 16 μm.

Chapter 5

Spin-resolved imaging of single atoms

In the final chapter, we bring together the experimental parts of previous chapters to demonstrate spin-resolved imaging of single ^{87}Sr atoms. We use the tweezer setup to prepare single atoms and use an additional optical Stern-Gerlach (OSG) beam to create a spin-dependent potential and spatially separate the atoms based on their nuclear spin state m_F.

A comparison with the original Stern-Gerlach experiment, as presented in figure 5.1, allows us to identify three important aspects for the successful implementation of this approach. The original Stern-Gerlach experiment demonstrated the quantization of the angular momentum by deflecting silver atoms in an inhomogeneous magnetic field and showing a splitting in two separate directions rather than a classically expected continuous distribution [96].

To achieve this resolution, the first important measure was the reduction of the momentum spread of silver atoms, which directly translates into a position spread on the detector screen. The atomic beam emitted from the oven was collimated by selecting atoms with small transverse velocities through the placement of an aperture. In our experiment, we implement the momentum filtering by preparing low-entropy samples of single atoms in the tweezer and further ramping down the tweezer potential. The evaporative momentum filtering provides low-temperature atoms with reduced velocity spread.

A second important aspect is the strong magnetic gradient field, which deflects the atomic beam strongly enough to detect a spin-dependent spatial separation on the screen. For silver atoms, an electromagnet with cutting-edge magnetic field design was required. In comparison to silver atoms with no orbital but electronic spin, ground state strontium atoms have neither orbital nor electronic spin but a nuclear spin. An unrealistically large magnetic field would be required to separate them owing to the weak magnetic-field sensitivity of nuclear spin states. We instead resolve this technical limitation by creating an optical potential gradient with a high-intensity focused optical Stern-Gerlach (OSG) beam [43, 44]. The frequency and polarization of the OSG beam is chosen to create a spin-dependent coupling to the ground state manifold and, ultimately, a spin-dependent potential.

The final aspect of our approach is the imaging of single atoms in free space to detect their spatial separation. Conventional fluorescence imaging of trapped single atoms with additional cooling inside traps generates a large amount of photons coming from a localized trap site. In contrast, during free-space imaging, the atom scatters photons and is randomly accelerated by the recoil momentum imparted by the photons, thereby reducing spatial resolution. We employ a fast free-space imaging technique [67, 68] on the broad $^1P_1$-transition inside a light sheet trap at the focus of the objective, to rapidly detect enough fluorescence photons for single-atom identification and simultaneous high spatial resolution.

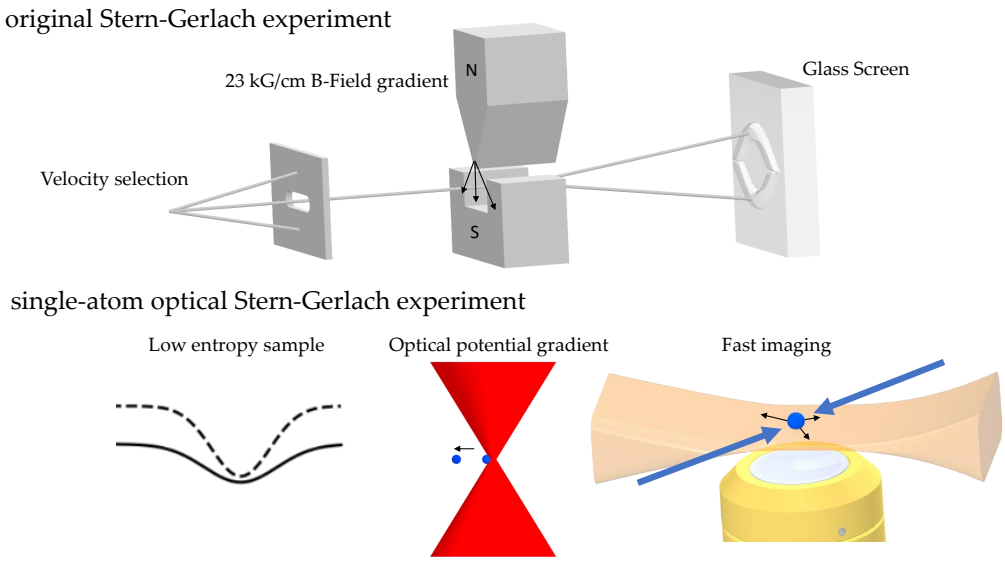

FIGURE 5.1: Comparison of the original Stern-Gerlach experiment with an optical single-atom spin-resolved detection method. In the Stern-Gerlach experiment, an atomic beam of silver atoms is first collimated through apertures to reduce the momentum spread. Afterwards, a non-uniform magnetic field applies a strong enough spin-dependent force on the atoms to spatially separate their trajectories based on their spin. Finally, the silver atoms coat a glass plate showing two distinguishable distributions. Translating this technique to the single-atom level with ^{87}Sr atoms requires the preparation of single atoms with low entropy in a tweezer trap. Instead of an unrealistically large magnetic-field gradient a high-intensity optical Stern-Gerlach beam creates a spin-dependent potential gradient. Subsequently, the distinct spatial positions after in plane expansion are imaged inside a light sheet trap in the focal plane of the objective. For high spatial resolution, the detection requires a fast single-atom imaging technique with minimal imaging spread.

The experimental procedure is detailed in the following three sections. In section 5.1, we demonstrate single-atom detection by implementing the blue free-space imaging technique. The free-space imaging requires a camera noise characterization and image post-processing to obtain single-atom sensitivity. In the next section 5.2, we describe the choice of OSG beam parameters and their characterization. Section 5.3 demonstrates the use of the OSG beam to separate 4 nuclear spin states out of a maximum of 10 within the ^{87}Sr ground state spin manifold. Furthermore, we describe the production of spin-polarized ^{87}Sr atoms and the imaging of coherent nuclear spin dynamics following a quench of the magnetic guiding field. In section 5.4, we conclude with a discussion of alternative OSG beam settings and protocols to extend this technique to more spin states. This chapter is closely related and adapted from the results presented in [97].

5.1 Free-space imaging of individual atoms

The chosen spin-separation approach of spatially separating the atoms with a spin-dependent force ultimately requires an imaging technique of single atoms without a trapping potential. The challenge is to collect enough photons to identify a single atom and to keep a minimal position spread before the atoms are eventually accelerated out of sight.

The imaging linewidth and mass of the atom have a fundamental influence on the imaging performance. The free-space imaging technique has been applied to ^{6}Li atoms

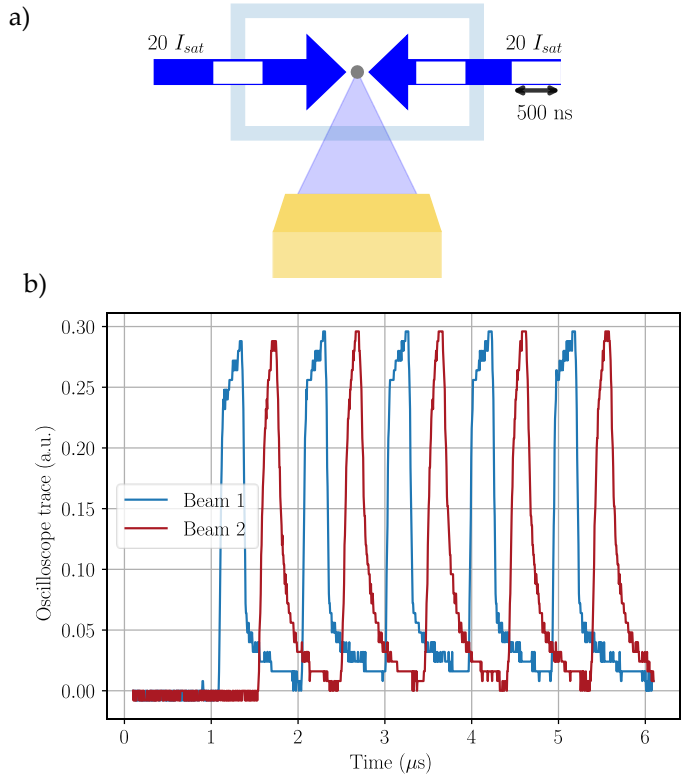

FIGURE 5.2: Free-space imaging illustration. a) Fluorescence is induced by a pair of strongly saturating alternating beams. Single atom imaging system collects about 30 photons on the EMCCD camera. b) The overlap of imaging pulses is minimized and checked by recording the pulses on a fast photodiode. The pulses are generated by two separate AOMs as described in section 2.5.4

[67]. Later, the technique has been adapted to image ^{168}Er atoms released from an optical lattice. In comparison to lithium atoms, the linewidth and mass of erbium are much larger (6 MHz vs. 30 MHz), which drastically speeds up the imaging process and reduces the spatial spread [68]. Applying the free-space imaging to strontium atoms, our experiment should work in a parameter region close to the erbium case. The imaging transition linewidth is similar to erbium, but strontium atoms are lighter, which results in a larger position spread at a fixed number of scattered photons.

A short imaging time is crucial for a minimal position spread and a high resolution in the spatial separation of the atoms after the OSG beam application and subsequent free-planar evolution. This free-space imaging technique is best realized by two counter-propagating imaging beams at high intensity, which are alternated with minimal switching time. The imaging configuration is illustrated in figure 5.2. The high intensity ensures a maximal scattering rate and insensitivity to intensity imbalances. Moreover, the high intensity power broadens the imaging transition, which ensures scattering on resonance even when the atoms are accelerated through the photon recoil and obtain a Doppler shift. Two counter-propagating beams are required to equal out the photon momentum kick. Another important aspect of the two imaging beams is the alternating switching. The alternating switching minimizes the momentum diffusion during the photon scattering and is crucial for single-atom detection as analyzed in [68]. To understand the advantage of alternating imaging beams, we consider two imaging beams driving Rabi oscillations between the ground and excited state before the atom spontaneously decays from the excited state. During the illumination, the atom can absorb a photon from one beam and

afterward be stimulated to re-emit the same photon into the counter-propagating beam. The atom thereby gains two recoil-momentum quanta. The process can continue and in some instances, accumulate several momentum quanta in one direction. If only one imaging beam is on at the time, absorption and stimulated emission cancel out in momentum transfer, and the diffusion to higher momentum is prohibited.

Besides the natural limitations of strontium's atomic properties and the required short exposure time, there is the experimental setup that limits the number of expected photons for single-atom detection. To estimate the photon number, we assume a short imaging time of 15 μs at a maximal scattering rate of $\Gamma_{461}/2 = 2\pi \times 15.25$ MHz. The objective with 0.55 NA has a capture efficiency of 8 %. Due to the reduced transmission of our microscope objective, we estimate at least 60 % photon loss across the entire imaging system, conservatively accounting for dichroic mirrors, the glass cell wall, and spectral filters on the camera. Moreover, the camera has an assumed quantum efficiency of 90 %, resulting in an expected detection count of 31 photons.

As a result, the low expected photon number requires a low-noise camera working in the few-photon regime. Once single atoms can be identified, the imaging parameters are optimized to achieve the highest single-atom detection fidelity at the lowest spatial spread. In addition to that, the free-space imaging technique can simultaneously resolve the number of atoms, as we present with preliminary data in the last section.

5.1.1 EMCCD noise characterization

The low expected photon number and the large magnification of our imaging system (Section 4.2.3) result in a low photon density of 1.2 photons/pixel on the chip. The low signal level necessitates an EMCCD camera with single-photon sensitivity. In comparison to conventional CCD cameras, the photon-counting mode of an EMCCD camera can detect single photons on individual pixels. In order to exploit this high photon sensitivity, a careful characterization of the noise is necessary, which is done in this section following the results of the first free-space imaging demonstration in [67].

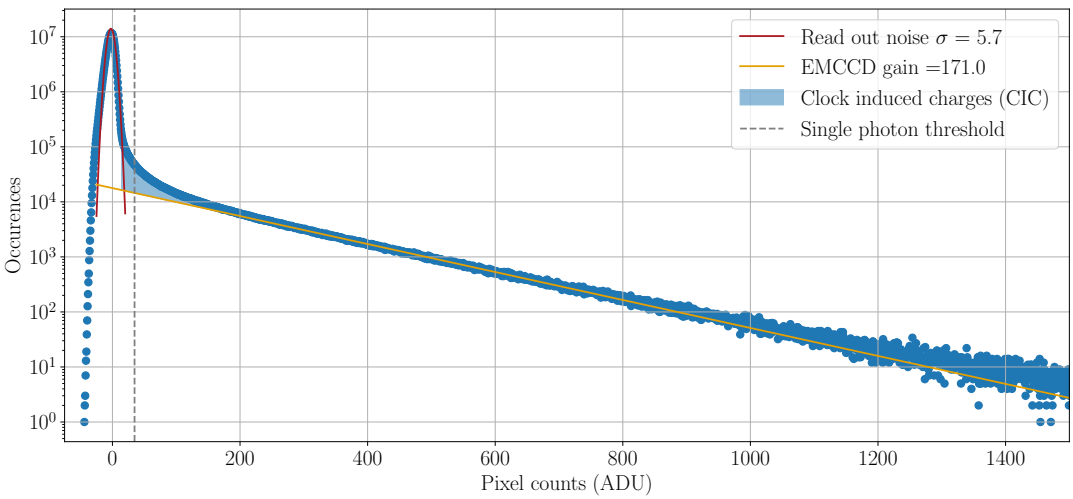

FIGURE 5.3: EMCCD camera noise analysis for working in a low-photon density regime. Histogram of the pixel counts for 1000 dark images with the best camera setting for single photon sensitivity. The photon sensitivity is determined from the ratio of the fitted gain g over the fitted Gaussian distributed readout noise σ_{read}. The single photon detection threshold at $6.5 \times \sigma_{read}$ is a compromise between maximising the photon signal and minimizing the detrimental CIC contributions.

Prior to the noise evaluation, the full imaging system is carefully shielded from stray light to reduce background noise. The camera chip is cooled to $-80\,C^\circ$ to minimize the dark current in the electronics. Furthermore, the readout noise is not spatially homogeneous across the camera ship. We found that the best detection fidelity can be achieved with our camera in an area at the top middle of the EMCCD chip, and moved the image position accordingly.

Afterward, the dominant detection noise source becomes the camera noise itself. In an EMCCD chip, photoelectrons generated by incoming photons are collected in each pixel and shifted towards the amplification register. During the amplification, photoelectrons are amplified into a stochastically distributed number of secondary electrons. The probability distribution of his process is described by the Erlang distribution [98].

$$P_n(x) = \frac{x^{n-1}\, e^{x/g}}{g^n (n-1)!}, \tag{5.1}$$

where g is the gain, x secondary electrons and n the primary photoelectrons. After amplification, the secondary electrons are shifted to the readout register. The benefit of an EMCCD is that it has a generally large gain, which lifts the signal of a single photoelectron above the readout noise. On the contrary, this amplification process means that an EMCCD cannot distinguish between multiple photoelectrons, as a varying number of them are combined into the amplified signal. To optimize single-photon sensitivity, we find the settings that maximize the ratio of gain to readout noise, $\nu = g/\sigma_{read}$. However, in addition to the normally distributed readout noise, an EMCCD camera suffers from clock-induced charges (CIC). CIC occurs during the shifting of photoelectrons from the pixels to the amplification registers. This process causes CIC to be wrongly amplified and afterward detected as real photoelectrons.

To determine the optimal camera settings with maximal $\nu = g/\sigma_{read}$ and minimal CIC contributions, we analyzed 1000 dark shots and plotted the histogram of individual pixel values (ADU). Because a spatially dependent bias exists across the chip, we correct each raw image by subtracting an averaged background image. Figure 5.3 presents the histogram obtained under the best camera setting. The best camera settings are found to be EM gain = 1000, vertical pixel register shifting speed $VSS = 0.5\,\mu$s, horizontal pixel register shifting speed $HSS = 1\,$MHz, small clock-voltage, and pre-amplifier gain = 3 at a dark exposure time of 5 ms. These camera parameters influence the detection performance. Generally, the highest EM gain and the smallest readout noise give the best sensitivity. Using a slow horizontal shifting speed reduces the readout noise, whereas a fast vertical shifting speed minimizes the CIC process [99]. The noise dependence of our camera has been characterized by the manufacturer and listed in table 5.1. However, we found that the readout noise is generally higher and the gain is generally lower than specified. Additionally, the predicted best performance for minimizing CIC at a fast $VSS = 0.3\,\mu$s could not be used in our camera due to missing signals in the readout process and image output.

Quantity	Specified	Measured
Read out noise σ_{read} (ADU)	3.49	5.7
Gain g	231	171
CIC (%)	0.2	2

TABLE 5.1: Specified and measured EMCCD noise characteristics for EM gain = 1000, $VSS = 0.5\,\mu$s, $HSS = 1\,$MHz, small clock-voltage and pre-amplifier gain = 3.

In the histogram of figure 5.3, the normal distribution (red curve) indicates the readout noise and can be quantified with a standard deviation of $\sigma_{read} = 5.7\,$ADU. The exponential

tail far beyond the readout noise reflects the stochastic amplification process. By fitting the Erlang distribution with $n = 0$ to the data between 600 ADU and 1000 ADU (orange curve), we obtain an effective gain of $g = 171$. Together, we obtain a sensitivity of $\nu = g/\sigma_{read} = 30$. The area of the histogram that is not captured by the two fits (blue area) indicates the contribution from the CIC. To be able to confidently distinguish fluorescence photons from camera noise for the subsequent image analysis, we have to set a detection threshold.

We define a single photon detection threshold at $N_c^{th} = 6.5 \times \sigma_{read}$. The choice of the threshold reduces the readout noise contribution to 0.0001 % and makes it practically negligible. Setting this threshold is unavoidably a compromise between keeping the maximal atomic-photon signal and minimizing the contribution of CIC to the detected signal. The choice of N_c^{th} results in an measured 2 % of wrongly detected CIC signal and 80 % detected atomic photon signal. The CIC contribution is obtained by integrating the measured histogram starting from ADU= N_c^{th}. The remaining atomic photon signal is calculated by integrating the Erlang distribution for $n = 1$ photo electrons starting from ADU= N_c^{th}. With that, we have prepared the EMCCD camera for highly sensitive single-atom detection despite the small expected photon density on the camera.

5.1.2 Imaging beam characterization

Crucial for successful free-space imaging of single atoms is the alignment of the imaging beams. Our alignment procedure images the atom cloud from a fully loaded ^{88}Sr tweezer, as shown in figure 5.4. We use ^{88}Sr because it provides more atoms and a higher signal level in raw images for alignment purposes.

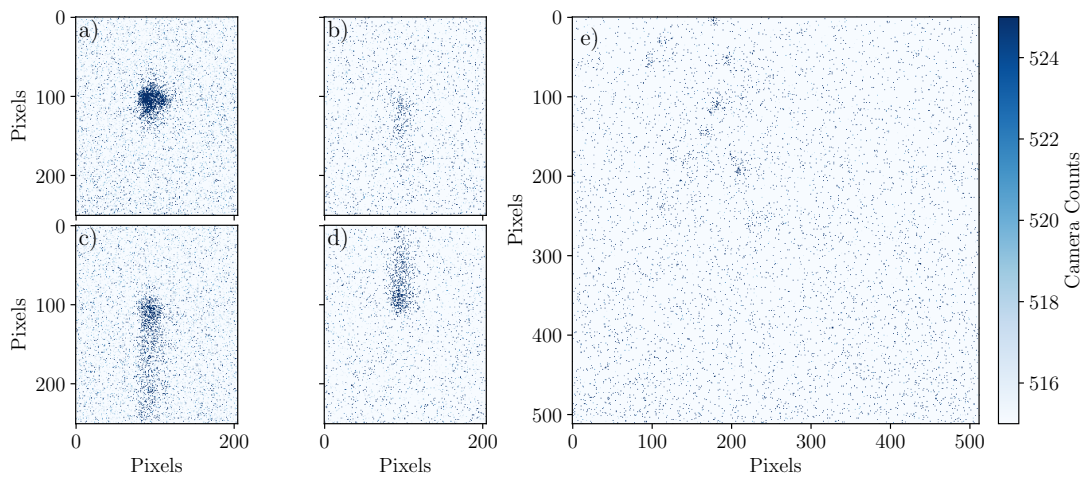

FIGURE 5.4: Alignment of free-space imaging beams. a) The fully loaded tweezer is imaged in free-space with 15 μs of alternating imaging beams. The signal from the fully loaded tweezer is used to optimize the alignment of the individual imaging beams. b) Misaligned free-space imaging beam which is improved to give a larger signal as shown in c). If both beams give the same image of the fully loaded tweezer as in c) and d), the free-space imaging is optimized as in a). e) Optimized free-space imaging of the fully loaded tweezer after 50 μs of TOF, showing an expanding cloud of individual atoms.

The cloud is released from the tweezer and shortly after illuminated with one of the two beams. First, we align the two beams separately such that the fluorescence signal and the imaging tail of the illuminated atoms in either direction are maximized (figure 5.4 c)-d)). The imaging tail forms due to the acceleration of the atoms through the imaging light.

Afterward, we switch on both beams and observe an increase in fluorescence. To optimize this fluorescence and mitigate any formation of a tail in one direction, we adapt the intensity balancing between the two beams. Although we employ a high intensity of 20 I_{sat} in each beam to reduce the impact of small intensity imbalances, precise intensity balancing remains important. The intensity balancing is most visible in images with single atoms. Figures 5.4 e) shows a free-space image of an expanding atom cloud after 50 μs of TOF, where the density is sufficiently low to identify individual atoms. The expansion results from the momentum spread of the atoms. Control over this expansion can be achieved by ramping down the tweezer depth and selecting colder atoms prior to imaging. We use images of single atoms to finely adjust the intensity balancing. We can observe that at the single-atom level, the two beams in alternating switching mode are strictly necessary to obtain a visible fluorescence signal on the EMCCD. With a single beam or both beams on at the same time we are not able to identify individual atoms. Additionally, we found that using the free-space imaging beam is beneficial for imaging small bulk gases, such as small red MOTs or atoms in the reservoir dipole trap.

5.1.3 Image analysis

With an optimized imaging beam and sensitivity of the EMCCD camera, we can define an image analysis routine of identifying single atoms in raw-count images. Despite the high photon sensitivity, the EMCCD characterization showed that CIC are non-negligible in comparison to the fluorescence signal from a single atom. Moreover, the atoms are still randomly moving during the scattering process and further dilute the fluorescence signal over several pixels. Therefore, a post-processing of the raw EMCCD images is necessary to detect single atoms and quantitatively determine their positions. The data processing is summarized in figure 5.5.

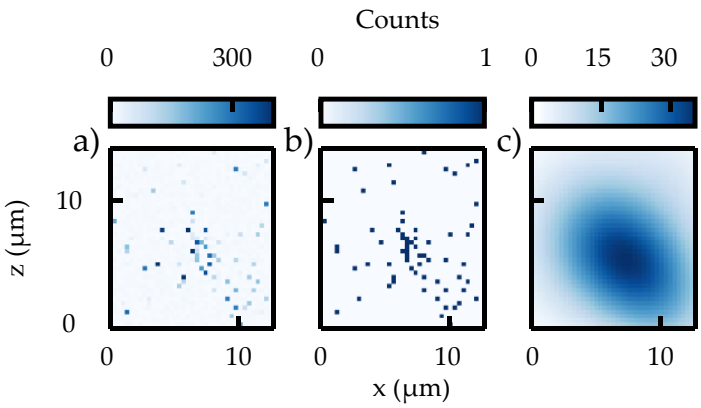

FIGURE 5.5: Data processing steps of a single atom signal. a) Background subtracted raw image b) Binarized raw image with a binarization threshold of $N_c^{th} = 6.5 \times \sigma_{read} = 34.65$. c) Gaussian filtered binarized image, with Gaussian filter size $\sigma_x = 8$, $\sigma_y = 10.4$. The resulting local maxima are used to identify an atom.

First, the background corrected raw pixel map (figure 5.5 a)) is binarized using the single photon detection threshold N_c^{th} (figure 5.5 b)). The binarization sets pixels with non-zero counts above N_c^{th} to a value of 1 and otherwise to 0. This process improves the signal-to-noise for a single photon detection as it removes the camera-induced readout noise and a significant CIC contribution to the detected signal. The remaining CIC is further suppressed by spatial filtering of the binarized images. Thanks to the distinct spatial distributions of atomic signals in comparison to randomly distributed CIC noise,

the atomic signals are revealed by low-pass filtering of the images with a 2D Gaussian kernel (figure 5.5 c)). The optimal 2D Gaussian kernel has the dimensions $\sigma_x = 8$ pixels and $\sigma_y = 10.4$ pixels, although we obtained nearly equal single-atom detection fidelity with $\sigma = 6 \times 6$ pixels.

The binarized, filtered images are then analyzed to find local maxima. The peak values of these maxima are plotted in a histogram, which exhibits a characteristic double-peak structure. Eventually, the distinct separation and possibility to define a threshold between a single-atom peak and a no-atom peak decides which local maximum is an atom, as presented in the next section.

The detection fidelity is dependent on the Gaussian kernel size and is optimized to maximize the overall single-atom detection fidelity. The kernel size is related to the imaging spread. If the kernel size is chosen too small, the detection fidelity decreases, since the obtained signal are comparable to single CIC-induced signals. If the kernel size is too large, the fidelity also decreases, since an increasing number CIC signals are combined in the final signal after spatial filtering. Ultimately, a large kernel size becomes detrimental to the spatial resolution, making it difficult to distinguish atoms that are close together.

5.1.4 Imaging fidelity and spatial resolution

With the defined data analysis procedure, the single-atom free-space imaging is characterized. In order to characterize the fidelity of the free-space imaging, we use the following experimental sequence. First, the tweezer is loaded with ^{87}Sr atoms from the MOT and overlapped reservoir dipole trap. Subsequently, the reservoir trap is switched off, and the tweezer trap is ramped down in 150 ms to $k_B \times 6\,\mu$K, resulting in typically one remaining atom in 50 % of the realizations. The tweezer ramp down reduces the momentum spread. Before imaging, the reservoir dipole trap is ramped up again to $k_B \times 60\,\mu$K to be able to ramp down the tweezer to the lowest radial trap depth as possible without letting the atom fall out of the imaging plane due to a vanishing vertical confinement. It is essential for keeping the atom at the objective focus for high spatial resolution. The reservoir dipole trap also prevents unintended kicking of the atom out of the imaging plane, which could happen if the OSG beam applies a vertical force component to the atoms. The subsequent free expansion in the reservoir dipole trap is kept minimal with 5 μs of TOF time, which is negligible given the low momentum spread of the atoms. For the imaging, we used the counter-propagating imaging beams at our typical intensities of $I = 20\,I_{sat}$. The beams are switched with 500 ns period and minimal overlap of imaging pulses as shown in figure 5.2. During the imaging, a guiding field of 80 mG in z-direction is present.

For characterizing the detection fidelity, we analyze the post-processed images. The histogram of the maxima in 3738 binarized and low-pass filtered images displays a characteristic double-peak structure and allows setting an identification threshold by fitting the histogram. The single-atom detection threshold is set at the intersection where the detection error is minimized, and the two distributions have an equal overlap. The detection fidelity is reduced by the combined probability of wrongly identifying a zero atom as one atom and the probability of wrongly identifying one atom as zero atoms. Figure 5.6 shows the histogramm at 15 μs of imaging time. The atom peaks have a non-vanishing separation between them. The histogram is best reproduced by fitting a skewed Gaussian distribution to the zero-atom peak and a skewed Gaussian plus an offset to the one-atom peak. The fitted histogram results in an imaging fidelity of 98.2(2) %. The uncertainty on the fidelity is given by bootstrapping the data [95].

The offset in the fit model is a consequence of the decay channel from the $^1P_1$ state to the $^1D_2$ state. The lifetime of the $^1D_2$ state is longer than the imaging time and blocks the

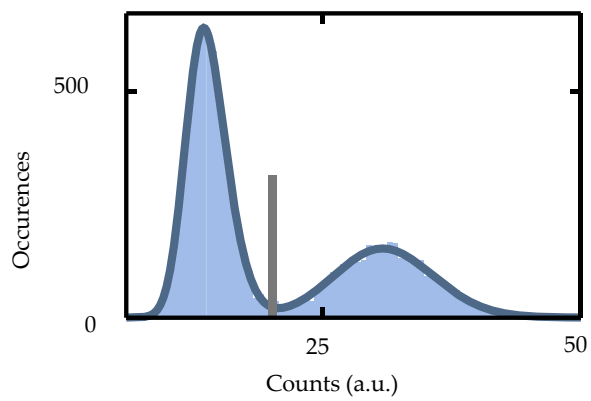

FIGURE 5.6: Single atom detection fidelity. Histogram of the maxima count value of 3738 low-pass filtered images, displaying a characteristic double-peak structure. An imaging time of 15 μs was used with the optimized alternating imaging beam parameters. A fit of the histogram with two skewed Gaussians and an offset defines the detection threshold (gray line) and a detection fidelity of 98.2(2) %.

atom from further photon scattering. Before decaying, the atoms have scattered a distribution of photons, which creates a signal tail of the single-atom peak and is responsible for the signal offset between the zero and one-atom peak. Without directly repumping from the $^1D_2$ state, the stop in scattering is a limitation for increasing the detection fidelity by increasing the imaging time. Eventually, the $^1D_2$ decays to $^3P_1$ and $^3P_2$ and is repumped by our standard repumping scheme. However, this repumping process is limited by the $^1D_2$ lifetime of 350 μs, which is defying the target of fast imaging on μs time scales. Similar conclusions have been drawn from works on fast imaging of ^{88}Sr atoms in tweezers [100]. A solution would be to implement a direct repumping scheme from the $^1D_2$ state. Successful repumping on the $5s4d\,^1D_2 \rightarrow 5s8p\,^1P_1$ transition at 448 nm has already been demonstrated in [101].

The imaging limit of the blue free-space imaging is shown with a scan of detection infidelity as a function of imaging time in figure 5.7 a). As the imaging time increases beyond the optimal imaging time of 15 μs, the infidelity increases with imaging time, due to the decay to the $^1D_2$ state. On the other side, for shorter imaging times, the detection fidelity is limited by the camera noise. The camera noise defines the spread of the zero atom peak. As the imaging time decreases, the atom peaks start to overlap and consequently reduce the detection fidelity.

The best imaging parameters are the settings that simultaneously maximize the single-atom detection fidelity and minimize spatial spread. For characterizing the imaging spread, an averaged raw fluorescence image is fitted with a 2D Gaussian distribution. The spread is defined as the Gaussian standard deviation σ and the uncertainty on the determined spread is obtained from bootstrapping the data. Figure 5.7 b) shows the resulting imaging resolution as function of imaging time.

The spread is increasing for longer imaging times and starts to saturate where the atoms stop scattering due to the $^1D_2$ decay process. For smaller imaging times, the spread reduces but the low detection fidelity does not allow working at this short imaging time. For the remainder of the thesis, the optimal imaging time is set at 15 μs, which yields an imaging spread of $\sigma_x = 1.0(1)\,\mu$m and $\sigma_y = 1.2(2)\,\mu$m. The uncertainty is given by the standard deviation of the measured mean spread.

Optimizing the spatial spread and detection fidelity towards smaller imaging times is limited by three contributing factors. In the current setup, the initial momentum spread

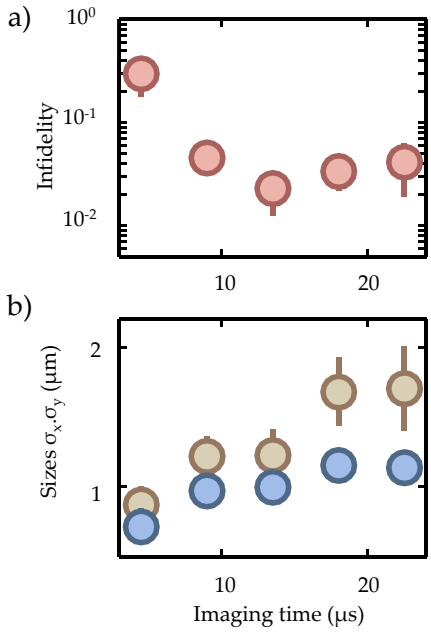

FIGURE 5.7: Optimal free-space imaging parameters. a) Single-atom detection infidelity as a function of imaging time. b) Spatial spread of the atomic fluorescence signal as a function of imaging time. The reported sizes are defined as the standard deviations of the fitted anisotropic Gaussian along its major (yellow) and minor (blue) axis. Error bars represent one standard deviation of the mean and are obtained through bootstrapping the data.

and the imaging system performance limit a minimal achievable imaging time.

The first contribution is the temperature of the atoms. After ramping down the tweezer to $k_B \times 6\,\mu$K, we can assume that the temperature of the remaining atoms is not higher than half the trap depth. According to the Boltzmann distribution, the atoms have for $T = 3\,\mu$K a mean velocity of 16.9 mm/s and thus a maximal spread after 15 μs of 250 nm.

A more significant contributor is the overall imaging resolution of our system. In section 4.2.3 we have characterized our imaging system to have a spatial resolution of $\sigma_x = 901$ nm and $\sigma_y = 733$ nm. Optimizing the imaging system would improve both spatial resolution and detection fidelity. A larger imaging resolution results in a higher signal density, which enhances the separation from the camera noise and thus improves the overall detection fidelity.

The fundamental limiting factor is the momentum diffusion of the atoms during the scattering process. We approximate its contribution by assuming that the atom equally scatters photons with the recoil momentum on the unit sphere and thus performs a 3D random walk. The average positional uncertainty per scattering event can be approximated by the Heisenberg uncertainty principle. As the uncertainty of the momentum is given by the recoil momentum $\delta p = \hbar k$, the positional uncertainty is given by $\delta x = \lambda/4\pi$. For a 3D walk, the root mean square displacement increases with the number of scattering events as $\sqrt{N}$. With a scattering rate of $2\pi \times 15.25$ MHz and an imaging time of 15 μs, the atom scatters 1437 photons and thus has an approximate root-mean-square displacement of at most 1.4 μm.

All in all, our free-space imaging technique achieves fast and high-fidelity detection with micrometer-scale spatial precision which is important for resolving the spatial separation of individual ^{87}Sr atoms in subsequent sections. The demonstrated single-atom imaging fidelity approaches that of in-situ imaging in optical lattice experiments [102]. By

improving the imaging system and employing active cooling techniques for the trapped atoms before the release from the tweezer trap, the free-space imaging resolution can be significantly enhanced towards smaller imaging times. The imaging eventually reaches the fundamental limit imposed by the imaging process itself. Nonetheless, the inevitable spatial imaging spread limits the final spin-separation fidelity.

5.1.5 Atom number resolution

Detecting multiple atoms that are spatially separated is straightforward, as demonstrated in figure 5.4 e), where individual atoms are clearly distinguishable. However, identifying multiple atoms that appear close to each other presents a different challenge. In this section, we present preliminary experimental data to show the possibility of free-space imaging to detect more than a single atom.

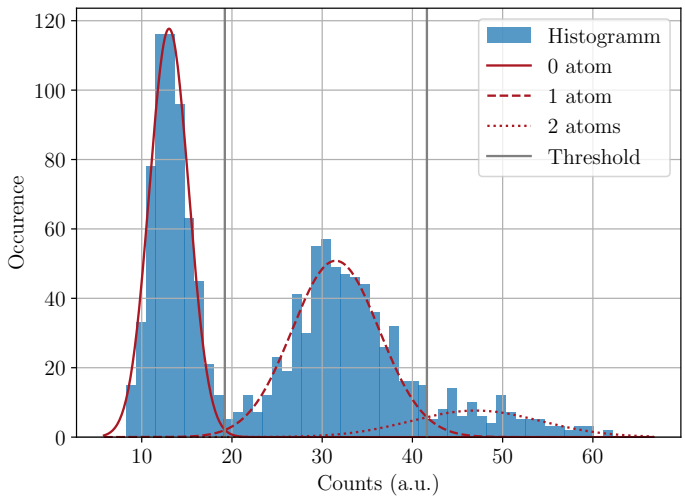

FIGURE 5.8: Free-space detection of more than a single atom. Histogram of detected atom peaks showing a tail of the one-atom peak. The dataset consists of 1293 experimental shots with same image settings as in figure 5.6. The region next to the single atom peak indicates the presence of a second atom or more. The histogram allows a fit of the single atom peaks with skewed Gaussian distributions but has limited detection fidelity for multiple atoms.

Our atom preparation setting occasionally results in multiple atoms being loaded into the tweezer, which was confirmed by experiments involving longer expansion times before imaging. Figure 5.8 shows the resulting histogram under extended loading conditions with the same optimal imaging parameters as in the previous section. The histogram exhibits a tail beyond the single-atom peak, suggesting the presence of a second atom within the same ROI. Fitting the individual atom peaks with skewed Gaussian distributions reveals a consistent detection fidelity of 98.9(5) % for distinguishing no atom from a single atom. However, the two-atom peak has an enlarged spread and larger overlap with the single-atom peak, which yields a detection fidelity of 78(8) % of distinguishing one atom from two atoms. The fidelity uncertainty is determined by bootstrapping the data.

While the histogram shows the potential to image multiple atoms, the confidence in fitting the histogram with multiple Gaussian distributions is limited by three factors. Firstly, the fit quality is limited by statistics and the number of shots with two atoms. A challenge in our experiment was to raise the possibility of having multiple atoms in the tweezer. In our experiment, the number of ^{87}Sr atoms in the tweezer is strongly limited. Extended

reservoir state loading time, optimized blue and red MOT parameters for lower temperatures, only slightly improved the possibility of having more than one atom in the tweezer trap.

Secondly, the overlap of multi-atom peaks increases. One reason for this is the detrimental impact of the decay to the metastable $^1D_2$-state during imaging. The stochastic stop in the scattering process causes a spread of detected fluorescence signals, which is expected to scale with the number of involved atoms. The signal from a third atom in our data may be obscured within the width of its distribution and overlap with signals from other atom-peaks.

The third limitation is saturation in the detection process. The high gain of the EMCCD camera and subsequent binarization are intended for low-photon count and single-photon detection. Stacking the fluorescence from multiple atoms in the same image analysis routine does not detect the expected linear increase of signal with atom number. A solution to that is spreading the atom fluorescence across more pixels and reducing the chance of saturated detection.

In summary, while the results are promising and demonstrate the potential of free-space imaging for multi-atom detection, a comprehensive understanding and quantification of the detection fidelity for multiple atoms requires further data and refined modeling. A potential avenue for further characterizations is the deterministic preparation of multiple atoms in separated tweezers, a repumping scheme from the $^1D_2$ state, and an exploration of adequate imaging settings. These improvements will be the focus of future investigations.

5.2 The optical Stern-Gerlach beam

In the following section, we focus on the optical Stern-Gerlach beam settings that allow us to spatially separate the ^{87}Sr atoms based on their m_F state. A large separation is required to resolve the resulting spin location with our free-space imaging system. Our single OSG beam setup imposes a few constraints on the choice of beam parameters to obtain the optimal OSG potential.

5.2.1 OSG beam design consideration

The first parameter to consider is the beam size. On the one hand, it should not be too large, given the currently limited power of 3.25 mW. On the other hand, it should not be too small, which would make aligning to the fixed tweezer position more difficult. Balancing both, results in a beam waist approximately four times larger than the tweezer beam, leading to a waist of about $w = 4\,\mu$m and a peak-intensity of 12.93 kW/cm^2. In terms of optimal alignment, the OSG beam should be positioned at a distance from the tweezer of half the OSG beam radius. At half the beam radius, the optical gradient is maximal, thus optimizing the force exerted on the atoms.

For a given beam intensity, we are left with choices about detuning and polarization. The polarization critically influences the nature of the OSG potential and the resulting spin separation. This can be understood by analyzing the formula for the light shift which is induced by a light field in an atom in the state $|F, m_F\rangle$ [94].

$$U_{OSG} = -\frac{1}{2\epsilon_0 c} I(r) \left(\alpha^S(\lambda) + \frac{i\alpha^V(\lambda)}{F} [\mathbf{u}^* \times \mathbf{u}] \cdot \mathbf{F} + \frac{\alpha^T(\lambda)}{2F(2F-1)} \left(3\{\mathbf{u}\cdot\mathbf{F}, \mathbf{u}^*\cdot\mathbf{F}\} - 2F(F+1)\right) \right) \tag{5.2}$$

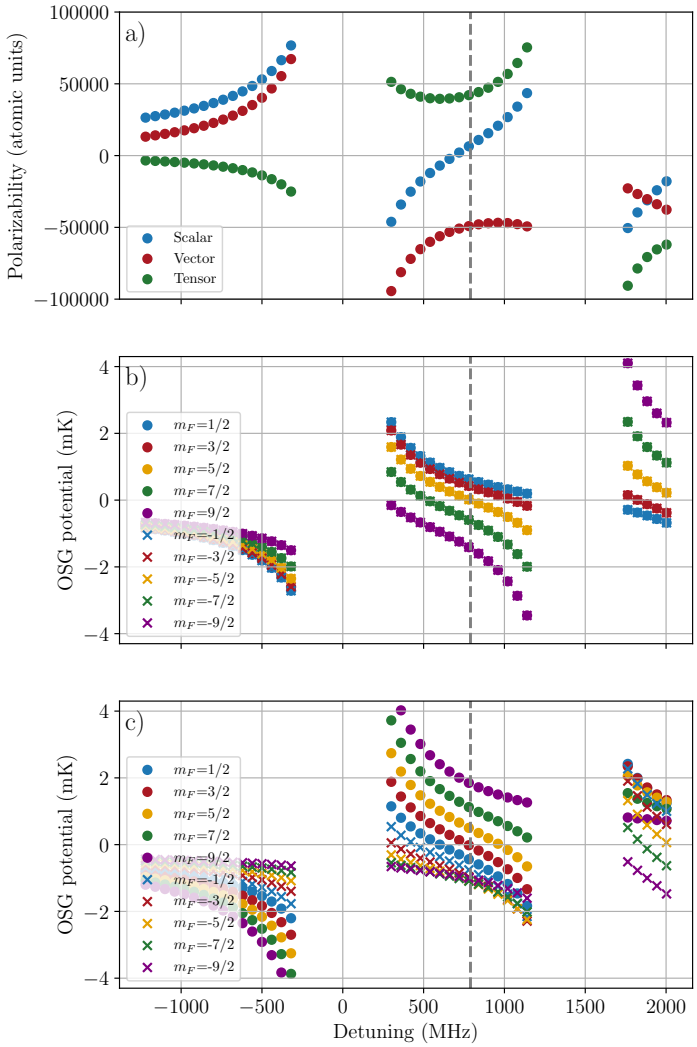

FIGURE 5.9: Polarizabilities and OSG potential. a) Scalar, vector and tensor polarizabilities of the $^1S_0$ ground state in ^{87}Sr as function of the OSG beam detuning from the $F = 11/2$ state. For a detuning in between the $F = 11/2$ and $F = 9/2$ transition, the scalar polarizability vanishes giving rise to a purely spin-dependent OSG potential. b) OSG potential for a 3.25 mW beam with $w = 4.0\,\mu$m as function of detuning for linear polarization creating the same potential for m_F and $-m_F$ states. c) OSG potential for the same beam parameters but with circular polarization creating a fully m_F dependent potential but with reduced separation capability for one half of the spin manifold.

where $\{\cdot,\cdot\}$ denotes the anticommutator and $[\mathbf{u}^* \times \mathbf{u}]$ is the cross-product of the light polarization vector $\mathbf{u}$. The resulting optical potential decomposes into a scalar $\alpha^S_{nJF}(\lambda)$, a vector $\alpha^V_{nJF}(\lambda)$, and a tensor $\alpha^T_{nJF}(\lambda)$ part. Their contributions depend on the orientation of the light field polarization $\mathbf{u}$, and the total angular momentum of the atom $\mathbf{F}$ with respect to the quantization axis. The potential shape is essentially given by the intensity distribution $I(r)$. The atom-specific polarizability components depend on the coupling of the light field with wavelength λ to the internal atomic states and are calculated for strontium in Appendix B.

By choosing the polarization of the light, we can select the number of separated spin states. Circularly polarized light creates a fully m_F-dependent potential, enabling full $N = 10$ spin separation. Linear polarization, on the other hand, causes the vector part to vanish, and the potential then depends on $(m_F)^2$, reducing the number of distinguishable spin states from 10 to 5. It is important to avoid a superposition of linear and circular components, as this can drive Raman transitions within the ground state spin manifold. These transitions can alter the initial spin state and prohibit the deterministic assignment of the initial spin. Although the OSG beam will be several linewidth detuned for the $^3P_1$ state, its intensity is high enough to provide a significant driving strength.

In addition to the polarization, the detuning from the $^3P_1$ transition affects the three light-shift components and thus determines the relative strength of the spin-dependent potential components. Generally, the influence of the vector and tensor parts becomes negligible at large detunings. Only the scalar component contributes, which makes the light shift polarization-independent and uniform across the ground state spin states. On the contrary, as shown in figure 5.9 a), in between the $F = 11/2$ and $F = 9/2$ the scalar polarizability cancels out. A vanishing scalar light shift results in a pure spin-dependent potential without a scalar-potential offset. It is advantageous to work in this regime, as the spin-dependent force should only change the velocity distribution of the atoms as much as necessary to detect a separation and not unnecessarily accelerate the atoms.

In order to find the optimal detuning and polarization state, we compare the total light shift and resulting OSG potential of a linear and circular polarized OSG beam with 3.25 mW power and 4 μm waist in figure 5.9 b) and c). Our goal is to maximize the difference of OSG potentials between neighboring m_F states, which directly translates into a measure for the separation distance after the expansion time. The larger the separation, the easier it will be to resolve the m_F states. For circular polarization, always one-half of the spin manifold is minimally resolved. For that reason, we use a tensor potential rather than a vector potential. We accept a reduced separation performance in terms of the number of m_F-states but gain in separation distance between the remaining 5 $|m_F|$-states to have enough spin assignment fidelity and resolution for our proof of concept experiment. As a technically possible offset lock frequency, we choose +790 MHz detuning. This detuning is as close as possible to 700 MHz to achieve a vanishing scalar light shift.

With a chosen detuning, we can now estimate the effect of off-resonant driving on the 689 nm transition. Although we avoid Raman transitions by setting a pure linear polarization, the high intensity and close detuning within the hyperfine manifold of the $^3P_1$ state still cause a mixing of the $^1S_0$ and $^3P_1$ states. State mixing reduces the effective OSG potential as the light shift for a ground state and the excited state have opposite signs. Additionally, the state mixing turns the assumption of a static OSG potential into a position and time-dependent potential. As the atom is accelerated along the OSG potential, the intensity and state mixing change, and hence the OSG potential. However, the lowest energy dressed state contains at most 4 % of $^3P_1$ contribution and state mixing therefore has negligible contribution to the OSG process when the OSG pulse is shorter than the lifetime of the $^3P_1$ state.

In contrast to off-resonant driving, off-resonant scattering is more detrimental for the spin detection since it can cause detection errors in the spin separation. If the atom is excited and scatters back into a different spin state where the spin-dependent force is different, the total spin separation process does not reflect the initial spin state and distorts the measurement outcome. Scattering is mitigated by limiting the OSG pulse duration. The duration should be shorter than the lifetime of the $^3P_1$ excited state of 21.5 μs to minimize off-resonant scattering. Further separation distance is created by increasing the expansion time.

The resulting OSG potential with the chosen settings is illustrated in figure 5.10. At our chosen detuning of +790 MHz detuning, the resulting potential mostly depends on the tensor light shift. As a result, we get the $|m_F| = 5/2$ state, which is nearly not affected in the separation process, whereas half of the remaining 4 states are moved in one direction and the other two states in the other direction.

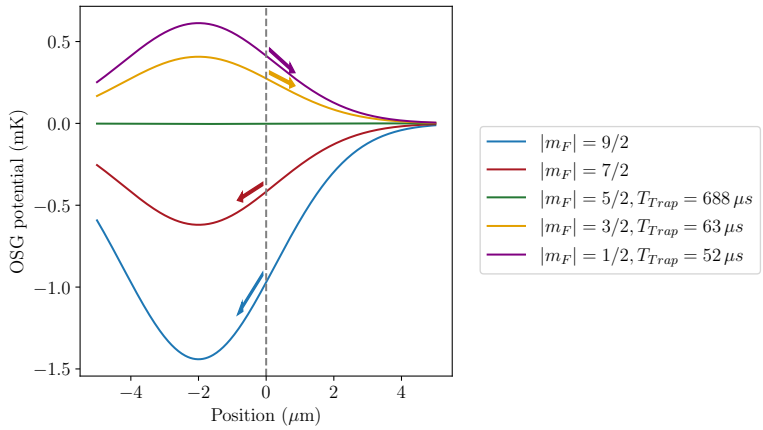

FIGURE 5.10: OSG potential for the chosen beam parameters of 3.25 mW, $w = 4.0\,\mu$m, linear polarization and +790 MHz detuning as function of the $|m_F|$ state. The OSG potential beam is displaced by half its waist from the tweezer position (gray line). Associated with the attractive OSG potentials is a trapping frequency. The OSG beam application time of a few μs is always smaller than the trap period T_{Trap} to avoid the exploration of the potential shape.

The choice of beam parameters and the resulting OSG potentials have further implications for the optimal duration of the OSG beam application. These implications stem from the beam shape and the associated curvature of the potential. The curvature of the potential influences how the spatial distribution of the atoms evolves during expansion. Generally, the curvature of a circular OSG beam causes a symmetric spread of the atomic distribution around its position. However, in comparison to a linear potential gradient and linear evolution of the initial momentum spread, a finite evolution time in a harmonic potential significantly modifies the symmetric spatial distribution before the expansion and final imaging. This effect can be denoted as the lensing effect of a harmonic potential and is most apparent for an attractive potential in which the atoms oscillate with the trapping frequency and trapping period T_{Trap}. For example, at $T_{Trap}/4$, the atom's initial position is translated into maximal momentum. On the other side, for $3 \times T_{Trap}/4$, the momentum direction of the atom is reversed. This effect is even worse when considering that the assumed harmonic potential is just an approximation of the true Gaussian-shaped OSG potential.

In figure 5.10, we report the associated oscillation period for each OSG potential. To minimize the lensing effect, we keep the application time below the smallest trapping period and therefore limit the OSG application time to $5\,\mu$s. This choice of OSG time approximates the OSG potential as close to a linear potential as possible and avoids a substantial evolution in the Gaussian OSG potential. The defined settings of the OSG beam are characterized as presented in the next section.

5.2.2 OSG beam characterization

The characterization of the OSG beam is essential for understanding the atom dynamics in presence of this optical potential. The detuning of the OSG beam is fully determined

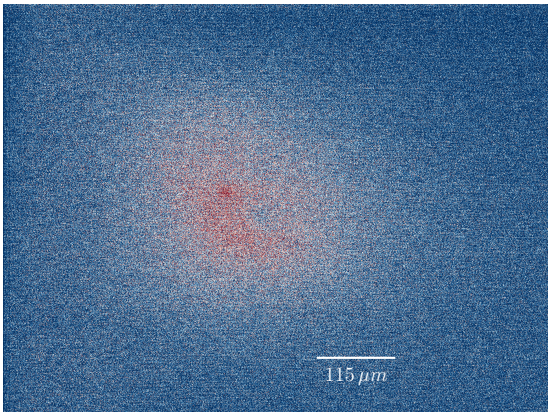

FIGURE 5.11: OSG beam alignment. A repulsive OSG beam is aligned to the tweezer position by imaging the atom response in the red MOT with the Manta1 imaging system.

by the offset lock to the red MOT laser. Measuring the less obvious beam characteristics, such as alignment, polarization, and beam size, is done by measuring the response of the atoms to the applied OSG potential.

Due to the experimental ease of ^{88}Sr and its simpler transition structure to the $^3P_1$ state, we use ^{88}Sr atoms throughout the OSG beam characterization. The characterization of the OSG beam starts with the alignment to the atoms by shining the OSG beam within the red MOT. Figure 5.11 shows the ^{88}Sr red MOT imaged with the Manta1 setup. The image shows the increase in density due to the tweezer beam. Next to it is a reduced density spot created by the OSG beam, which was switched on for 1 ms prior to the imaging. The OSG beam is 100 MHz blue detuned to the $^3P_1$ transition, making the OSG beam repulsive. This situation allows us to precisely move the OSG beam on top of the tweezer spot.

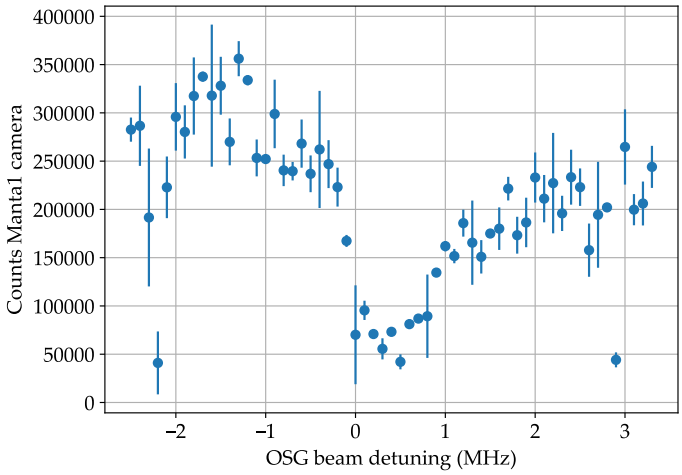

FIGURE 5.12: Polarization optimization of OSG beam. The required linear polarization is characterized by performing spectroscopy on the $^3P_1$ $F = 1$ transition of free-space atoms released from the reservoir dipole trap. For the three possible transitions in ^{88}Sr, the centered π-transition is the most dominant transition indicating dominant linear polarization of the OSG beam.

With the OSG beam overlapped with the tweezer, we perform spectroscopy on the $^3P_1$ transition to set a clean linear polarization of the OSG beam. The measurement is analogous to the polarization characterization of the pumping beam in section 4.1. Figure 5.12

shows the atom blowout signal after applying the OSG beam on resonance for 2 ms of a free-falling ^{88}Sr cloud. A guiding field of 1.2 G is applied to separate the σ transitions from the π-transition. After optimizing the guiding field direction to the OSG beam alignment and its polarization state, we get a strong suppression of the σ-transition component in comparison to the strong π-transition.

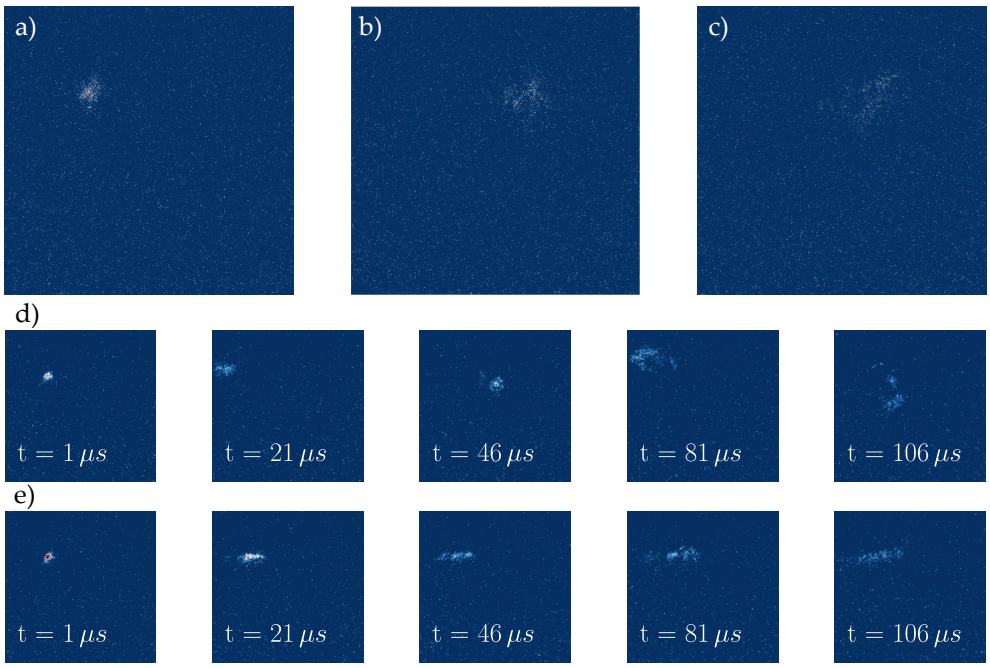

FIGURE 5.13: Alignment of OSG potential gradient. a) A cloud of ^{88}Sr atoms is released from the tweezer and imaged with free-space imaging after 300 μs of TOF b) For a 10 μs flash of a repulsive OSG beam after the release, the atom cloud is kicked stronger the closer the OSG beam is displaced from the tweezer. At a OSG beam displacement of half its waist, the kick is maximized. c) If the OSG beam is moved too close to the tweezer beam, the atom cloud spread drastically increases and eventually the kick distance is reduced. d) from left to right: Trajectory of the atom cloud after 300 μs of TOF for various application times of an attractive OSG beam. For non-optimal position of the OSG focus with respect to the tweezer focus, the trajectory becomes twisted. e) from left to right: For an optimized OSG beam focal position, the trajectory shows the fastest harmonic oscillations in horizontal direction.

Next, we slightly displaced the OSG beam from the tweezer position and set a 100 MHz blue detuning again. Observing the kick of a cloud of atoms released from the tweezer trap aligns the OSG potential gradient onto the atom position. This displacement causes the atom cloud, released from the tweezer trap, to experience a kick along the potential gradient, allowing us to align the OSG potential gradient with the atomic position. First, we switch off the tweezer, switch on the OSG beam for up to 10 μs, and image the position of the atom cloud after a TOF time of up to 300 μs using our free-space imaging technique. Figure 5.13 shows a collection of displaced atom clouds. As we move the beam closer to the tweezer position (figure 5.13 a)) the displacement increases accordingly (figure 5.13 b)). When moving even closer to the tweezer position, the cloud size drastically increases and is fragmented (figure 5.13 2c)). We selected the OSG beam position to maximize the observed kick. At this optimal position, the OSG beam is displaced by approximately half a waist from the atom location, where the steepest potential gradient exists. The OSG

beam can be precisely positioned and aligned in any desired direction to control the kick accordingly.

The essential OSG beam characteristic is its intensity, which we infer from trapping frequency measurements of the resulting light potential. To do that, we tune the OSG beam to the red of the 689 nm transition by 500 MHz and release a ^{88}Sr cloud from the tweezer trap into the off-centered attractive OSG potential. The cloud oscillates in the OSG potential, and its time-dependent position is imaged after some TOF time [90]. Figure 5.13 d) shows a collection of the atom cloud evolution after 300 μs TOF and variable OSG beam application time of $1 - 100\,\mu$s.

The atom cloud evolution is also used to align the OSG beam focus to the tweezer focus and obtain a maximal trapping frequency. Due to a non-achromatic objective, the focal point of the OSG beam and the tweezer beam do not coincide. We can slightly change the focal point of the OSG beam by moving the last lens of the 1:1 telescope before the objective (Setup 2.5.5). As we move the focal point towards the optimal position, the trajectories of the atom clouds for longer OSG beam application speed up, and the trajectories become less twisted. In the focus, the beam quality is normally the best, which is apparent when comparing figure 5.13 e) with figure 5.13 d).

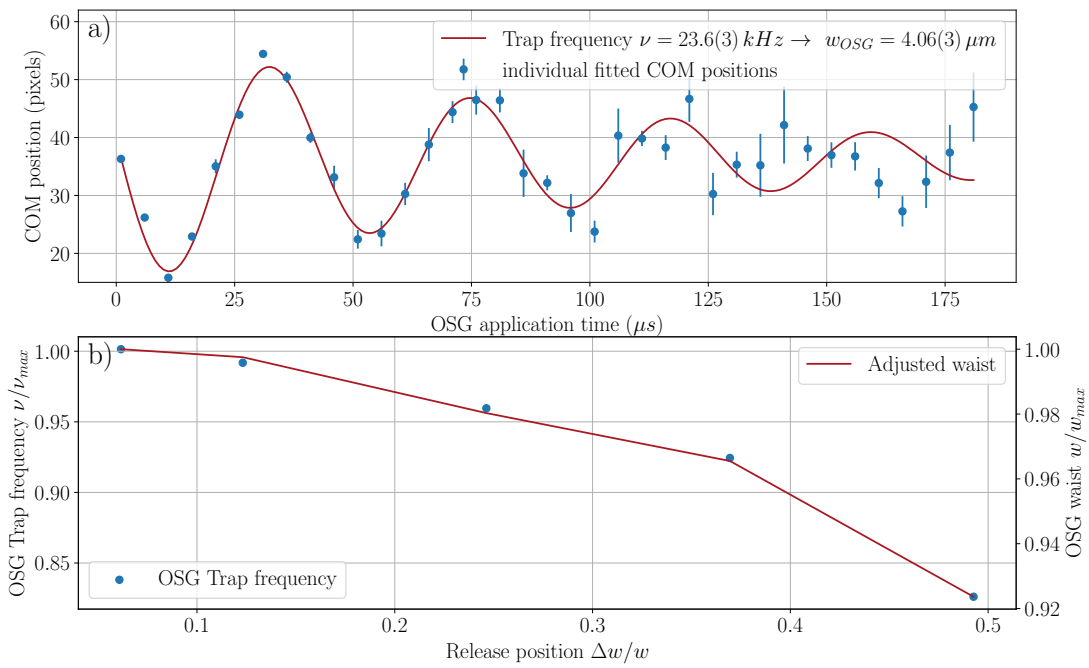

FIGURE 5.14: OSG beam waist from trap frequency measurement. a) The center of mass position (COM) of the atomic cloud as function of the OSG application time for a 2.76 mW OSG beam detuned by $\Delta = -500$ MHz from the 689 nm transition. A fit of the oscillation yields a trapping frequency of 23.6(3) kHz, which is translated into a beam waist of 4.06(3) μm. b) The trapping frequency is simulated for different release points of the atom cloud into the Gaussian shaped OSG beam. The second y-axis gives the necessary adjustment of the OSG beam waist to be compatible with the measured trap frequency of 23.6 kHz.

For an optimized alignment, we determine the final beam shape by measuring the trap frequency of the attractive OSG potential. The trap frequency can be determined by tracking the center of mass position of the atom cloud as a function of the OSG application time. A fit of the data with a decaying harmonic oscillation reveals a trapping frequency of 23.6(3) kHz in figure 5.14 a). Next, the trapping frequency is translated into a beam waist by comparing it to the light shift calculations in Appendix B at the used 2.76 mW of beam

power. Thanks to the single ground state of ^{88}Sr, the light shift simplifies to the scalar light shift that is induced by the OSG beam with a beam waist of 4.06(3) μm.

The determined OSG beam waist of 4.09 μm is an upper limit. The beam waist measurement has an uncertainty given by the displacement of the OSG beam with respect to the tweezer position. Technically, the OSG beam is only at its center well-approximated by a harmonic trap and has actually a Gaussian trap shape. The oscillations are influenced by the release point in the OSG potential. Although we have a procedure to optimize the OSG beam position around the displacement of halve the OSG beam waist, we can not accurately measure the displacement. To clarify the OSG beam displacement, we perform simulations of the evolution of a wavepacket inside a Gaussian trap based on the 1D Schroedinger equation. We assume a wavepacket given by the ground state of the tweezer trap and let it evolve inside the Gaussian OSG trap at different displacements from the trap center. The corresponding trap frequency of the center of mass evolution is plotted as a function of the release point in figure 5.14 b). For a release point shift of half the beam waist, we have to adjust the corresponding beam waist downwards by 8 %, which results in a smaller beam waist of 3.75 μm. Therefore, we adjust the measured OSG beam waist with a larger uncertainty of $w_{OSG} = 4.0(2)$ μm.

5.3 Spin resolution

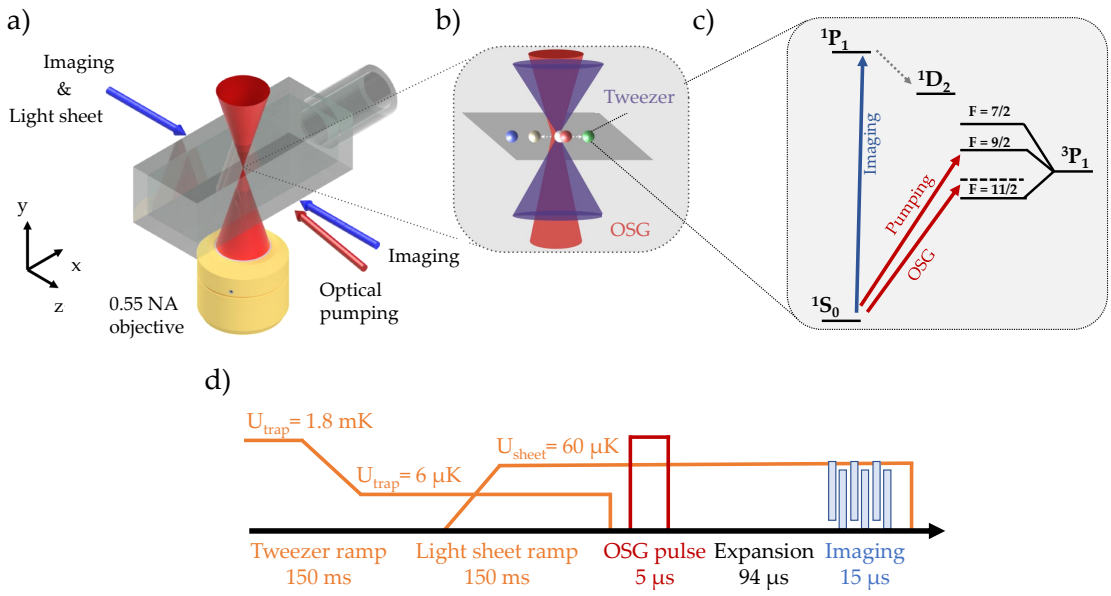

FIGURE 5.15: Experiment overview of the spin-resolved imaging with ^{87}Sr atoms. a) The experimental setup consists of the tweezer, the OSG beam, counter-propagating free-space imaging beams, an optical pumping beam and the 1040 nm reservoir dipole trap forming a light sheet. b) A nuclear spin-dependent force is created by flashing the linearly polarized optical Stern-Gerlach beam with a displaced center from the optical tweezer in the atomic plane. A subsequent free planar evolution in the light sheet dipole trap at the focus of the objective allows to infer the atomic spin from the atom position. c) Free-space imaging is performed on the blue transition and the optical Stern-Gerlach beam operates +790 MHz detuned from the red $F = 11/2$ intercombination transition. In order to initialize ground state atoms in the nuclear spin state $m_F = +9/2$, optical pumping is performed using the σ^+ polarized cooling beam tuned on resonance to the $F = 9/2$ transition. d) Typical spin separation sequence.

This section describes the combined use of free-space imaging and the OSG separation technique for spin-resolved single-atom detection of ^{87}Sr atoms. The working principle of our imaging technique is presented in figure 5.15. The OSG beam is directed through the objective and is displaced by half its beam waist from the tweezer beam. The focal points of both beams are vertically aligned to the 1040 nm reservoir dipole trap, which forms a light sheet. The OSG beam is detuned between the $^3P_1$ $F = 9/2$ and $^3P_1$ $F = 11/2$ state to induce spin-dependent light shifts for ground-state atoms. As a consequence, during a flash of the OSG beam after release from the tweezer beam, the atoms evolve in the spin-dependent potentials and feel a spin-dependent force. After a free evolution in the light sheet, the atoms appear at distinct positions based on their initial nuclear spin state. Additionally, we have an optional circular polarized pump beam on resonance with the $F = 9/2$ transition to optically pump the ground state spin state into either of the $m_F = \pm 9/2$ stretched states in $^1S_0$.

The spin separation procedure begins after the successful loading of the tweezer trap. Figure 5.15 d) illustrates the typical sequence of experimental steps. At the beginning, the tweezer is ramped down in 150 ms to a depth of $k_B \times 6\,\mu$K. Subsequently, the light sheet is ramped up over 150 ms to a final depth of $k_B \times 60\,\mu$K. The tweezer trap is then switched off, and an OSG pulse of 5 μs is applied. Following this, the atoms continue to move within the light sheet for 94 μs before being imaged using the free-space imaging. To obtain a random spin mixture, optical cooling with red light inside the tweezers beforehand is avoided.

The resulting experimental data consist of single-shot binarized images, as shown in Figure 5.16. These images reveal that the atoms appear at various locations within a range of 25 μm. Some atoms are observed to be displaced upward from the initial tweezer position (cross), while others are pushed downward. In order to evaluate the OSG process, the spatial locations of 3738 individual experimental realizations are evaluated. To quantify the location of the atoms, the binarized images are converted to maps of single atoms using the routine defined in 5.1.3. After low-pass filtering the binarized images, spatial maxima are identified and labeled as a single-atom position based on the free-space imaging detection threshold.

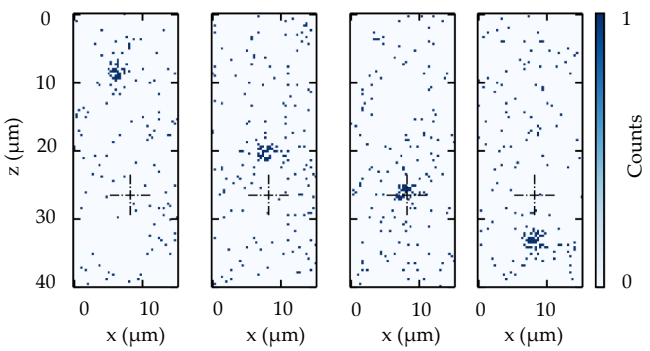

FIGURE 5.16: Spin separation experiment outcomes. Individual binarized free-space imaging shots, showing different locations of single atoms with respect to the initial tweezer position (cross).

Detection fidelity

The sum of all 3738 individual atom locations is plotted in figure 5.17 a) and shows distinct atom location clusters. Two separated location clusters are visible above the tweezer

positon, one cluster is located in close vicinity to the tweezer position and another location cluster is visible below the tweezer position. By comparing to the theoretically expected total light shift from our OSG beam setting in figure 5.9 b), we can assign a spin state to each location cluster. Since we have used the tensor light shift, the OSG potential is insensitive to the sign of each m_F state and we therefore can assign a spin value $|m_F|$ to each location. The top location is the $|m_F| = 9/2$ since it has the largest pulling force. In contrast, the $|m_F| = 5/2$ location should experience a negligible light shift and therefore shows up at the tweezer position. In between the $|m_F| = 9/2$ and $|m_F| = 5/2$ appears the $|m_F| = 7/2$ spin states. For $|m_F| = 1/2$ and $|m_F| = 3/2$ spin states that are pushed below the tweezer position, the light shift difference was not large enough to show a clear spatial separation. As a consequence, we regard this spin location as a combined area of the $|m_F| = 1/2$ and $|m_F| = 3/2$ spin states. All in all, we have successfully separated 4 out of 5 spin states of the ^{87}Sr ground state manifold neglecting the sign of the m_F states.

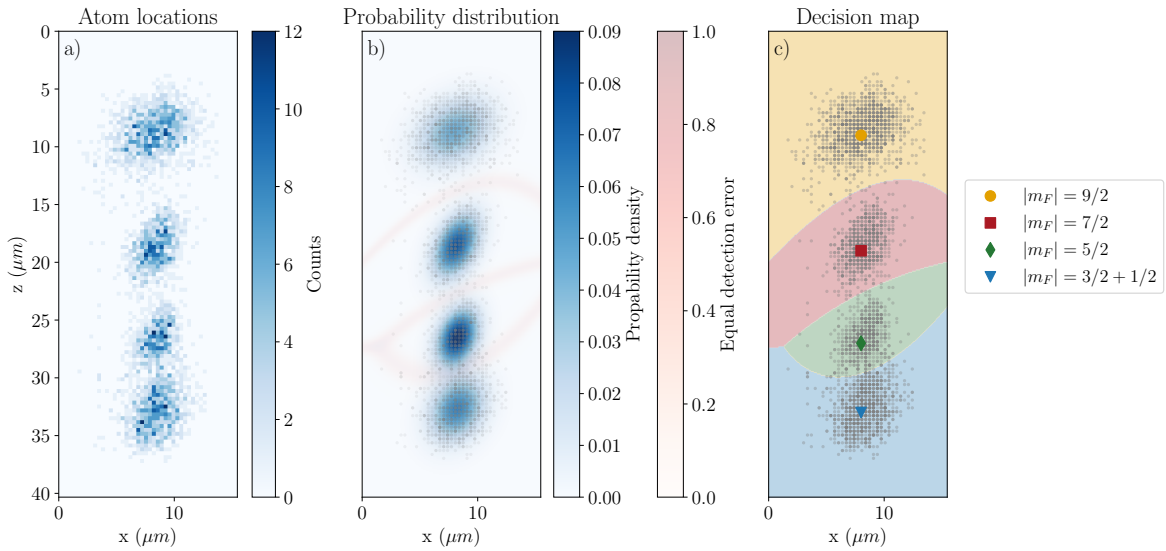

FIGURE 5.17: Spin state assignment. a) Sum of all single atom locations in 3738 experimental realizations containing an atom. b) A fit of the atom locations with a Gaussian mixture model yields 4 individual Gaussian distributions. Based on these 4 Gaussian distributions, the atom location map is divided into spin areas. The boundaries are defined at the position where the assignment to either of the neighboring distributions has an equal error. The boundary is shown in red. c) The resulting decision map of assigning a detected atom at a certain position to its correct spin value.

Next, we quantify the fidelity of a measured single atom appearing in a 15 μm$\times$40 μm area around the original tweezer position being correctly assigned to one of the 4 spin state values. We can treat the map of all atom locations as a 2D extension of a histogram. To do that, we fit to the map of all atom locations a Gaussian mixture model, consisting of a linearly weighted superposition of $k_{max} = 4$ Gaussian distributions with a mixing coefficient Π_k, a mean value $\mu_{x,k}$, $\mu_{y,k}$ and spatial spread $\sigma_{x,k}$, $\sigma_{y,k}$. The fitting parameters are estimated using the Expectation-Maximization algorithm, which iteratively adapts the fitting parameters to maximize the likelihood that the model matches the observed data [103]. From the 4-component Gaussian mixture model, the mean and spatial spread are extracted to define individual normalized probability distributions for each cluster area as show in figure 5.17 b). We define the boundaries of neighboring clusters at the position where the overlap of neighboring distributions is equal and thus the assignment error is minimized. The boundaries are shown in red in figure 5.17 b). Based on these boundaries,

the atom location map can be divided into spin areas and a resulting decision map to assign a spin state to each detected atom. The spin areas are shown as colored regions in figure 5.17 c). We obtain a detection fidelity for the choice of our decision map by calculating the overlap of each probability distribution with respect to all other distributions at the defined boundaries. The infidelity is thereby the sum of wrongly assigning a detected atom to its neighboring spin areas and wrongly assigning atoms from neighboring spin areas to a certain spin state. In the end, our measurement yields spin detection fidelities of 99.70(6) % for $|m_F| = 9/2$, 98.7(2) % for $|m_F| = 7/2$, 93.6(8) % for $|m_F| = 5/2$, and 94.6(7) % for $|m_F| = 1/2, 3/2$. The fidelities are obtained under the condition that an atom has been detected. The error on the fidelity is obtained by bootstrapping the data [95].

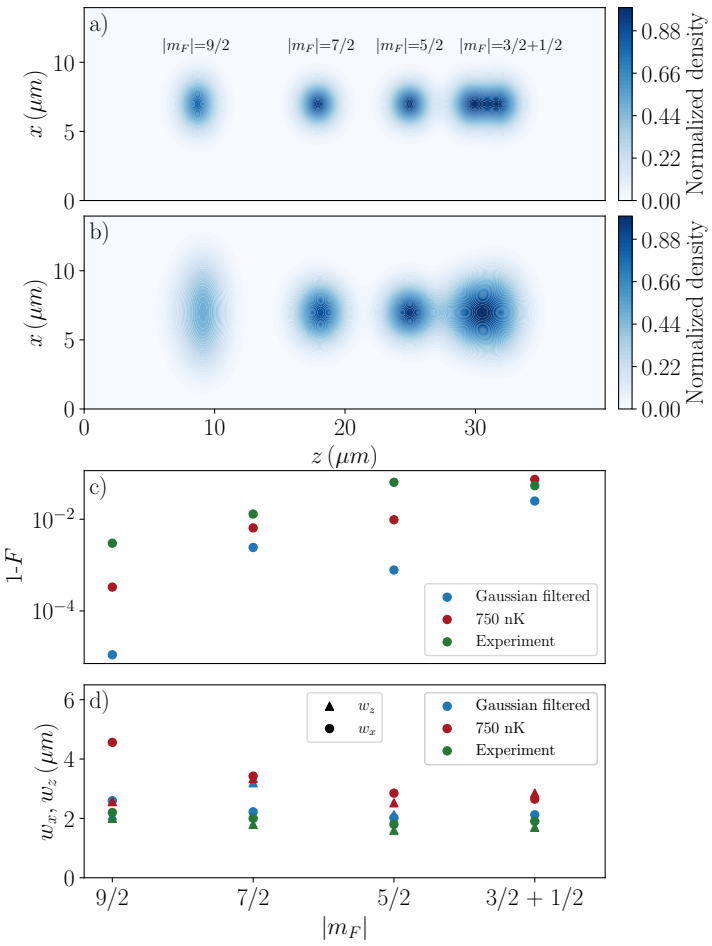

FIGURE 5.18: Simulation of the spin separation process. a) Expected atomic signal for an atom initially in the tweezer ground state after 5 μs application of the OSG potential and 94 μs free expansion. To make the results compareable to the experimental data, the simulation results are convoluted with a Gaussian kernel with the size of the free-space imaging resolution $\sigma = 1.0\,\mu\text{m} \times 1.2\,\mu\text{m}$. b) Same simulation parameters as for a) but for a thermal distribution of 50 harmonic oscillator states at 750 nK. c) Extracted spin detection fidelity by applying the 4 component Gaussian mixture model to different simulation assumptions and the experimental atom location map. d) Simulated and measured spread w_x and w_y of the fitted spin regions for different model assumptions as function of spin state $|m_F|$.

Following the spin assignment, we model the spin-separation process to determine the limiting factors of the obtained detection fidelities. The numerical simulations use the split-step method to propagate a wave function in a potential based on the 2D Schroedinger

equation [104]. As the initial wave function, we use the harmonic oscillator wave function of the final tweezer trap. Afterward, we apply the 5 different OSG potentials and a final common free-space expansion for 94 μs. The time is divided into 0.5 μs steps and space is resolved with 0.1 nm. The resulting expectation value of the wave function after the separation process is convoluted with a Gaussian kernel with the size of the free-space imaging resolution $\sigma = 1.0\,\mu\text{m} \times 1.2\,\mu\text{m}$ in order to make it comparable to the experimental results. Simulated and experimental results are visualized in figure 5.18.

Figure 5.18 a) shows the ideal situations for the ground state of the tweezer trap. The simulation matches well with the measured spin locations in figure 5.17 a) in terms of separation distance. 4 out of 5 spin regions are visible. The inclusion of our free-space imaging resolution reproduces well the merging of the $|m_F| = 1/2$ and $|m_F| = 3/2$ states into one region and is therefore one of the limiting factors in our separation process. Including a finite temperature into the separation process yields a simulated atom location distribution as shown in figure 5.18 b). This simulation takes 50 higher excited harmonic oscillator states of the 2D tweezer trap into account and overlaps the resulting wave functions according to a Boltzmann distribution at 750 nK. In comparison to 5.18 a) the simulation shows a larger spread. For the $|m_F| = 9/2$ state, the increase in spread is the strongest.

The influence of the spread on the spin detection fidelity is plotted in figure 5.18 c) where the Gaussian mixture model is applied to the simulated data. The experimental data has a comparable fidelity as the simulation data. To compare the different contributions to the spin-dependent spatial spread, figure 5.18 d) shows the extracted horizontal and vertical Gaussian widths for each spin state. The simulated width is close to the experimentally found width, where the free-space imaging resolution can be identified as the strongest contribution. For $|m_F| = 9/2$ it is striking that the finite temperature strongly adds to the vertical spread in comparison to the horizontal. All in all, the simulation reproduces the measured spin locations with near-quantitative agreement in terms of separation distance, absolute position, and spatial spread. This rough modeling therefore, provides a useful framework for understanding the current limitations of our spin-detection scheme.

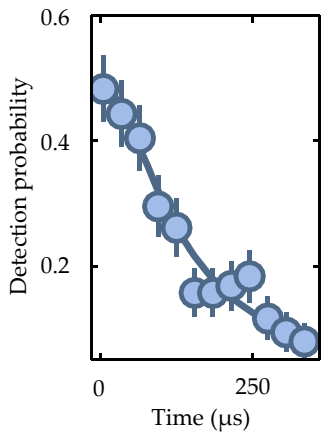

FIGURE 5.19: Release and recapture measurement for an atom temperature estimation. Probability to detect an atom as a function of release time from the tweezer trap into the light sheet trap. The solid line represents the probability based on Monte-Carlo simulations at an assumed atom temperature of 750 nK. Error bars represent one standard deviation of the mean

The assumed temperature of approximately 750 nK was experimentally determined from an independent measurement using the release and recapture method [105]. In this procedure, the probability of detecting an atom was measured after the tweezer was

switched off, without applying the OSG beam, for various expansion times. The resulting probability as a function of the release time is shown in figure 5.19. This experimental data was then compared to Monte Carlo simulations of the atom dynamics in the 2D light sheet. The decay of the probability provides information about the atoms' thermal velocity distribution, allowing for an estimation of the temperature. The error bars in the data represent the standard deviation of the measured mean probability.

Spin-polarized manifold via optical pumping

In the following section, we want to further characterize the spin-resolved imaging of single ^{87}Sr atoms by preparing a certain spin state instead of working with a sample of random spin states. For preparing a certain spin state, we perform optical pumping on the $^1S_0\, F = 9/2$ to $^3P_1\, F' = 9/2$ intercombination transition to transfer the atom from its initially random m_F state into the $m_F = 9/2$ state. Once in the $m_F = 9/2$ state, the atom is in a dark state to the pumping beam and does not scatter any further photons.

The details of the pumping sequence prior to the established spin separation and imaging sequence are visualized in figure 5.20 a). The sequence starts with switching on a guiding field of 2 G in the z-direction and along the optical pumping beam. We ramp down the tweezer to avoid scattering from the tweezer trap and light shifts on the pumping transitions. Afterward, we switch on the cooling beam with stirring light as optical pumping light for 50 ms at an intensity of $I_{pump} = 94\, I_{sat}$. Due to the guiding field and the larger Zeeman splitting of 2.1 MHz/G/m_F, the pumping beam is modulated over a span of 6 MHz to reach every m_F state in the tilted spin manifold of $^3P_1\, F' = 9/2$. Likewise, we can optically pump to $m_F = -9/2$ by reversing the guiding field direction.

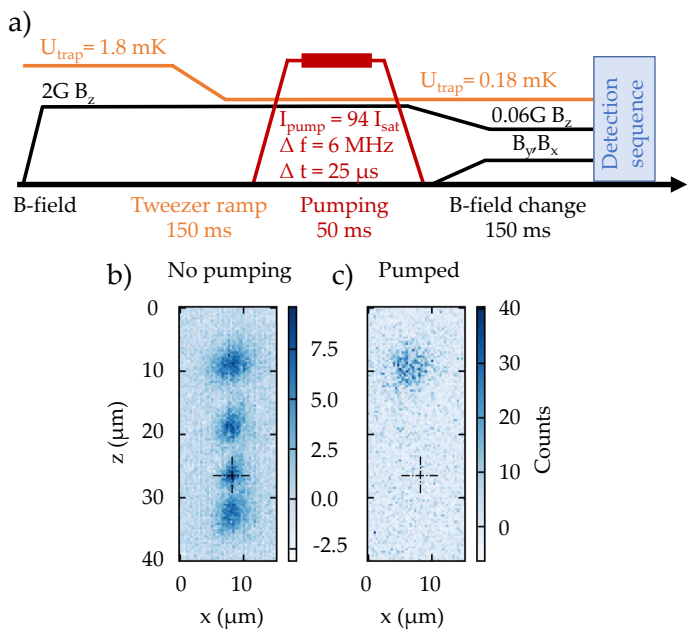

FIGURE 5.20: Optical pumping to stretched state $m_F = 9/2$. a) Experiment steps to optically pump ^{87}Sr atoms to the stretched $m_F = 9/2$ or $m_F = -9/2$ state prior to spin resolved imaging. b) Average fluorescence image of pumped and non pumped atoms, justifying the $|m_F| = 9/2$ assignment of the top spin cluster.

After pumping, it is important to precisely align the initial quantization axis during pumping with the subsequent quantization axis of the OSG beam. This is done by adiabatically rotating the guiding field axis to align it with the polarization axis of the OSG beam. Afterward, the spin-resolved imaging sequence is applied. The resulting averaged fluorescence picture changes from displaying four spin regions in figure 5.20 b) to only one top spin region in figure 5.20 c) when optically pumped to $m_F = 9/2$. The fidelity of measuring only the top $m_F = 9/2$ region is 94(2) %. The detected spin-polarized manifold allows two conclusions about the OSG technique. First, the pumping and detection of the top spin region experimentally justifies the spin assignment. Second, up to the pumping preparation fidelity, the data shows no spin-changing processes, meaning the OSG spin separation indeed preserves the original spin state of the atom. It shows the potential applicability of imaging a priori unknown spin configurations of single atoms.

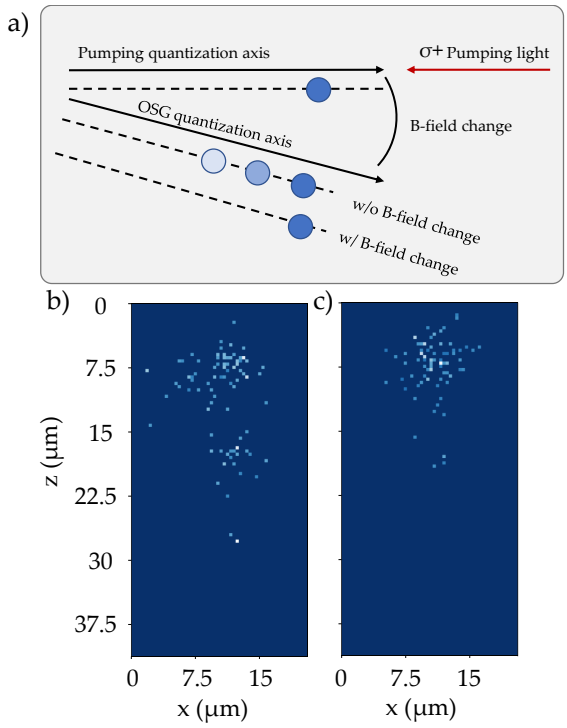

FIGURE 5.21: Optimization of stretched state detection. a) For the correct interpretation of the imaged spin-polarized manifold, the magnetic quantization axis during the optical pumping process and the OSG detection basis must be aligned. The alignment is precisely done by adjusting the compensation fields after the optical pumping and before the OSG separation sequence. b) Non-optimal stretched state measurement showing a projection of the stretched state on to other spin states. c) Optimized pumping and detection showing the single $m_F = 9/2$ spin cluster with 94(2) % fidelity.

In the end, the alignment of the pumping quantization axis and polarization of the OSG beam was crucial for a successful detection of the spin-polarized manifold. A small difference between the two axes without the adiabatic alignment drastically reduced the fidelity of only detecting the $m_F = 9/2$ spin region. The problem is visualized in figure 5.21 a). Figure 5.21 b) shows the detection outcome before the optimization in comparison to figure 5.21 c) after the optimization. Ultimately, the polarization of the OSG beam determines the quantization axis since the measurement basis of 4 different spin regions is only defined along its linear polarization axis. Every process beforehand has to be referenced to this measurement axis. If the quantization axis during optical pumping is not

aligned to the measurement axis, then the prepared state is ultimately projected onto the measurement basis and shows contributions from all four basis states.

Application: Coherent nuclear spin dynamics

Given that we can measure the $|m_F|$ spin value with our spin-resolved imaging technique and deterministically prepare the $m_F = 9/2$ state, it allows us to perform manipulations of the nuclear spin state at the single-atom level. More specifically, we measure the coherent dynamics of the nuclear spin after a magnetic field quench.

The underlying experimental sequence is visualized in figure 5.22 a). First, an atom is optically pumped into the stretched $m_F = 9/2$ state. The spin orientation axis is aligned to the axis of the spin separation process as discussed before and is denoted with the z-axis. Then, the compensation coils create a sudden 1.158 G magnetic field applied for a variable application time. The quench field is directed in y-direction, which is nearly perpendicular to the spin orientation of the subsequent spin separation process in z-direction.

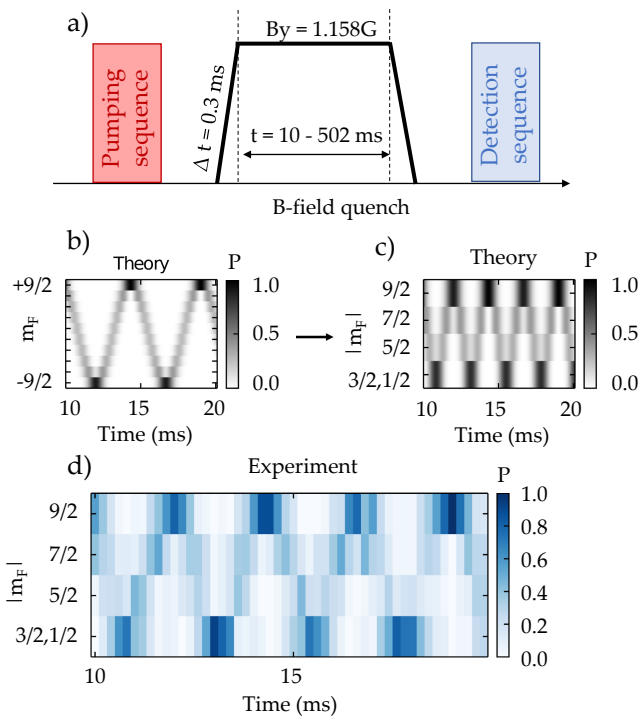

FIGURE 5.22: Coherent spin dynamics after a magnetic field quench. a) The quench dynamics sequence consists of the initialization in $m_F = 9/2$ with a guiding field in z-direction, switch on of 1.158 G guiding field in y-direction for a variable time and finally the spin detection. b) Numerical simulation of the coherent spin evolution of a spin-9/2 system under the near-transversal quench field. c) Projection of the numerical simulation on to our detection method that is only sensitive to $|m_F|$. d) Experimentally measured time evolution of the $|m_F|$ populations.

This experimental setup resembles the coherent Larmor precession with spin-9/2 atoms and can be numerically simulated as shown in figure 5.22 b). The field quench induces the nuclear spin to evolve coherently with the Hamiltonian

$$H_{Quench} = \mu \mathbf{F} \cdot \mathbf{B}, \tag{5.3}$$

where μ is the magnetic moment of the nuclear spin, $\mathbf{B}$ the quench magnetic field and $\mathbf{F}$ a spin-9/2 operator. After a variable evolution time, the populations in different m_F states

are determined. Figure 5.22 c) shows how the population evolution would look with our spin detection method that is only sensitive to $|m_F|$. Figure 5.22 d) shows the measured population evolution.

For comparing theory with the experimental outcome, we plot the individual population evolution as a function of the quench time in figure 5.23. The oscillations exhibit a large contrast, with no visible decay for up to 500 ms. Since the applied magnetic field is tilted by the constantly present small guiding field of 80 mG for the subsequent imaging process, the remaining contrast oscillations with additional frequency components stem from the non-perfect transverse direction of the quench field. Taking both fields into account and assuming an exponential switching time of 0.3 ms in good agreement with independent measurement of the magnetic field rise time, the magnetic field quench accurately fits the experimental data. The most significant noise source lies in the accuracy and stability of the magnetic fields. Both the guiding field and the quench field were independently calibrated within 5 mG via spectroscopy on the red transition in ^{88}Sr. Since the quench field is limited by the allowed current in the compensation fields, the initial guiding field had to be the small default 80 mG in z-direction, which is more prone to stray magnetic field variations or other temporal drifts. Changes in the initial guiding field not only affect the quench dynamics but also affect the detection by changing the angle between the initial quantization basis and the detection basis provided by the OSG beam. As we have noted during the optimization of the optical pumping, a correct alignment of the initialization basis and detection axis is important for high-fidelity detection.

All in all, the results demonstrate the ability to coherently control and observe long-time highly coherent nuclear spin dynamics and highlight the robustness of the nuclear spin in ^{87}Sr to external noise sources.

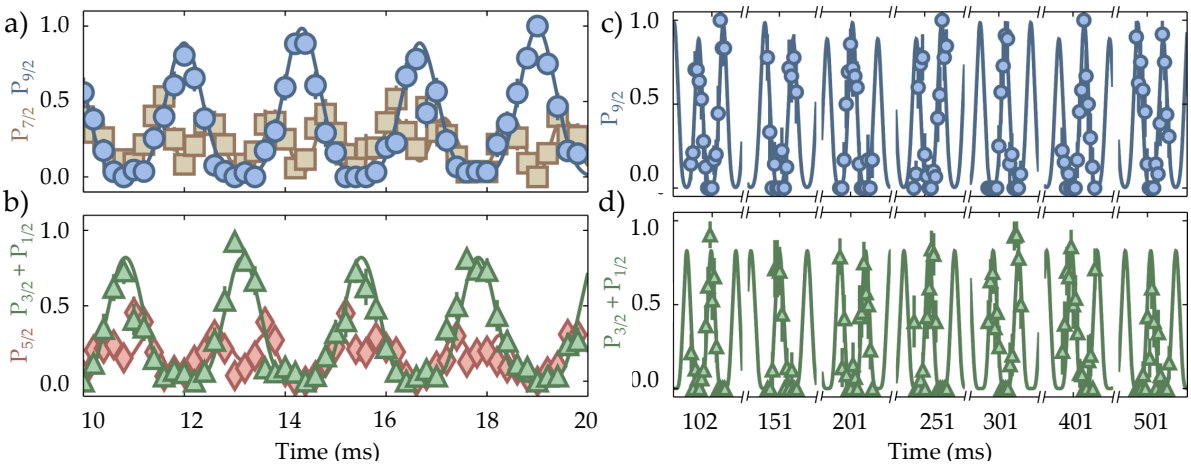

FIGURE 5.23: Coherent spin dynamics after a quench. a) Time evolutions of the $|m_F| = 9/2$ (blue dots), $|m_F| = 7/2$ (yellow squares) and b) $|m_F| = 5/2$ (red diamonds), $|m_F| = 3/2, 1/2$ (green triangles) populations and theory expectations (solid lines). Error bars represent one standard deviation of the mean. c) Long time population dynamics for $|m_F| = 9/2$ (blue dots) and d) $|m_F| = 3/2, 1/2$ (green triangles) and theory expectations (solid lines), showing a long coherence time.

5.4 Possible improvements

The key to increasing the number of resolved spin states and their detection fidelity is minimizing the spatial spread after the separation process. An obvious approach to improving

the spin-resolved imaging is increasing the separation distance by setting a longer free expansion time. However, for a possible application of the spin-resolved imaging to lattice experiments, it is particularly important to preserve the minimal distance between different spin states and rather minimize the product of separation distance and spread while maintaining a constant detection fidelity. This goal can be achieved by lowering both the temperature and the imaging-induced spread. Since our separation process simulations fit well with the experimental data, we present in this section possible improvements and their limitations for the spin-resolved imaging.

One primary contribution to the spread is the duration of the imaging process. The spread originating from the imaging process can only be reduced by decreasing the imaging time. With a more optimized imaging system, which has an objective with a transmission efficiency closer to the requested 90 % and optimized dichroic optics, we could double the number of captured photons. This enhancement would allow us to halve the current imaging time, leading to a smaller spatial spread of around 0.6 μm, according to figure 5.7 b). Assuming the improved imaging spread and our measured temperature of 750 nK would give a spin separation as shown by the simulation in figure 5.24. The detection fidelity of the initially more separated spin states significantly improves, whereas the spin states $|m_F| = 1/2$ and $|m_F| = 3/2$ can still not be resolved. The simulation outcomes indicate a detection infidelity of 6×10^{-6} for the $|m_F| = 9/2$ state, 1×10^{-3} for the $|m_F| = 7/2$ state, and 2.6×10^{-2} for the $|m_F| = 5/2$ as well as for the combined state $|m_F| = 1/2 + 3/2$.

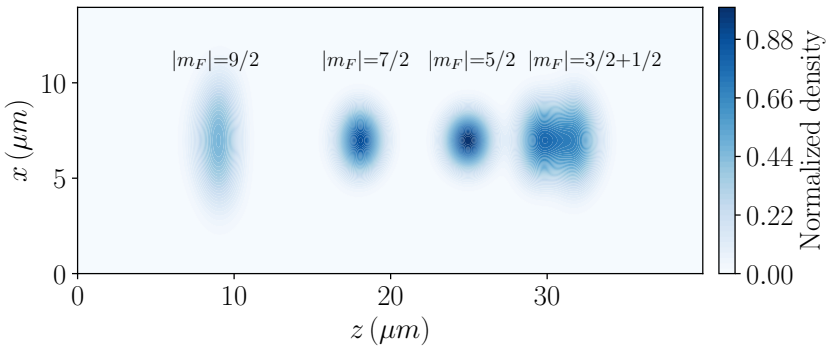

FIGURE 5.24: Simulated spin separation with improved imaging resolution. Simulation of the spin separation with 5 μs application time and 94 μs of free expansion. The simulation is convoluted with the imaging resolution of 0.6 μm$\times$0.6 μm for an optimized imaging time of 6 μs instead of 15 μs.

Even with a minimal imaging time, the simulations show that full separation of the 5 accessible spin states in our experimental setup is now limited by temperature. In our experiment, we have two possibilities to reduce the temperature.

The first approach is the single atom approach with an active cooling inside the tweezer trap, which has been investigated in chapter 4. Our Sisyphus cooling might not reach the lowest temperatures. However, cooling close to the ground state with sideband resolved cooling has been demonstrated for ^{88}Sr atoms [106] and also for ^{87}Sr atoms [107]. A ground state fraction of around $n = 0.75$ has been achieved. A disadvantage of the active cooling is the parity projection to 1 or 0 atoms and the optical pumping to the stretched state, where a closed cooling transition is possible. However, with our magnetic field quench and coherent spin evolution, we would still be able to prepare and characterize every other spin state of the full spin manifold.

Alternatively, the temperature can be reduced by evaporatively cooling a sample of tweezer-trapped atoms. The number of atoms can eventually be controlled by controlling the final tweezer depth and spilling atoms out of the trap one by one, as demonstrated in [108]. This approach presupposes we optimize the experiment for large atom numbers in the dipole trap and evaporative cooling instead of single-atom preparation as described so far.

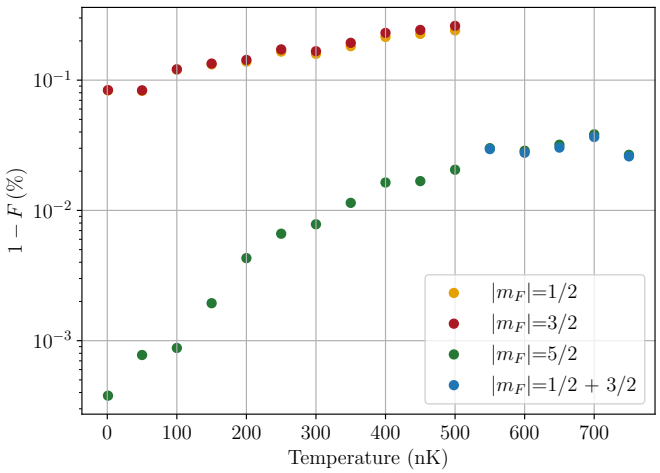

FIGURE 5.25: Simulated spin separation fidelity as function of the temperature for the least separated spin states $|m_F| = 1/2$,$|m_F| = 3/2$ and $|m_F| = 5/2$. The OSG beam is applied for 5 μs and 94 μs of free expansion. The simulations are convoluted with the optimal free-space resolution before the application of the Gaussian mixture model. For low enough temperatures the spin assignment allows 5 different spin areas, otherwise the two closest spin states $|m_F| = 1/2$ and $|m_F| = 3/2$ are combined to $|m_F| = 1/2 + 3/2$.

Both approaches would bring the temperature low enough to see a further increase in separation resolution. In figure 5.25 we simulate the detection infidelity of the three closest spin states $|m_F| = 5/2, 3/2$ and $1/2$ as a function of the temperature. The final trap depth is the lowest achievable tweezer trap depth $k_B \times 6\,\mu$K. For the imaging spread, we assume the best case of 0.6 μm. The simulation shows that below 500 nK the $|m_F| = 1/2$ and $|m_F| = 3/2$ start to separate and can reliability be resolved. The detection infidelity for the other states strongly decreases with lower temperature.

All in all, the simulations show that an optimization of the free-space imaging time and imaging spread, as well as cooling the atom towards the ground state of the trap, is crucial for advancing the detection capabilities and fidelity.

Towards SU(N>4) resolution

Next, we numerically explore whether alternative experimental settings could resolve the full $N = 10$ spin manifold of ^{87}Sr and pave the way towards resolving SU(N) physics phenomena.

In a first step, we transform the OSG potential from a tensor potential to a vector potential by changing the polarization of the OSG beam to circular. In the second step, we consider the application of two OSG beams sequentially. Previous OSG beam considerations (figure 5.9 b)) indicate that only one half of the spin manifold can sufficiently be lightshifted with a single circularly polarized beam. Therefore, the proposed separation process requires a sequence of two consecutive OSG pulses with two different OSG beams. The two beams have opposite circular polarization and opposite detuning with respect to the $^3P_1$ $F = 11/2$ resonance. The position of both beams is considered to be the same and thus does not require an extension of the optical setup and alignment procedure. The light for the full sequence can still be derived from the same light source with suitable polarization optics and a suitable AOM setup for the timing and frequency control. As a first step in the sequence, one beam switches on, and the positive m_F states are displaced according to the first OSG potential. The stretched state is accelerated the furthest, while the negative m_F states remain almost stationary due to the reduced OSG potential. After the typical OSG time, the second beam switches on and accelerates the opposite spin states in the opposite direction. Additionally, this approach results in a more equal spacing between all spin states to avoid a concentration of multiple spin states in a certain region, as it has been the case for the $m_F = 5/2, 3/2$, and $1/2$ states in our experiment. Figure 5.26 shows the expected OSG potential depth for both beam configurations as function of the detuning.

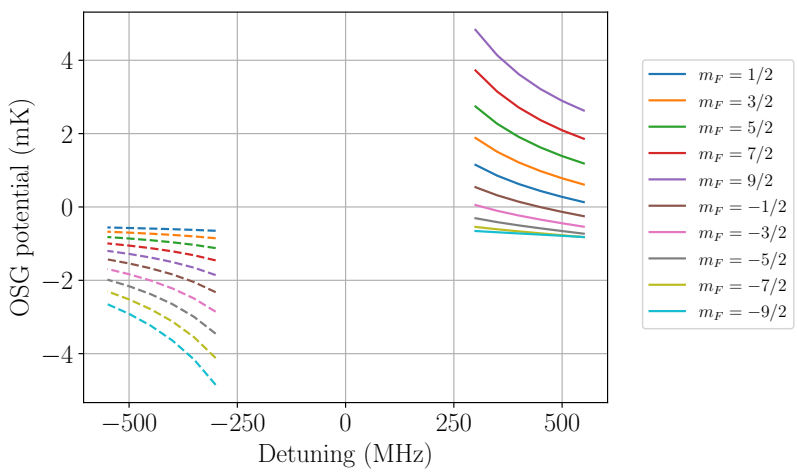

FIGURE 5.26: OSG potentials to resolve the full nuclear spin manifold using a vector light shift. The dashed OSG potential curves are created with a circular OSG beam red detuned to the $F = 11/2$ transition. The solid OSG potential curves are created with a second beam with opposite circular polarization and blue detuning. The beams are sequentially applied to separate the full spin manifold.

To investigate the feasibility of spatially resolving the full manifold of ^{87}Sr atoms, we simulate the proposed OSG sequence. The sequence with two different OSG beams has an increased parameter space to choose from. In order to systematically study the feasibility, we restrict the parameters to the following settings. We fix the detuning of both OSG beams to the minimal detuning of 300 MHz. From the plot in figure 5.9, it is visible

that a closer detuning leads to a larger potential difference among either half of the spin manifold. The timing of the two beams is fixed to 2.5 μs each in order to have the same total OSG beam application of 5 μs. With this timing, we avoid chances of off-resonant scattering and stay in the linear regime of the OSG potential and do not explore the full OSG potential too much. Furthermore, we fix the imaging resolution to be the best possible case of 0.6 μm and assume the atoms to initially be in the ground state of the tweezer trap. The remaining parameter is the free expansion time that we leave as a free parameter to scan at which separation distance a full $N = 10$ resolution is possible. The results of the simulation are depicted in figure 5.27 for an expansion time of 1800 μs.

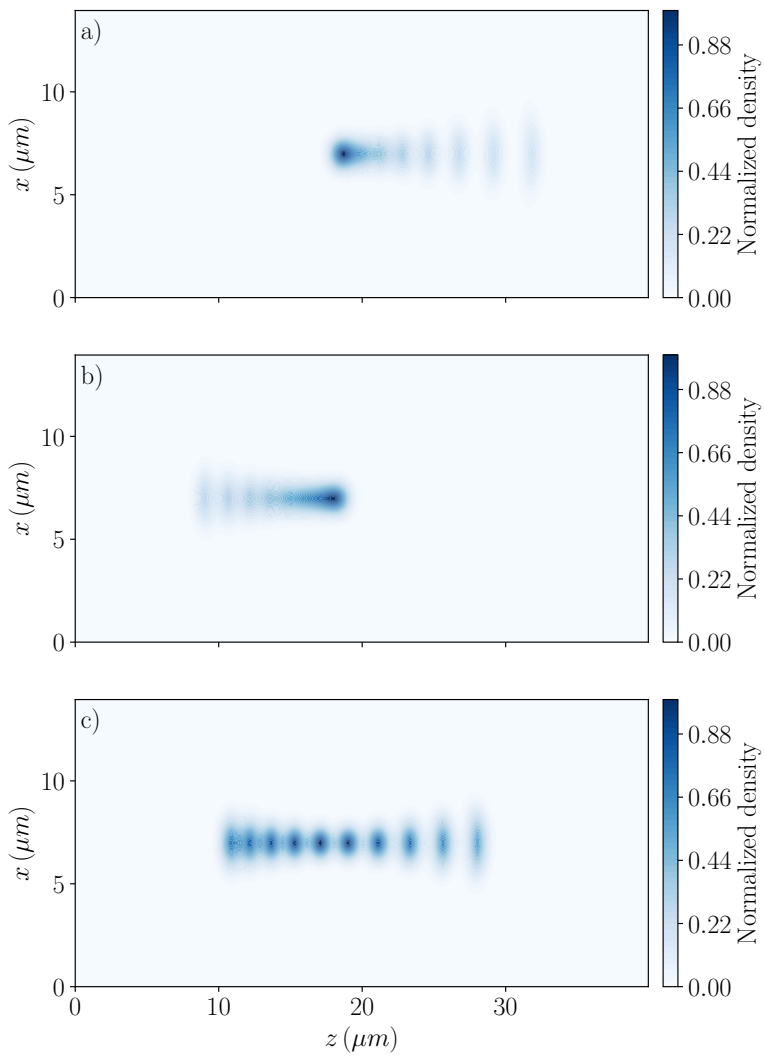

FIGURE 5.27: Detection of the full spin manifold of ^{87}Sr. a) Simulated spin separation for 2.5 μs of a first OSG beam with 300 MHz blue detuning and 1800 μs free expansion. b) Spin separation for 2.5 μs of the second OSG beam with 300 MHz red detuning and opposite circular polarization but same 1800 μs free expansion c) Combining the two OSG applications sequentially results in a visible separation of all 10 m_F-states. All simulation results are convoluted with the optimized imaging spread of 0.6 μm.

In figure 5.27 a) and 5.27 b), we show how the individual OSG beams separate one half of the spin manifold in either direction. In figure 5.27 c), we then consider the combined effect of both beams in the proposed sequence. As a result, the one-sided separation turns into a more equally spaced separation, with a sufficiently large separation to yield

a visible number of 10 distinct spin clusters. Comparing the combined sequence with the individual sequence shows that the two beams counteract each other. We obtain a smaller separation for the combined sequence than when considering each beam individually. The detection fidelities vary significantly, ranging from 99.6 % to 86.2 %.

The separation is not perfectly homogeneous among all spin clusters. The reduced separation from the second beam is directly translated into the full separation. However, the observed asymmetry could potentially be corrected by adapting the OSG application time from 2.5 μs to 3.0 μs only for the second OSG beam. Another possibility would be to use a different frequency for the second OSG beam. This shows that parameters such as timing and frequency provide many options to tailor the spin separation as desired. A full study of all possibilities and limitations of the optimal OSG beam sequence goes beyond the scope of this thesis. All in all, the simulations suggest that an equal spacing of the full spin manifold of ^{87}Sr could be achieved by applying a suitable OSG beam sequence.

To evaluate whether the implementation in the experiment is realistic, we determine how much space is required to achieve a sufficiently high detection fidelity. For this purpose, we apply a Gaussian mixture model to simulations with different free expansion times. Since all spin states have different detection fidelities, we consider the minimal detection fidelity among them. To make this quantity comparable to experimental settings such as the magnification of the imaging system and the lattice spacing, we plot the minimal detection fidelity as a function of the maximal separation between the outermost stretched spin states ($m_F = \pm 9/2$). The plot in figure 5.28 shows a linear correspondence. Generally, more space is required to reach a better detection fidelity. For expansion times below 1400 μs and 18 μm, the spin clusters begin to overlap and only a reduced number of spin states can be reliably fitted with the Gaussian mixture model. By further improving the imaging resolution or reducing the spread during free expansion by using a shallower trap, we could shift this characteristic curve further upward. This would allow the same detection fidelity over a smaller spatial range.

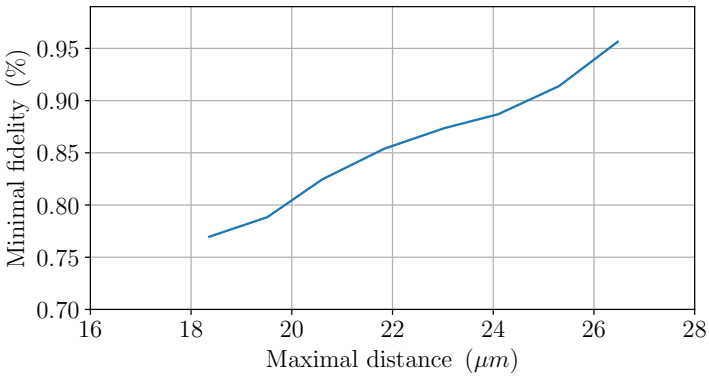

FIGURE 5.28: Detection of 10 spin states as function of maximal separation distance. The minimal fidelity of the simulated sequential OSG beam application is taken out of all 10 calculated detection fidelities and reported for varying free-expansion time. As separation distance, we define the distance between the two outermost spin clusters. Below 18 μm and 1400 μs free expansion time, spin clusters start to overlap and only a reduced number of spin states can be reliability fitted with the Gaussian mixture model.

Chapter 6

Conclusion and Outlook

In this thesis, we presented the experimental techniques used for the preparation and spin-resolved imaging of individual ^{87}Sr atoms. This includes the construction of the experiment and the development of cooling methods for strontium atoms. Our setup enables high-fidelity single-atom imaging of atoms in tweezer traps and rapid imaging in free space with μm-scale resolution. By combining free-space imaging with spin-dependent optical potential gradients, we could achieve simultaneous single-atom number and spin resolution. We employ an optical Stern-Gerlach potential, which spatially separates ^{87}Sr atoms according to the magnitude of their nuclear spin projection $|m_F|$. Our novel method enables the separation of 4 out of 10 possible m_F states within the ground-state spin manifold of ^{87}Sr and enables the investigation of systems exhibiting SU(4) spin symmetry. Our results offer several exciting perspectives for quantum information science based on the large nuclear spin manifold of strontium, which we briefly outline below.

From one atom to many

We have demonstrated our spin separation technique with a single atom. However, our approach can readily be scaled up for studying quantum many-body physics in optical lattices or in programmable tweezer arrays.

Although the parallel application of OSG beams to individual atom positions requires a linearly increasing laser power, suitable higher-power laser systems with narrow linewidth in 689 nm-region exist to provide enough power for hundreds of atoms. These laser systems use sum frequency generation of high-power fiber lasers to generate 4 W of 698 nm light [109]. Similar to tweezer systems, several tailored OSG beams could then be generated with a spatial light-modulator (SLM). Given a required power of 3.25 mW per OSG beam and atom position, we estimate from our experiment a feasible number of OSG beams of around 500, assuming the SLM works with 80 % efficiency at red light and other optical losses in the system are limited to 50 %. The estimated number shows that our technique can already be scaled to study system sizes that are not trivial to simulate numerically.

By applying the OSG beam sequentially, with tailored polarization and detuning, we could simulate that the OSG spin separation is able to resolve the full $N = 10$ spin manifold of ^{87}Sr atoms. Applying the spin separation to several atoms in a potential grid is ultimately limited by the separation distance that is required for high-fidelity detection. For optimized atom temperatures and imaging resolution, we could resolve 10 spin states over a spatial region of $20\,\mu\text{m}\times 4\,\mu\text{m}$, which is well accessible for tweezer arrays, but may be challenging for optical lattices. Adapting the separation direction to the grid geometry, one could for example, separate the atoms along the diagonal of a square grid and gain $\sqrt{2}$ more space. Furthermore, controlling the timings, polarization and frequency of several tailored OSG beams has additional unexplored potential to make the spin separation more space efficient. Even if the spin resolution is limited, the spin-dependent OSG potentials

provide a way to control the initial spin state configuration by superimposing a vector or tensor potential with the trapping potential and selectively removing certain spin states. This approach is routinely used in preparing ^{87}Sr atoms for an optical lattice clock [32].

Quantum gas microscopy of SU(N) fermions

Applying our technique to quantum gas microscopy opens a wide range of possibilities for exploring the rich phase diagram of the SU(N) Fermi-Hubbard model.

Our approach is well-suited for imaging the magnetic ordering of the SU(3) Fermi-Hubbard model. By restricting the system from general SU(N) physics to SU(3), we can focus on a regime that matches our capabilities for resolving up to 4 nuclear-spin components. This restriction also leaves room to adjust the method to the specific requirements of the problem, for example, the needed spin resolution in a finite NA imaging system or the achievable system size. We therefore focus in the following on the SU(3) Fermi-Hubbard model with repulsive interactions in a 2D square lattice at a commensurate filling of 1/3. In this regime, several theoretical works using different numerical techniques have predicted consistent results for the low-entropy phases of the model [55, 56, 110, 111, 112]. Once higher temperatures, spin imbalances, more spin components, or doping are considered, the number of possible phases increases significantly [113, 114, 115]. For this reason, we focus our experimental efforts on the low-entropy phases at integer filling that still await confirmation by experiment.

The first challenge is to reach the low temperatures that have also been critical for observing the first SU(2) antiferromagnetic phase [20]. Our strontium atoms provide an efficient route to creating a deeply degenerate Fermi system, since the many spin components help to keep the collision and thermalization rate high during evaporative cooling and efficiently remove entropy from the system [31, 32].

Once these low temperatures are reached, our single-site and spin-resolved imaging should allow us to measure spin correlators of the form $C_d = <S_i S_j>$, where the correlator is averaged over all pairs of sites with a displacement of d. This correlator has been used in theoretical studies and also in the experimental identification of magnetic orderings for the SU(2) Fermi-Hubbard model, where the decay or saturation of the spin correlator signal allows one to distinguish between different ordering patterns and identify long-range magnetic order [116].

Depending on the ratio U/t of interaction U and tunneling t, the SU(3) Fermi-Hubbard model can exhibit different magnetic orderings. In the large U/t limit, Fermi-Hubbard physics generally leads to localized particles and in the case of SU(3) symmetry at low temperatures to a three-component AFM ordering with stripe-like patterns [55, 56].

Beyond the large coupling-limit at intermediate values of U/t, additional ordering patterns are expected. These orderings can appear with different periodicities along different spatial directions. For example, the 3-2 AFM phase presents itself as an ordered pattern with period 3 of one spin component in one direction and period 2 in the other direction. Similarly, the 3-4 AFM phase emerges when the interaction U increases. At vanishing interactions U, the system ultimately reaches the paramagnetic regime with uniform spin correlations [110, 111]. Including a finite temperature, simulations predict that shorter-range spin correlations can be observed at commensurate fillings [117]. In the finite-temperature regime, we can also exploit the strength of our free-space imaging with an effective number resolution. The number resolution would allow us to detect doublon excitations [53, 118]. Finally, exploring filling factors beyond the commensurate 1/3 would be possible and may reveal further interesting phases [113].

An experimental challenge for us will be to implement a suitable optical lattice geometry. The lattice spacing has to be short enough on the half-micrometer scale to allow for the

tunneling process and Fermi-Hubbard physics. At the same time, it also needs the possibility to change to the spacing that is required to spatially separate the spin states and perform spin-resolved imaging. For our detection method we need an atomic distance on the scale of several micrometers. A solution for that is optical accordion lattices, which have proven to be an effective tool in studying the ordering of magnetic erbium atoms [119].

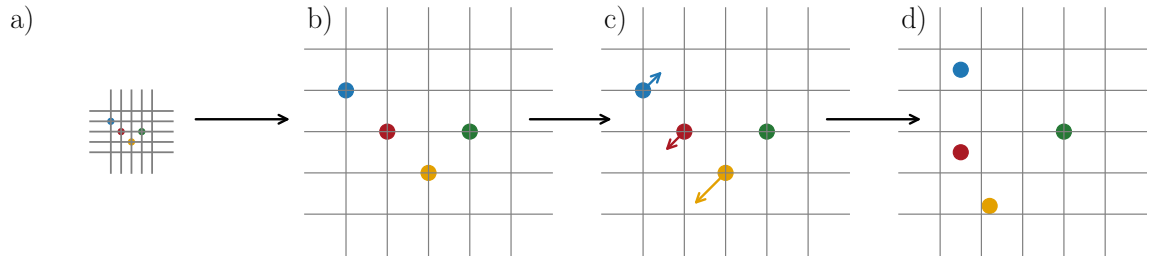

FIGURE 6.1: Conceptual overview of a quantum gas microscope for studying SU(N) Fermi Hubbard physics with an accordion lattice and our spin-resolved imaging technique. a) The Fermi-Hubbard system is initialized by loading degenerate ^{87}Sr atoms into a short-spaced lattice. The minimal lattice spacing with our green accordion lattice is 470 nm. b) The dynamics are frozen by ramping up the lattice depth and the accordion lattice is expanded to enable the spin-resolved imaging. c) One OSG beam is applied per lattice site which separates the atoms based on their spin state. d) Lastly, the atom number and spin composition is imaged with the free-space imaging technique.

Preparing our experimental apparatus as a quantum simulator platform for the SU(3) Fermi Hubbard model is part of the ongoing efforts in the lab. For a successful implementation, we are creating a degenerate Fermi gas, preparing a number of resolvable spin states, and loading the atoms into an accordion lattice. An accordion lattice with 520 nm light has already been constructed by my colleague Leon Schaefer and is being applied to the atoms at the time of writing this thesis. The lattice gas is initially loaded into an optical lattice with a minimal spacing of 470 nm for Fermi-Hubbard physics. After freezing the dynamics by ramping up the lattice depth, the lattice spacing is increased up to 10 μm for the detection sequence. For single-atom spin-resolved imaging, a set of tightly focused OSG beams is generated at each lattice site using an SLM. This experimental concept is illustrated in figure 6.1. The full state resolution of the system provides the necessary data to calculate correlation functions and unravel the predicted phases for various system parameters.

Synthetic dimensions

Alternatively, with single-state detection and simultaneous coherent control within the spin manifold, our spin separation technique provides a way to utilize the large spin manifold of ^{87}Sr as a synthetic dimension for engineering gauge fields [120, 121, 122, 123]. Raman transitions between nuclear spin states allow to mimic the effect of an Aharonov–Bohm phase acquired for charged quantum particles in a magnetic field [124]. Such implementation mimics the physics of the quantum Hall effect and spin-orbit coupling and in presence of interactions, may enable access to fractional quantum Hall physics [125, 126] and other correlated topological phases [127]. A feasible implementation for our experiment would be to use atoms in a 1D optical lattice, where the reduced dimension of the lattice provides sufficient space to fully resolve the synthetic dimension for a $N = 10$ spin manifold.

Quantum computing

Beyond analog quantum simulations, our technique is also relevant for quantum information science, where multi-level qudits encoded in the nuclear-spin states offer enhanced information density and new opportunities for quantum algorithms [128, 129]. The large nuclear spin of strontium provides a $log_{10}(N)$ enhancement of information storage capacities instead of $log_2(N)$, drastically reducing system sizes [130]. Due to the weak coupling to external magnetic fields, the nuclear spin additionally provides long coherence times [107, 131, 132, 133, 134]. By using Raman transitions within the spin manifold, spin-cat states can be created, enabling new possibilities for fault-tolerant quantum computing [135, 69], mid-circuit measurements, and erasure conversion protocols [136, 100].

Overall, our spin-resolved single-atom microscopy method opens up several exciting avenues for our experiment and for exploiting the large ground-state nuclear spin manifold as a highly coherent resource for quantum information and quantum simulation.

Appendix A

Zeeman shifts

The coupling of small external magnetic fields to the total dipole moment of the atoms is given by the Zeemann shift. The external fields that we have applied in the experiment are MOT magnetic fields and compensation fields to alter the energy of certain magnetic m_F-levels. The Zeeman energy shift is calculated with the following expression.

$$\Delta_{Zeeman} = \boldsymbol{\mu} \cdot \boldsymbol{B} = m_F g_F \mu_B B \tag{A.1}$$

with the magnetic field B, the projection of angular momentum onto B the magnetic quantum number m_F, the Bohr magneton μ_B and the total Landé g-factor g_F. The Landé g-factor is a combination of the following equations

$$g_F = g_J \frac{[F(F+1) - I(I+1) + J(J+1)]}{2F(F+1)} + g_I \frac{[F(F+1) + I(I+1) - J(J+1)]}{2F(F+1)} \tag{A.2}$$

$$g_J = g_L \frac{J(J+1) - S(S+1) + L(L+1)}{2J(J+1)} + g_S \frac{J(J+1) + S(S+1) - L(L+1)}{2J(J+1)} \tag{A.3}$$

where we use the Total angular momentum $F = J + I$, Electronic angular momentum $J = L + S$, the Electronic orbital angular momentum L, Electronic spin angular momentum S, the Nuclear angular momentum I, Electron orbital Landé g-factor g_L, Electron spin Landé g-factor g_S and the Nuclear Landé g-factor g_I [137].
The resulting Zeeman shifts for the most relevant transitions in this work are presented in table A.1. Of particular interest is the Zeeman shift of the $^1S_0$ state in ^{87}Sr that dictated the Spin dynamics in Chapter 5.3. In the work of [73] a Zeeman shift of 108 Hz/G is measured whereas in a recent study [138] a Zeeman shift of 184 Hz/G has been measured. We find that 184 Hz/G matches better to our Spin dynamics observations.

Isotope	State	Zeeman shift in $kHz/m_F B$
	$^1S_0$	0
	$^1P_1$	1399.5
	$^3P_0$	0
^{88}Sr	$^3P_1$	2099
	$^3P_2$	2099
	$^3S_1$	2799.1
	$^1S_0$	-0.184
^{87}Sr	$^1P_1\ F = 7/2$	-311.1
	$^1P_1\ F = 9/2$	56.4
	$^1P_1\ F = 11/2$	254.4
	$^3P_0\ F = 9/2$	-0.184
	$^3P_1\ F = 7/2$	-466.7
	$^3P_1\ F = 9/2$	84.7
	$^3P_1\ F = 11/2$	381.6

TABLE A.1: Isotope quantum numbers and Zeeman shifts

Constants and variables:

B (Magnetic field strength)

μ_B (Bohr magneton)

μ_N (Nuclear magneton)

$F = J + I$ (Total angular momentum)

$J = L + S$ (Electronic angular momentum)

L (Electronic orbital angular momentum)

S (Electronic spin angular momentum)

I (Nuclear angular momentum)

$g_L \simeq 1$ (Electron orbital Landé g-factor)

$g_S \simeq 2.00231930437$ (Electron spin Landé g-factor)

$g_I = -0.1422\frac{\mu_N}{\mu_B}$ (Nuclear Landé g-factor)

m_F (Projection of angular momentum onto $\boldsymbol{B}$ field; $-F \leq m_F \leq F$)

Appendix B

Light shifts

Whenever an atom is inside the perimeter of a laser beam, the oscillating electric field of the laser interacts with the atom. The internal states of the atoms have to be interpreted as modified states inside the coupled system of electric field and atom together. The modified energies of the resulting states are referred as AC Stark shifts or light shifts. Along the spatially varying electric field strength of a laser beam the atom experiences an optical dipole potential. In the thesis several different dipole potentials have been used from the tweezer potential to the optical Stern-Gerlach beam. The optical dipole potential of a focused laser beam is calculated in radial and axial direction [90]. For a given internal state i the radial dipole potential is expressed through

$$U_i(r) = -\frac{1}{2\epsilon_0 c} I_0(r)\, \alpha_i(\lambda) = -\frac{P}{\epsilon_0 c \pi w_0^2} e^{2r^2/w_0^2}\, \alpha_i(\lambda) \tag{B.1}$$

where ϵ_0 is the vacuum permittivity, c is the speed of light, I_0 is the laser intensity, P is the laser power, λ is the laser wavelength, w is the beam waist, r is the distance from the optical axis and α is the polarizability of the state. For the axial direction z the dipole potential is given by

$$U_i(z) = -\frac{P}{\epsilon_0 c \pi w_0^2} \frac{1}{1 + (\frac{\lambda z}{\pi w_0^2})}\, \alpha_i(\lambda) \tag{B.2}$$

In the following appendix section, we aim to describe the theoretical framework to calculate the polarizabilities and light shifts of the relevant states of strontium.

Next, we derive expressions for the polarizability of states that are characterized by their hyperfine quantum numbers. The formulas are extracted from [137]. We start the equations with an expression for the hyperfine shift based on the A and B hyperfine coefficients. These coefficients come from the atomic data base [71] and are experimentally found values. We list all states that have been used in the calculation with their respective A, B coefficients and lifetimes in table B.1.

For the hyperfine shift we define two expressions

$$K(F) = F(F+1)I(I+1)J(J+1) \tag{B.3}$$

and

$$D = 2I(2I-1) \times 2J(2J-1) \tag{B.4}$$

The hyperfine shift is then given by

$$\Delta E_{HF}(F) = \frac{K(F)}{2} \cdot A + \delta_{quad} \tag{B.5}$$

where δ_{quad} is given by

$$\delta_{quad} = \begin{cases} 0, & \text{if } D = 0 \\ \dfrac{\frac{3}{2}K(F)(K(F)+1) - 2I(I+1)J(J+1)}{D} \cdot B, & \text{if } D \neq 0 \end{cases} \tag{B.6}$$

The hyperfine state energies will enter the expression of the hyperfine dipole matrix elements next. The dipole matrix elements describe the coupling of the light field to the atomic state where only the angular quantum numbers matter for the state depending coupling. The radial part of the states are compressed in the decay rates of each state.

$$|\langle J_i, I, F_i \| d \| J_f, I, F_f \rangle|^2 = \left(\frac{\Gamma \times 3\pi\epsilon_0 \hbar c^3}{|\omega_{J_f J_i}|^3} \cdot \frac{2J_i + 1}{2J_f + 1} \right) \cdot (2J_i + 1) \cdot (2F_f + 1) \cdot \begin{Bmatrix} J_i & J_f & 1 \\ F_f & F_i & I \end{Bmatrix}^2 \tag{B.7}$$

with the variables

d : Dipole operator
I : Nuclear spin quantum number
F_i : Initial total angular momentum quantum number
F_f : Final total angular momentum quantum number
J_i : Initial electronic angular momentum quantum number
J_f : Final electronic angular momentum quantum number
$\omega_{J_f J_i} = \omega_f - \omega_i$: Energy (frequency) difference between states
Γ : Decay rate (linewidth) from the higher to the lower state
$\{\ \}$: 6j-Symbol

Each available state contributes to the total polarizability, which is expressed as a sum over F_f. Renaming equation B.7 as M_{F_f}, leads to the following expression for the scalar, vector, and tensor polarizability.

$$\alpha_s = \frac{2}{3} \sum_{F_f} \frac{\omega_{F_f F_i} \times M_{F_f}}{\hbar(\omega^2_{F_f F_i} - \omega^2)} \tag{B.8}$$

$$\alpha_v = \sum_{F_f} (-1)^{F_i + F_f + 1} \sqrt{\frac{6F_i(2F_i+1)}{F_i+1}} \times \begin{Bmatrix} 1 & 1 & 1 \\ F_i & F_i & F_f \end{Bmatrix} \times \frac{\omega_{F_f F_i} \times M_{F_f}}{\hbar(\omega^2_{F_f F_i} - \omega^2)} \times \frac{\omega}{\omega_{F_f F_i}} \tag{B.9}$$

$$\alpha_T = \sum_{F_f} (-1)^{F_i + F_f} \sqrt{\frac{40F_i(2F_i+1)(2F_i-1)}{3(F_i+1)(2F_i+3)}} \times \begin{Bmatrix} 1 & 1 & 2 \\ F_i & F_i & F_f \end{Bmatrix} \times \frac{\omega_{F_f F_i} \times M_{F_f}}{\hbar(\omega^2_{F_f F_i} - \omega^2)} \tag{B.10}$$

As a next step we define the electrical field E_0 from the laser beam intensity I_0 of the laser light in order to calculate the final light shifts:

$$E_0^2 = \frac{I_0 \times 10^4}{2\epsilon_0 c h} \tag{B.11}$$

$$\Delta\nu_{\text{scalar}} = -\frac{\alpha_s(\lambda) \times E_0^2}{h}$$

$$\Delta\nu_{\text{vector}} = \begin{cases} -\frac{\alpha_v(\lambda)\times m_F \times q \times E_0^2}{F\times h} & \text{if } F > 0 \\ 0 & \text{if } F \leq 0 \end{cases}$$

$$\Delta\nu_{\text{tensor}} = \begin{cases} -\frac{\alpha_T(\lambda)\times(3m_F^2 - F(F+1))}{F(2F-1)} \times \frac{3(1-|q|)-1}{2} \times \frac{E_0^2}{h} & \text{if } F > \frac{1}{2} \\ 0 & \text{if } F \leq \frac{1}{2} \end{cases}$$

The following additional variables have been used to characterize the light field and the atomic state

λ (wavelength of the light field in nm)

ω (frequency of the light field in Hz)

$q \in \{-1, 0, 1\}$ (polarization of the light field: σ^-, π, σ^+)

I_0 (Intensity of the light in mW/cm^2)

m_F (Projection of total angular momentum onto quantization axis)

State	Energy ω_i in Hz	A in MHz	B in MHz
$5s5s\,^1S_0$	0	0	0
$5s5p\,^3P_0$	429227851741500.0	0	0
$5s5p\,^3P_1$	434827974856940.0	-260.084	-35.658
$5s5p\,^3P_0$	446647682243785.44	-212.765	67.34
$5s5p\,^1P_1$	650504664991300.0	-3.4	39
$5s4d\,^3D_1$	544394803319964.9	0	0
$5s4d\,^3D_2$	546185733484810.94	0	0
$5s4d\,^3D_3$	549197808268828.6	0	0
$5s6s\,^3S_1$	870560513497403.4	0	0
$5s5d\,^3D_1$	1049480699629986.5	0	0
$5p5p\,^3P_1$	1061268449140809.1	0	0
$5p5p\,^3P_2$	1069498711448774.6	0	0
$4p4p\,^3P_1$	1336952047357136.0	0	0
$5s7s\,^3S_1$	1121963530810115.0	0	0

TABLE B.1: Internal states of strontium used in light shift calculation. The state energies have been extracted from the NIST data base [71] and the relevant A and B coefficients form [73]

State i	State f	Decay rate Γ in Hz
$5s5s\,^1S_0$	$5s5p\,^1P_1$	2.01e+08
$5s5s\,^1S_0$	$5s5p\,^3P_1$	4.69e+04
$5s5p\,^3P_1$	$5s6s\,^3S_1$	2.7e+07
$5s5p\,^3P_1$	$5p5p\,^3P_2$	3.6e+07
$5s5p\,^3P_1$	$5p6p\,^3P_1$	3.0e+07
$5s5p\,^3P_1$	$5s7s\,^3S_1$	9.7e+06
$5s5p\,^3P_1$	$5s5d\,^3D_1$	2.63e+07

TABLE B.2: Documented transitions of strontium used in light shift calculation. The lifetimes have been extracted from the NIST data base [71].

Appendix C

Magnetic field calculations

C.1 Magnetic field

In this appendix we present the formulas for the magnetic fields of our diamond shaped coils. The calculations start with considering the magnetic field of a loop of wire that is given by the Biot-Savart law.

$$\vec{B} = \frac{\mu_0 I}{4\pi} \int \frac{\vec{dl}' \times (\vec{r} - \vec{r}')}{|\vec{r} - \vec{r}'|^3} \tag{C.1}$$

with I the current through the wire, μ_0 the magnetic permeability, $\vec{r}$ the point in space where the field is computed, and $\vec{r}'$ the position of the wire in space. The integral is a closed integral over the current loop with the differentials $\vec{dl}'$ along the current loop. We apply the Biot-Savart law to a idealized diamond shaped current loop. The setup is shown in figure C.1. Space is oriented such that the z-axis is oriented along the B-Field lines. This means for our setup, that with two current loops in the Helmholtz configuration we will have the strong homogeneous field in the z-axis. The diamond shape appears stretched in the x-axis. We set the x-axis to be aligned with the long axis b and the y-axis with the short axis a of the diamond.

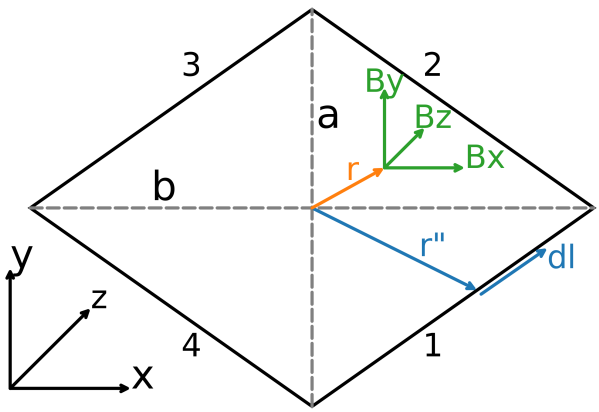

FIGURE C.1: Parametrization of a wire loop of our diamond coils in the coordinate system of our experiment.

Applying the Biot-Savart law requires a parametrization of the current loop. Since the current loop will be sitting in a plane, the integral simplifies if we do the parametrization based on one single parameter. Here, we will use the x-position between $x = 0$ and $x = b$ for parameterizing the current loop in space and assume that the current loop sits in the xy-plane at $z = D$. In comparison to the classical circular current loop the current loop

is not continuous which breaks up the diamond current loop in 4 different sections. As a result, the first section of the diamond shaped current loop is given by

$$\vec{r'}_1 = \begin{pmatrix} x' \\ -a + \frac{a}{b}x' \\ D \end{pmatrix} \tag{C.2}$$

The differential with respect to the parameter x' is given by

$$\vec{dl'} = \begin{pmatrix} 1 \\ \frac{a}{b} \\ 0 \end{pmatrix} dx \tag{C.3}$$

This gives the following expression for the integral

$$\vec{dl'} \times (\vec{r} - \vec{r'}) = \begin{pmatrix} dx' \\ \frac{a}{b}dx' \\ 0 \end{pmatrix} \times \begin{pmatrix} x - x' \\ y - (-a + \frac{a}{b}x') \\ z - D \end{pmatrix} = \begin{pmatrix} (z-D)\frac{a}{b}dx'dx' \\ -(z-D)dx' \\ (y - (-a + \frac{a}{b}x'))dx' - (x - x')\frac{a}{b}dx' \end{pmatrix} \tag{C.4}$$

This gives the following expressions for the B-field in z-direction for each loop section. The expression for each B-field component can be derived accordingly. We list the B-field expressions for the z-direction of each loop section below. In the end, the section have to be summed for the total B-field and repeated for every turn N_i. The underlying integrals have to be solved numerically.

$$B_z^1 = \frac{\mu_0 I}{4\pi} \int_0^x \frac{((y - (-a + \frac{a}{b}x') - \frac{a}{b}(x - x'))dx'}{((x - x')^2 + (y - (-a + \frac{a}{b}x'))^2 + (z - D)^2)^{3/2}} \tag{C.5}$$

$$B_z^2 = \frac{\mu_0 I}{4\pi} \int_0^x \frac{((y - (a - \frac{a}{b}x') + \frac{a}{b}(x - x'))dx'}{((x - x')^2 + (y - (-a + \frac{a}{b}x'))^2 + (z - D)^2)^{3/2}} \tag{C.6}$$

$$B_z^3 = \frac{\mu_0 I}{4\pi} \int_0^x \frac{((y - (a + \frac{a}{b}x') - \frac{a}{b}(x - x'))dx'}{((x - x')^2 + (y - (-a + \frac{a}{b}x'))^2 + (z - D)^2)^{3/2}} \tag{C.7}$$

$$B_z^4 = \frac{\mu_0 I}{4\pi} \int_0^x \frac{((y - (-a - \frac{a}{b}x') + \frac{a}{b}(x - x'))dx'}{((x - x')^2 + (y - (-a + \frac{a}{b}x'))^2 + (z - D)^2)^{3/2}} \tag{C.8}$$

Following the same steps expression for a rectangular coil shape can be found that apply to the compensation coils in x and y-direction of our experiment [139].

C.2 Dipole force on coils

Attractive and repulsive forces act on the coils and the coil holding structures. If the coil is in Helmholtz configuration the coils attract each other. If the coil is in Anti-Helmholtz configuration the coils repel each other. In this section we present the calculations for the mechanical forces acting on the coils. Two regimes determine the type and strength of the mechanical force. The first regime is the static regime. The second regime is the switch-off or switch-on regime where the quick change of magnetic field induces a large magnetic field in the partner coil. The current that is induced acts as a new dipole. The calculation considers the coils as dipoles that act on each other via the magnetic dipole force [140].

For simple calculations that will give an upper bound of the forces acting on the coils we approximate the diamond coil as a round current loop with 24 infinite small windings. With that the coil has a magnetic moment

$$m = NIA = NI\pi r^2 \tag{C.9}$$

with the radius r and the number of windings N. Consequently, the other coil has also a magnetic moment that interacts with the first one via the magnetic dipole force

$$F = \frac{3\mu_0}{4\pi D^4}(-2\vec{m}_1\vec{m}_2) \tag{C.10}$$

In the switching process, the coils induce a voltage in the opposite direction in the partner coil. This voltage can be calculated via

$$V = M_{12}\dot{I} = M_{12}\frac{I_{max}}{t_{ramp}} \tag{C.11}$$

M_{12} is the mutual inductance of the two coils in their specific arrangement. The mutual inductance determines how much magnetic flux goes through the partner coil and can be calculated with

$$M_{mn} = \frac{\mu_0}{4\pi}\oint_{C_m}\oint_{C_n}\frac{d\vec{x}_m \cdot d\vec{x}_n}{|\vec{x}_m - \vec{x}_n|} \tag{C.12}$$

with the closed path of the wire loop C_m. With the resulting voltage we can calculate the current $I_{induced} = V/R$ that will flow in the coils and repeat the calculation of the magnetic dipole force from a above.

C.3 Water cooling power

In this section, we quantify the effect of the wire dimension on the heating of the coil [140]. The calculation starts with estimating how much power we generate with the wire due to resistive heating. Then we calculate what water flow we need to compensate for the heating. We have chosen a 5×5 mm copper tube with a 3×3 mm inside tube with 16 mm^2 cross section. With an estimated length of $L = 20$ m and a specific resistivity for CW009A copper of $\rho = 0.01724\,\Omega\text{mm}^2/\text{m}$, the resistance equals to $R = 21.55\,\text{m}\Omega$. For the dissipated power in the coils we use the Ohmic law which gives at maximal current a power of

$$P = UI = RI^2 = 1939.5\,W \tag{C.13}$$

If we want to know about the voltage our power supply has to give when we have the two coils in series we have

$$U = 2RI = 12.93\,V \tag{C.14}$$

which is below the 20 V power supply voltage limit.

For the calculation of the cooling power of the copper tube, we first have to calculate the pressure drop. The pressure drop is affected by the material specific friction of the side walls of the tube and whether we have a laminar or turbulent flow in the tube. Generally, the longer the tube and smaller the cross section the larger the pressure drop is and the more pressure we need to obtain a reasonable cooling water flow through the copper tube. The calculation starts with the Colebrook-White equation for the friction factor f. We set the Reynolds number to $R_e = 4000$ which is something between the laminar and turbulent flow. The hydraulic diameter is the side length of $D_h = 3$ mm and the roughness factor of copper is $\epsilon = 0.002$ mm.

$$\frac{1}{\sqrt{f}} = -2log\left(\frac{\epsilon}{3.7D_h} - \frac{2.57}{R_e\sqrt{f}}\right) \tag{C.15}$$

Next, we calculate the volumetric flow Q through the pipe considering the Darcy-Weisbach equation. By rearranging this equation we obtain

$$Q = A\sqrt{\Delta p\frac{2}{\rho}\frac{D_h}{L}\frac{1}{f}} \tag{C.16}$$

with the Darcy-friction factor f from above, the density ρ of water, and a cross-section of $A = 9\,\mathrm{mm}^2$. For assuming a pressure of $\Delta p = 5\,\mathrm{bar}$ we obtain a water flow of $Q = 1.038\,\mathrm{L/min}$. The pressure is set to such a value since larger pressures increase the risk of plumbing failures and increase the cost of the chiller unit to a high pressure unit. We plug the water flow Q in the water cooling formula. The water flow times the density yields the mass flow of water. The specific heat of water is $C_p = 4.184 \times 1000\,\mathrm{J/kg\,°C}$.

$$\Delta T = \frac{P}{\dot{m}C_p} = \frac{DC \times P}{FRF \times Q\rho C_p} = 19.13\,°C \tag{C.17}$$

In addition, we add a duty cycle factor of $DC = 0.5$ and a flow reduction factor of $FRF = 0.7$. As a result, we obtain a reasonable acceptable temperature increase of 19.13 °C assuming the full length of the copper tube.

Bibliography

[1] Immanuel Bloch, Jean Dalibard, and Wilhelm Zwerger. "Many-body physics with ultracold gases". In: *Rev. Mod. Phys.* 80 (3 July 2008), pp. 885–964. DOI: 10.1103/RevModPhys.80.885.

[2] Christian Gross and Immanuel Bloch. "Quantum simulations with ultracold atoms in optical lattices". In: *Science* 357.6355 (2017), pp. 995–1001. DOI: 10.1126/science.aal3837.

[3] Kai-Niklas Schymik et al. "Enhanced atom-by-atom assembly of arbitrary tweezer arrays". In: *Phys. Rev. A* 102 (6 Dec. 2020), p. 063107. DOI: 10.1103/PhysRevA.102.063107.

[4] Richard P. Feynman. "Simulating physics with computers". In: *International Journal of Theoretical Physics* 21.6 (June 1982), pp. 467–488. ISSN: 1572-9575. DOI: 10.1007/BF02650179.

[5] Antoine Browaeys and Thierry Lahaye. "Many-body physics with individually controlled Rydberg atoms". In: *Nature Physics* 16.2 (2020), pp. 132–142. ISSN: 1745-2481. DOI: 10.1038/s41567-019-0733-z.

[6] Leticia Tarruell and Laurent Sanchez-Palencia. "Quantum simulation of the Hubbard model with ultracold fermions in optical lattices". en. In: *Comptes Rendus. Physique* 19.6 (2018), pp. 365–393. DOI: 10.1016/j.crhy.2018.10.013.

[7] Qijin Chen et al. "When superconductivity crosses over: From BCS to BEC". In: *Rev. Mod. Phys.* 96 (2 May 2024), p. 025002. DOI: 10.1103/RevModPhys.96.025002.

[8] T.-W. Zhou et al. "Observation of universal Hall response in strongly interacting Fermions". In: *Science* 381.6656 (2023), pp. 427–430. DOI: 10.1126/science.add1969.

[9] Victor Galitski, Gediminas Juzeliūnas, and Ian B. Spielman. "Artificial gauge fields with ultracold atoms". In: *Physics Today* 72.1 (Jan. 2019), pp. 38–44. ISSN: 1945-0699. DOI: 10.1063/pt.3.4111.

[10] G. Semeghini et al. "Probing topological spin liquids on a programmable quantum simulator". In: *Science* 374.6572 (2021), pp. 1242–1247. DOI: 10.1126/science.abi8794.

[11] Sylvain de Léséleuc et al. "Observation of a symmetry-protected topological phase of interacting bosons with Rydberg atoms". In: *Science* 365.6455 (2019), pp. 775–780. DOI: 10.1126/science.aav9105.

[12] Pimonpan Sompet et al. "Realizing the symmetry-protected Haldane phase in Fermi–Hubbard ladders". In: *Nature* 606.7914 (June 2022), pp. 484–488. ISSN: 1476-4687. DOI: 10.1038/s41586-022-04688-z.

[13] B. Keimer et al. "From quantum matter to high-temperature superconductivity in copper oxides". In: *Nature* 518.7538 (Feb. 2015), pp. 179–186. ISSN: 1476-4687. DOI: 10.1038/nature14165.

[14] Christian Gross and Waseem S. Bakr. "Quantum gas microscopy for single atom and spin detection". In: *Nature Physics* 17.12 (2021). Published: 2021/12/01, pp. 1316–1323. ISSN: 1745-2481. DOI: 10.1038/s41567-021-01370-5.

[15] Hongyun Zhang et al. "Angle-resolved photoemission spectroscopy". In: *Nature Reviews Methods Primers* 2.1 (2022), p. 54. ISSN: 2662-8449. DOI: 10.1038/s43586-022-00133-7.

[16] Øystein Fischer et al. "Scanning tunneling spectroscopy of high-temperature superconductors". In: *Rev. Mod. Phys.* 79 (1 Mar. 2007), pp. 353–419. DOI: 10.1103/RevModPhys.79.353.

[17] Annabelle Bohrdt et al. "Exploration of doped quantum magnets with ultracold atoms". In: *Annals of Physics* 435 (2021). Special issue on Philip W. Anderson, p. 168651. ISSN: 0003-4916. DOI: https://doi.org/10.1016/j.aop.2021.168651.

[18] Daniel Greif et al. "Site-resolved imaging of a fermionic Mott insulator". In: *Science* 351.6276 (2016), pp. 953–957. DOI: 10.1126/science.aad9041.

[19] Joannis Koepsell et al. "Microscopic evolution of doped Mott insulators from polaronic metal to Fermi liquid". In: *Science* 374.6563 (2021), pp. 82–86. DOI: 10.1126/science.abe7165.

[20] Anton Mazurenko et al. "A cold-atom Fermi–Hubbard antiferromagnet". In: *Nature* 545.7655 (May 2017), pp. 462–466. ISSN: 1476-4687. DOI: 10.1038/nature22362.

[21] Muqing Xu et al. "A neutral-atom Hubbard quantum simulator in the cryogenic regime". In: *Nature* 642.8069 (June 2025), pp. 909–915. DOI: 10.1038/s41586-025-09112-w.

[22] Jirayu Mongkolkiattichai et al. "Quantum gas microscopy of fermionic triangular-lattice Mott insulators". In: *Phys. Rev. A* 108 (6 Dec. 2023), p. L061301. DOI: 10.1103/PhysRevA.108.L061301.

[23] S. Baier et al. "Extended Bose-Hubbard models with ultracold magnetic atoms". In: *Science* 352.6282 (2016), pp. 201–205. DOI: 10.1126/science.aac9812.

[24] S. Lepoutre et al. "Out-of-equilibrium quantum magnetism and thermalization in a spin-3 many-body dipolar lattice system". In: *Nature Communications* 10.1 (2019), p. 1714. ISSN: 2041-1723. DOI: 10.1038/s41467-019-09699-5.

[25] A. Patscheider et al. "Controlling dipolar exchange interactions in a dense three-dimensional array of large-spin fermions". In: *Phys. Rev. Res.* 2 (2 Apr. 2020), p. 023050. DOI: 10.1103/PhysRevResearch.2.023050.

[26] Miguel A Cazalilla and Ana Maria Rey. "Ultracold Fermi gases with emergent SU(N) symmetry". In: *Reports on Progress in Physics* 77.12 (Nov. 2014), p. 124401. DOI: 10.1088/0034-4885/77/12/124401.

[27] Eduardo Ibarra-García-Padilla and Sayan Choudhury. "Many-body physics of ultracold alkaline-earth atoms with SU(N)-symmetric interactions". In: *Journal of Physics: Condensed Matter* 37.8 (Dec. 2024), p. 083003. DOI: 10.1088/1361-648X/ad9658.

[28] Florian Schäfer et al. "Tools for quantum simulation with ultracold atoms in optical lattices". In: *Nature Reviews Physics* 2.8 (Aug. 2020), pp. 411–425. ISSN: 2522-5820. DOI: 10.1038/s42254-020-0195-3.

[29] Y. Tokura and N. Nagaosa. "Orbital Physics in Transition-Metal Oxides". In: *Science* 288.5465 (2000), pp. 462–468. DOI: 10.1126/science.288.5465.462.

[30] Rahul Hingorani, Jaan Oitmaa, and Rajiv R. P. Singh. "Onset of charge incompressibility and Mott gaps in the honeycomb-lattice SU(4) Hubbard model: Lessons for twisted bilayer graphene systems". In: *Phys. Rev. B* 105 (24 June 2022), p. L241410. DOI: 10.1103/PhysRevB.105.L241410.

[31] Shintaro Taie et al. "An SU(6) Mott insulator of an atomic Fermi gas realized by large-spin Pomeranchuk cooling". In: *Nature Physics* 8.11 (2012), pp. 825–830. DOI: 10.1038/nphys2430.

[32] Lindsay Sonderhouse et al. "Thermodynamics of a deeply degenerate SU(N)-symmetric Fermi gas". In: *Nature Physics* 16.12 (2020), pp. 1216–1221. DOI: 10.1038/s41567-020-0986-6.

[33] Tobias Bothwell et al. "Resolving the gravitational redshift across a millimetre-scale atomic sample". In: *Nature* 602.7897 (2022), pp. 420–424. DOI: 10.1038/s41586-021-04349-7.

[34] B. J. Bloom et al. "An optical lattice clock with accuracy and stability at the $1018^{-18}18$*level*". In: *Nature* 506.7486 (2014), pp. 71–75. ISSN: 1476-4687. DOI: 10.1038/nature12941.

[35] Nathan Schine et al. "Long-lived Bell states in an array of optical clock qubits". In: *Nature Physics* 18.9 (2022), pp. 1067–1073. DOI: 10.1038/s41567-022-01678-w.

[36] Ivaylo S. Madjarov et al. "High-fidelity entanglement and detection of alkaline-earth Rydberg atoms". In: *Nature Physics* 16.8 (2020), pp. 857–861. ISSN: 1745-2481. DOI: 10.1038/s41567-020-0903-z.

[37] A. V. Gorshkov et al. "Two-orbital SU(N) magnetism with ultracold alkaline-earth atoms". In: *Nature Physics* 6.4 (Apr. 2010), pp. 289–295. ISSN: 1745-2481. DOI: 10.1038/nphys1535.

[38] Simon Stellmer, Rudolf Grimm, and Florian Schreck. "Production of quantum-degenerate strontium gases". In: *Phys. Rev. A* 87 (1 Jan. 2013), p. 013611. DOI: 10.1103/PhysRevA.87.013611.

[39] Christian Hofrichter et al. "Direct Probing of the Mott Crossover in the SU(N) Fermi-Hubbard Model". In: *Phys. Rev. X* 6 (2 June 2016), p. 021030. DOI: 10.1103/PhysRevX.6.021030.

[40] G. Pasqualetti et al. "Equation of State and Thermometry of the 2D SU(N) Fermi-Hubbard Model". In: *Phys. Rev. Lett.* 132 (8 Feb. 2024), p. 083401. DOI: 10.1103/PhysRevLett.132.083401.

[41] Hideki Ozawa et al. "Antiferromagnetic Spin Correlation of SU($\mathcal{N}$) Fermi Gas in an Optical Superlattice". In: *Phys. Rev. Lett.* 121 (22 Nov. 2018), p. 225303. DOI: 10.1103/PhysRevLett.121.225303.

[42] Shintaro Taie et al. "Observation of antiferromagnetic correlations in an ultracold SU(N) Hubbard model". In: *Nature Physics* 18.11 (2022). Published: 2022/11/01, pp. 1356–1361. ISSN: 1745-2481. DOI: 10.1038/s41567-022-01725-6.

[43] Shintaro Taie et al. "Realization of a SU(2) $\times$ SU(6) System of Fermions in a Cold Atomic Gas". In: *Phys. Rev. Lett.* 105 (19 Nov. 2010), p. 190401. DOI: 10.1103/PhysRevLett.105.190401.

[44] Simon Stellmer, Rudolf Grimm, and Florian Schreck. "Detection and manipulation of nuclear spin states in fermionic strontium". In: *Phys. Rev. A* 84 (4 Oct. 2011), p. 043611. DOI: 10.1103/PhysRevA.84.043611.

[45] Ahmed Omran et al. "Microscopic Observation of Pauli Blocking in Degenerate Fermionic Lattice Gases". In: *Phys. Rev. Lett.* 115 (26 Dec. 2015), p. 263001. DOI: 10.1103/PhysRevLett.115.263001.

[46] Maxwell F. Parsons et al. "Site-Resolved Imaging of Fermionic ^{6}Li in an Optical Lattice". In: *Phys. Rev. Lett.* 114 (21 May 2015), p. 213002. DOI: 10.1103/PhysRevLett.114.213002.

[47] Tim de Jongh et al. "Quantum Gas Microscopy of Fermions in the Continuum". In: *Phys. Rev. Lett.* 134 (18 May 2025), p. 183403. DOI: 10.1103/PhysRevLett.134.183403.

[48] Jin Yang et al. "Site-Resolved Imaging of Ultracold Fermions in a Triangular-Lattice Quantum Gas Microscope". In: *PRX Quantum* 2 (2 June 2021), p. 020344. DOI: 10.1103/PRXQuantum.2.020344.

[49] Elmar Haller et al. "Single-atom imaging of fermions in a quantum-gas microscope". In: *Nature Physics* 11.9 (2015), pp. 738–742. ISSN: 1745-2481. DOI: 10.1038/nphys3403.

[50] Lawrence W. Cheuk et al. "Quantum-Gas Microscope for Fermionic Atoms". In: *Phys. Rev. Lett.* 114 (19 May 2015), p. 193001. DOI: 10.1103/PhysRevLett.114.193001.

[51] A. Fuhrmanek et al. "Light-assisted collisions between a few cold atoms in a microscopic dipole trap". In: *Phys. Rev. A* 85 (6 June 2012), p. 062708. DOI: 10.1103/PhysRevA.85.062708.

[52] Maxwell F. Parsons et al. "Site-resolved measurement of the spin-correlation function in the Fermi-Hubbard model". In: *Science* 353.6305 (2016), pp. 1253–1256. DOI: 10.1126/science.aag1430.

[53] Joannis Koepsell et al. "Robust Bilayer Charge Pumping for Spin- and Density-Resolved Quantum Gas Microscopy". In: *Phys. Rev. Lett.* 125 (1 July 2020), p. 010403. DOI: 10.1103/PhysRevLett.125.010403.

[54] Carlos Gas-Ferrer et al. *Spin-resolved microscopy of ^{87}Sr SU(N) Fermi-Hubbard systems*. 2026. arXiv: 2603.05478 [cond-mat.quant-gas]. URL: https://arxiv.org/abs/2603.05478.

[55] Tamás A. Tóth et al. "Three-Sublattice Ordering of the SU(3) Heisenberg Model of Three-Flavor Fermions on the Square and Cubic Lattices". In: *Phys. Rev. Lett.* 105 (26 Dec. 2010), p. 265301. DOI: 10.1103/PhysRevLett.105.265301.

[56] Bela Bauer et al. "Three-sublattice order in the SU(3) Heisenberg model on the square and triangular lattice". In: *Phys. Rev. B* 85 (12 Mar. 2012), p. 125116. DOI: 10.1103/PhysRevB.85.125116.

[57] Martin Greiter and Stephan Rachel. "Valence bond solids for SU(n) spin chains: Exact models, spinon confinement, and the Haldane gap". In: *Phys. Rev. B* 75 (18 May 2007), p. 184441. DOI: 10.1103/PhysRevB.75.184441.

[58] Michael Hermele, Victor Gurarie, and Ana Maria Rey. "Mott Insulators of Ultracold Fermionic Alkaline Earth Atoms: Underconstrained Magnetism and Chiral Spin Liquid". In: *Phys. Rev. Lett.* 103 (13 Sept. 2009), p. 135301. DOI: 10.1103/PhysRevLett.103.135301.

[59] Martin Boll et al. "Spin- and density-resolved microscopy of antiferromagnetic correlations in Fermi-Hubbard chains". In: *Science* 353.6305 (2016), pp. 1257–1260. DOI: 10.1126/science.aag1635.

[60] Tsung-Yao Wu et al. "Stern–Gerlach detection of neutral-atom qubits in a state-dependent optical lattice". In: *Nature Physics* 15.6 (2019), pp. 538–542. ISSN: 1745-2481. DOI: 10.1038/s41567-019-0478-8.

[61] Minho Kwon et al. "Parallel Low-Loss Measurement of Multiple Atomic Qubits". In: *Phys. Rev. Lett.* 119 (18 Oct. 2017), p. 180504. DOI: 10.1103/PhysRevLett.119.180504.

[62] J. D. Thompson et al. "Coherence and Raman Sideband Cooling of a Single Atom in an Optical Tweezer". In: *Phys. Rev. Lett.* 110 (13 Mar. 2013), p. 133001. DOI: 10.1103/PhysRevLett.110.133001. URL: https://link.aps.org/doi/10.1103/PhysRevLett.110.133001.

[63] A. M. Kaufman, B. J. Lester, and C. A. Regal. "Cooling a Single Atom in an Optical Tweezer to Its Quantum Ground State". In: *Phys. Rev. X* 2 (4 Nov. 2012), p. 041014. DOI: 10.1103/PhysRevX.2.041014. URL: https://link.aps.org/doi/10.1103/PhysRevX.2.041014.

[64] Alexander Urech et al. "Narrow-line imaging of single strontium atoms in shallow optical tweezers". In: *Phys. Rev. Res.* 4 (2 June 2022), p. 023245. DOI: 10.1103/PhysRevResearch.4.023245.

[65] Alexandre Cooper et al. "Alkaline-Earth Atoms in Optical Tweezers". In: *Phys. Rev. X* 8 (4 Dec. 2018), p. 041055. DOI: 10.1103/PhysRevX.8.041055.

[66] R Bücker et al. "Single-particle-sensitive imaging of freely propagating ultracold atoms". In: *New Journal of Physics* 11.10 (Oct. 2009), p. 103039. DOI: 10.1088/1367-2630/11/10/103039.

[67] Andrea Bergschneider et al. "Spin-resolved single-atom imaging of ^{6}Li in free space". In: *Phys. Rev. A* 97 (6 June 2018), p. 063613. DOI: 10.1103/PhysRevA.97.063613.

[68] Lin Su et al. "Fast single atom imaging for optical lattice arrays". In: *Nature Communications* 16.1 (2025), p. 1017. ISSN: 2041-1723. DOI: 10.1038/s41467-025-56305-y.

[69] Toshi Kusano et al. *Spin-Cat Qubit with Biased Noise in an Optical Tweezer Array*. 2026. arXiv: 2602.22883 [quant-ph]. URL: https://arxiv.org/abs/2602.22883.

[70] Sören Dörscher et al. "Lattice-induced photon scattering in an optical lattice clock". In: *Phys. Rev. A* 97 (6 June 2018), p. 063419. DOI: 10.1103/PhysRevA.97.063419.

[71] National Institute of Standards and Technology (NIST) ASD Team. *NIST Atomic Spectra Database*. https://physics.nist.gov/asd. Version 5.11 (as of Dec. 2023) [Data accessed: Dec. 2025]. URL: https://physics.nist.gov/asd (visited on 12/18/2025).

[72] Simon Stellmer. "Degenerate quantum gases of strontium". PhD thesis. Institute of Experimental Physics, University of Innsbruck, 2013.

[73] M.M Boyd. "High Precision Spectroscopy of Strontium in an Optical Lattice: Towards a New Standard of Frequency and Time". PhD thesis. University of Colorado, 2007.

[74] C W Bauschlicher Jr, S R Langhoff, and H Partridge. "The radiative lifetime of the 1D2 state of Ca and Sr: a core-valence treatment". In: *Journal of Physics B: Atomic and Molecular Physics* 18.8 (Apr. 1985), p. 1523. DOI: 10.1088/0022-3700/18/8/011.

[75] David Husain and Gareth Roberts. "Radiative lifetimes, diffusion and energy pooling of Sr(5s5p(3PJ)) and Sr(5s4d(1D2)) studied by time-resolved atomic emission following pulsed dye-laser excitation". In: *Chemical Physics* 127.1 (1988), pp. 203–225. ISSN: 0301-0104. DOI: https://doi.org/10.1016/0301-0104(88)87119-2.

[76] Xinye Xu et al. "Cooling and trapping of atomic strontium". In: *J. Opt. Soc. Am. B* 20.5 (May 2003), pp. 968–976. DOI: 10.1364/JOSAB.20.000968.

[77] G Cattenoz. "Vacuum Acceptance Tests for the UHV Room Temperatue Vacuum System of the LHC during LS1". In: *bookftitle*. Ed. by edfitor.

[78] Ivaylo Sashkov Madjarov. "Entangling, Controlling, and Detecting Individual Strontium Atoms in Optical Tweezer Arrays". PhD thesis. California Institute of Technology, Division of Physics, Mathematics and Astronomy, 2021.

[79] Meny Menashes. "Construction of a novel strontium quantum simulator". PhD Thesis. University of Hamburg.

[80] Hendrik von Raven. "A new Caesium quantum gas microscope with precise magnetic field control". Sept. 2022. URL: http://nbn-resolving.de/urn:nbn:de:bvb:19-312786.

[81] Alexander Franzen. *GW optics components library*. 2009. URL: gwoptics.org.

[82] Leonhard Neuhaus et al. *FPGA-based feedback control of quantum optics experiments with the open source software package PyRPL*. 2023. arXiv: 2310.00086 [quant-ph]. URL: https://arxiv.org/abs/2310.00086.

[83] Ivan Kokhanovskyi. "Construction of an interference-filter-stabilized diode laser for experiments with ultracold strontium atoms". Bachelor Thesis. Ludwidg Maximilian University of Munich, 2019.

[84] Michael Delay et al. *Maximizing the Performance of Advanced Microscopes by Controlling Wavefront Error Using Optical Filters*. 2017.

[85] Christopher J. Foot. *Atomic physics*. Oxford master series in physics. Oxford ; New York: Oxford University Press, 2005. ISBN: 9780198506959.

[86] Hidetoshi Katori et al. "Laser cooling of strontium atoms toward quantum degeneracy". In: *AIP Conference Proceedings* 551.1 (Jan. 2001), pp. 382–396. ISSN: 0094-243X. DOI: 10.1063/1.1354362.

[87] Harold J. Metcalf and Peter van der Straten. *Laser Cooling and Trapping*. New York: Springer-Verlag, 1999.

[88] Stephen Eckel et al. "PyLCP: A Python package for computing laser cooling physics". In: *Computer Physics Communications* 270 (Jan. 2022), p. 108166. ISSN: 0010-4655. DOI: 10.1016/j.cpc.2021.108166.

[89] Takashi Mukaiyama et al. "Recoil-Limited Laser Cooling of ^{87}Sr Atoms near the Fermi Temperature". In: *Phys. Rev. Lett.* 90 (11 Mar. 2003), p. 113002. DOI: 10.1103/PhysRevLett.90.113002.

[90] Rudolf Grimm, Matthias Weidemüller, and Yurii B. Ovchinnikov. "Optical Dipole Traps for Neutral Atoms". In: ed. by Benjamin Bederson and Herbert Walther. Vol. 42. Advances In Atomic, Molecular, and Optical Physics. Academic Press, 2000, pp. 95–170. DOI: https://doi.org/10.1016/S1049-250X(08)60186-X.

[91] Jacob P. Covey et al. "2000-Times Repeated Imaging of Strontium Atoms in Clock-Magic Tweezer Arrays". In: *Physical Review Letters* 122.17 (May 2019). ISSN: 1079-7114. DOI: 10.1103/physrevlett.122.173201.

[92] Niamh Jackson et al. "Number-resolved imaging of ^{88}Sr atoms in a long working distance optical tweezer". In: *SciPost Physics* 8.3 (Mar. 2020). ISSN: 2542-4653. DOI: 10.21468/scipostphys.8.3.038.

[93] M. A. Norcia, A. W. Young, and A. M. Kaufman. "Microscopic Control and Detection of Ultracold Strontium in Optical-Tweezer Arrays". In: *Physical Review X* 8.4 (Dec. 2018). ISSN: 2160-3308. DOI: 10.1103/physrevx.8.041054.

[94] Fam Le Kien, Philipp Schneeweiss, and Arno Rauschenbeutel. "Dynamical polarizability of atoms in arbitrary light fields: general theory and application to cesium". In: *The European Physical Journal D* 67.5 (2013), p. 92. ISSN: 1434-6079. DOI: 10.1140/epjd/e2013-30729-x.

[95] Bradley Efron and Robert J Tibshirani. *An Introduction to the Bootstrap*. Vol. 57. Monographs on Statistics and Applied Probability. New York, London: Chapman & Hall/CRC, 1993. ISBN: 978-0-412-04231-7.

[96] Walther Gerlach and Otto Stern. "Der experimentelle Nachweis der Richtungsquantelung im Magnetfeld". In: *Zeitschrift für Physik* 9.1 (1922), pp. 349–352. DOI: 10.1007/BF01326983.

[97] Thies Plassmann et al. *Rapid state-resolved single-atom imaging of alkaline-earth fermions*. 2026. arXiv: 2602.19876 [quant-ph]. URL: https://arxiv.org/abs/2602.19876.

[98] A. G. Basden, C. A. Haniff, and C. D. Mackay. "Photon counting strategies with low-light-level CCDs". In: *Monthly Notices of the Royal Astronomical Society* 345.3 (Nov. 2003), pp. 985–991. ISSN: 0035-8711. DOI: 10.1046/j.1365-8711.2003.07020.x.

[99] Andor Technolog. *Hardware Guide Andor iXon Ultra 897 EMCCD Camera*. Accessed: 2026-01-18. Oxford, England, 2015.

[100] Pascal Scholl et al. "Erasure conversion in a high-fidelity Rydberg quantum simulator". In: *Nature* 622.7982 (2023), pp. 273–278. ISSN: 1476-4687. DOI: 10.1038/s41586-023-06516-4.

[101] Jens Samland et al. "Optical pumping of $5s4d\,^1D_2$ strontium atoms for laser cooling and imaging". In: *Phys. Rev. Res.* 6 (1 Mar. 2024), p. 013319. DOI: 10.1103/PhysRevResearch.6.013319.

[102] Renhao Tao et al. "High-Fidelity Detection of Large-Scale Atom Arrays in an Optical Lattice". In: *Phys. Rev. Lett.* 133 (1 July 2024), p. 013401. DOI: 10.1103/PhysRevLett.133.013401.

[103] A. P. Dempster, N. M. Laird, and D. B. Rubin. "Maximum Likelihood from Incomplete Data via the EM Algorithm". In: *Journal of the Royal Statistical Society. Series B (Methodological)* 39.1 (1977), pp. 1–38. ISSN: 00359246. URL: http://www.jstor.org/stable/2984875 (visited on 03/11/2026).

[104] J. Tromp. "Time-dependent wave packets and the split-step method". In: *Computers in Physics* 8.3 (1994), pp. 276–286. DOI: 10.1063/1.168472.

[105] C. Tuchendler et al. "Energy distribution and cooling of a single atom in an optical tweezer". In: *Phys. Rev. A* 78 (3 Sept. 2008), p. 033425. DOI: 10.1103/PhysRevA.78.033425.

[106] Alexandre Cooper et al. "Alkaline-Earth Atoms in Optical Tweezers". In: *Phys. Rev. X* 8 (4 Dec. 2018), p. 041055. DOI: 10.1103/PhysRevX.8.041055.

[107] Katrina Barnes et al. "Assembly and coherent control of a register of nuclear spin qubits". In: *Nature Communications* 13.1 (2022), p. 2779. DOI: 10.1038/s41467-022-29977-z.

[108] Luca Bayha et al. "Observing the emergence of a quantum phase transition shell by shell". In: *Nature* 587 (2020), pp. 583–587. ISSN: 1476-4687. DOI: 10.1038/s41586-020-2936-y.

[109] Lingfeng Yan et al. "High-Power Clock Laser Spectrally Tailored for High-Fidelity Quantum State Engineering". In: *Phys. Rev. X* 15 (3 Aug. 2025), p. 031055. DOI: 10.1103/qw53-8b8r.

[110] Chunhan Feng et al. "Metal-insulator transition and quantum magnetism in the SU(3) Fermi-Hubbard model". In: *Phys. Rev. Res.* 5 (4 Dec. 2023), p. 043267. DOI: 10.1103/PhysRevResearch.5.043267.

[111] Samuel Bird, Sebastian Huber, and Jannes Nys. "Partial suppression of magnetism in the square lattice SU(3) Hubbard model". In: *Phys. Rev. B* 112 (16 Oct. 2025), p. L161115. DOI: 10.1103/jfxt-9r1c.

[112] Andrii Sotnikov and Walter Hofstetter. "Magnetic ordering of three-component ultracold fermionic mixtures in optical lattices". In: *Phys. Rev. A* 89 (6 June 2014), p. 063601. DOI: 10.1103/PhysRevA.89.063601.

[113] Zewen Zhang et al. "Unit-density SU(3) Fermi-Hubbard model with spin-flavor imbalance". In: *Phys. Rev. A* 112 (3 Sept. 2025), p. 033313. DOI: 10.1103/7yvm-fsf5.

[114] Philippe Corboz et al. "Simultaneous Dimerization and SU(4) Symmetry Breaking of 4-Color Fermions on the Square Lattice". In: *Phys. Rev. Lett.* 107 (21 Nov. 2011), p. 215301. DOI: 10.1103/PhysRevLett.107.215301.

[115] Henning Schlömer et al. "Subdimensional magnetic polarons in the one-hole doped SU(3) $t-J$ model". In: *Phys. Rev. B* 110 (12 Sept. 2024), p. 125134. DOI: 10.1103/PhysRevB.110.125134.

[116] Maxwell F. Parsons et al. "Site-resolved measurement of the spin-correlation function in the Fermi-Hubbard model". In: *Science* 353.6305 (2016), pp. 1253–1256. DOI: 10.1126/science.aag1430.

[117] Eduardo Ibarra-García-Padilla et al. "Metal-insulator transition and magnetism of SU(3) fermions in the square lattice". In: *Phys. Rev. A* 108 (5 Nov. 2023), p. 053312. DOI: 10.1103/PhysRevA.108.053312.

[118] Thomas Hartke et al. "Doublon-Hole Correlations and Fluctuation Thermometry in a Fermi-Hubbard Gas". In: *Phys. Rev. Lett.* 125 (11 Sept. 2020), p. 113601. DOI: 10.1103/PhysRevLett.125.113601.

[119] Lin Su et al. "Dipolar quantum solids emerging in a Hubbard quantum simulator". In: *Nature* 622.7984 (2023), pp. 724–729. ISSN: 1476-4687. DOI: 10.1038/s41586-023-06614-3.

[120] L. F. Livi et al. "Synthetic Dimensions and Spin-Orbit Coupling with an Optical Clock Transition". In: *Phys. Rev. Lett.* 117 (22 Nov. 2016), p. 220401. DOI: 10.1103/PhysRevLett.117.220401.

[121] Jeong Ho Han, Jin Hyoun Kang, and Y. Shin. "Band Gap Closing in a Synthetic Hall Tube of Neutral Fermions". In: *Phys. Rev. Lett.* 122 (6 Feb. 2019), p. 065303. DOI: 10.1103/PhysRevLett.122.065303.

[122] Jean-Baptiste Bouhiron et al. "Realization of an atomic quantum Hall system in four dimensions". In: *Science* 384.6692 (2024), pp. 223–227. DOI: 10.1126/science.adf8459.

[123] M. Mancini et al. "Observation of chiral edge states with neutral fermions in synthetic Hall ribbons". In: *Science* 349.6255 (2015), pp. 1510–1513. DOI: 10.1126/science.aaa8736.

[124] Tomoki Ozawa and Hannah M. Price. "Topological quantum matter in synthetic dimensions". In: *Nature Reviews Physics* 1.5 (2019), pp. 349–357. ISSN: 2522-5820. DOI: 10.1038/s42254-019-0045-3. URL: https://doi.org/10.1038/s42254-019-0045-3.

[125] Philipp Lunt et al. "Realization of a Laughlin State of Two Rapidly Rotating Fermions". In: *Phys. Rev. Lett.* 133 (25 Dec. 2024), p. 253401. DOI: 10.1103/PhysRevLett.133.253401.

[126] Julian Léonard et al. "Realization of a fractional quantum Hall state with ultracold atoms". In: *Nature* 619.7970 (2023), pp. 495–499. ISSN: 1476-4687. DOI: 10.1038/s41586-023-06122-4. URL: https://doi.org/10.1038/s41586-023-06122-4.

[127] N. Goldman, J. C. Budich, and P. Zoller. "Topological quantum matter with ultracold gases in optical lattices". In: *Nature Physics* 12.7 (2016), pp. 639–645. ISSN: 1745-2481. DOI: 10.1038/nphys3803.

[128] Jordi R. Weggemans et al. "Solving correlation clustering with QAOA and a Rydberg qudit system: a full-stack approach". In: *Quantum* 6 (Apr. 2022), p. 687. ISSN: 2521-327X. DOI: 10.22331/q-2022-04-13-687.

[129] Sivaprasad Omanakuttan et al. "Qudit Entanglers Using Quantum Optimal Control". In: *PRX Quantum* 4 (4 Nov. 2023), p. 040333. DOI: 10.1103/PRXQuantum.4.040333.

[130] Evgeniy O. Kiktenko, Anastasiia S. Nikolaeva, and Aleksey K. Fedorov. "Colloquium: Qudits for decomposing multiqubit gates and realizing quantum algorithms". In: *Rev. Mod. Phys.* 97 (2 June 2025), p. 021003. DOI: 10.1103/RevModPhys.97.021003.

[131] Shuo Ma et al. "Universal Gate Operations on Nuclear Spin Qubits in an Optical Tweezer Array of ^{171}Yb Atoms". In: *Phys. Rev. X* 12 (2 May 2022), p. 021028. DOI: 10.1103/PhysRevX.12.021028.

[132] J. A. Muniz et al. *High-fidelity universal gates in the ^{171}Yb ground state nuclear spin qubit*. 2024. arXiv: 2411.11708 [quant-ph].

[133] Alec Jenkins et al. "Ytterbium Nuclear-Spin Qubits in an Optical Tweezer Array". In: *Phys. Rev. X* 12 (2 May 2022), p. 021027. DOI: 10.1103/PhysRevX.12.021027.

[134] William Huie et al. "Repetitive Readout and Real-Time Control of Nuclear Spin Qubits in ^{171}Yb Atoms". In: *PRX Quantum* 4 (3 Sept. 2023), p. 030337. DOI: 10.1103/PRXQuantum.4.030337.

[135] Sivaprasad Omanakuttan et al. "Fault-Tolerant Quantum Computation Using Large Spin-Cat Codes". In: *PRX Quantum* 5 (2 June 2024), p. 020355. DOI: 10.1103/PRXQuantum.5.020355.

[136] M. A. Norcia et al. "Midcircuit Qubit Measurement and Rearrangement in a ^{171}Yb Atomic Array". In: *Phys. Rev. X* 13 (4 Nov. 2023), p. 041034. DOI: 10.1103/PhysRevX.13.041034.

[137] Jook Walraven. *Atomic Physics lectures*. https://staff.fnwi.uva.nl/j.t.m.walraven/walraven/Lectures.htm. Accessed: 2026-01-05. 2015.

[138] Premjith Thekkeppatt et al. "Measurement of the g Factor of Ground-State ^{87}Sr at the Parts-per-Million Level Using Co-Trapped Ultracold Atoms". In: *Phys. Rev. Lett.* 135 (19 Nov. 2025), p. 193001. DOI: 10.1103/cjks-9hlp.

[139] S. Hampton et al. "Closed-form expressions for the magnetic fields of rectangular and circular finite-length solenoids and current loops". In: *AIP Advances* 10.6 (June 2020), p. 065320. ISSN: 2158-3226. DOI: 10.1063/5.0010982. eprint: https://pubs.aip.org/aip/adv/article-pdf/doi/10.1063/5.0010982/12830222/065320_1_online.pdf.

[140] Todd P. Meyrath. *Electromagnet Design Basics for Cold Atom Experiments*. 2001. URL: https://atomoptics-nas.uoregon.edu/~tbrown/files/relevant_papers/meyrath%20electromagnets.pdf (visited on 06/04/2026).

Acknowledgements

First and foremost, I would like to thank Ludwig Mathey and Guillaume Salomon for being my supervisors. I am especially grateful to Guillaume, for being our group leader and for the many moments of guidance, encouragement, and critical feedback throughout this PhD.

I enjoyed that you are so close to our experiment, and that you were always there to help us when we were stuck - while still allowing us to find our own way. I learned a lot from your experience, and from the way you approach the usual problems in the lab. Your ability to quickly estimate limitations and finding the tricky technical details that we had forgotten to consider in our setups is something I will always remember. I also greatly enjoyed the many lunch breaks where we discussed all the fascinating possibilities of quantum simulations with atoms, and what we can do with our experiment. There are so many things that we can do with our experiment and your enthusiasm and knowledge about atomic physics always made these conversations both motivating and exciting.

Next, I would like to thank the many colleagues at the IQP with whom I had the pleasure to work. First, there is Meny, who helped a great deal in getting the experiment up and running. In particular, for building most of the laser systems.

Then there is my lab mate Leon. I spent most of my time with Leon in the lab, and I am very grateful for that. We quickly became a good team and implemented many different functionalities over long hours in the lab. We went through many different stages: moments when we were desperate to get something working, constantly dealing with not enough laser power and a too weak atom signal but mostly moments where we managed to make fast progress such as implementing blue and red imaging, OSG kick, and free-space imaging. Our usual work approach in the lab involved a maximum portion of pragmatism. The first idea was usually something with epoxy glue, zip ties or something 3D printed. Something that always helped and brought us luck were lab snacks. It is amazing through how many candy and lab snacks we went over all that time.

I hope you will succeed with this experiment, and that you will get your green accordion lattice working. It would be amazing to see expanded atoms in the lattice structure or even getting a BEC with strontium.

Next, we have Sophie, who has recently joined us. I am very grateful that you will continue this experiment. I am sure you will succeed, and that you will explore all the different things we can do with it. I wish you all the best for what comes next.

In between, we had the great Master students, Etienne and Julie, who helped build important parts of the lab infrastructure. It was great to see how you managed to get something going in this short amount of time. At the time of writing this thesis, two further students have joined us. Thank you, Leander and Virgil, for building movable tweezers and the 448 repumper for us. These improvements will be very helpful for our experiment.

Next, I would like to thank the entire Moritz group to which we are attached. Thank you, Henning, for letting us use so much of your lab infrastructure and your expertise. I especially want to thank Niklas, Hauke, Benni, and Martin, who I could always approach for tips and tricks.

When the lab snacks were empty (which usually happened within the first hours), I could always go to the office of my study friend David, and to his drawer full of sweets and snacks. I am very grateful that our study group of Henry, David, Ruven, and Jasper stuck together for so many years, and that we had so many great experiences outside the institute.

Continuing within the institute, I would like to thank Jan, Jette, Tobi, and Nejira for the nice chats in the coffee corner

Special thanks go to the workshop. Building this experiment with so many custom-made mechanical parts would not have been possible without the work of Stefan, Gernot, Markus, Michael, and Franky. I really enjoyed seeing you manufacture the parts for our experiment and the nice chats in the workshop.

Lastly, I want to thank Laura and my family for the lovely support during the past four years. I cannot wait to see what comes next.

Eidesstattliche Erklärung

Hiermit versichere ich an Eides statt, die vorliegende Dissertationsschrift selbst verfasst und keine anderen als die angegebenen Hilfsmittel und Quellen benutzt zu haben.

Sofern im Zuge der Erstellung der vorliegenden Dissertationsschrift generative Künstliche Intelligenz (gKI) basierte elektronische Hilfsmittel verwendet wurden, versichere ich, dass meine eigene Leistung im Vordergrund stand und dass eine vollständige Dokumentation aller verwendeten Hilfsmittel gemäß der Guten wissenschaftlichen Praxis vorliegt. Ich trage die Verantwortung für eventuell durch die gKI generierte fehlerhafte oder verzerrte Inhalte, fehlerhafte Referenzen, Verstöße gegen das Datenschutz- und Urheberrecht oder Plagiate.

Hamburg, 22.07.2026	J. Pbr
.....	.....
Ort, Datum	Unterschrift